

DTIC FILE COPY

4

RADC-TR-88-160, Vol II (of two)  
In-House Report  
July 1988



AD-A206 705

# PROCEEDINGS OF THE 1987 ANTENNA APPLICATIONS SYMPOSIUM

Peter R. Franchi

Sponsored by  
DIRECTORATE OF ELECTROMAGNETICS  
ROME AIR DEVELOPMENT CENTER  
HANSCOM AFB, MA 01731  
AIR FORCE SYSTEMS COMMAND

DTIC  
ELECTE  
S 28 MAR 1989 D  
E

APPROVED FOR PUBLIC RELEASE; DISTRIBUTION UNLIMITED.

ROME AIR DEVELOPMENT CENTER  
Air Force Systems Command  
Griffiss Air Force Base, NY 13441-5700

89 3 27 090

This report has been reviewed by the RADC Public Affairs Division (PA) and is releasable to the National Technical Information Service (NTIS). At NTIS it will be releasable to the general public, including foreign nations.

RADC-TR-88-160, Vol II (of two) has been reviewed and is approved for publication.

APPROVED:



ROBERT J. MAILLOUX  
Antennas & Components Division  
Directorate of Electromagnetics

APPROVED:



JOHN K. SCHINDLER  
Acting Director of Electromagnetics

FOR THE COMMANDER:



JOHN A. RITZ  
Directorate of Plans & Programs

If your address has changed or if you wish to be removed from the RADC mailing list, or if the addressee is no longer employed by your organization, please notify RADC (FEAS ) Hanscom AFB MA 01731-5000. This will assist us in maintaining a current mailing list.

Do not return copies of this report unless contractual obligations or notices on a specific document require that it be returned.

Unclassified

SECURITY CLASSIFICATION OF THIS PAGE

## REPORT DOCUMENTATION PAGE

1a. REPORT SECURITY CLASSIFICATION Unclassified			1b. RESTRICTIVE MARKINGS		
2a. SECURITY CLASSIFICATION AUTHORITY			3. DISTRIBUTION/AVAILABILITY OF REPORT		
2b. DECLASSIFICATION/DOWNGRADING SCHEDULE			Approved for public release; Distribution Unlimited		
4. PERFORMING ORGANIZATION REPORT NUMBER(S)  RADC-TR-88-160 (Vol II)			5. MONITORING ORGANIZATION REPORT NUMBER(S)		
6a. NAME OF PERFORMING ORGANIZATION  Rome Air Development Center		6b. OFFICE SYMBOL (if applicable)  EEAS	7a. NAME OF MONITORING ORGANIZATION		
6c. ADDRESS (City, State, and ZIP Code) Hanscom AFB Massachusetts 01731-5000			7b. ADDRESS (City, State, and ZIP Code)		
8a. NAME OF FUNDING/SPONSORING ORGANIZATION Rome Air Development Center		8b. OFFICE SYMBOL (if applicable) EEAS	9. PROCUREMENT INSTRUMENT IDENTIFICATION NUMBER		
8c. ADDRESS (City, State, and ZIP Code) Hanscom AFB Massachusetts 01731-5000			10. SOURCE OF FUNDING NUMBERS		
			PROGRAM ELEMENT NO 62702F	PROJECT NO. 4600	TASK NO. 14
					WORK UNIT ACCESSION NO. 01
11. TITLE (Include Security Classification) Proceedings of the 1987 Antenna Applications Symposium					
12. PERSONAL AUTHOR(S)					
13a. TYPE OF REPORT In-house		13b. TIME COVERED FROM _____ TO _____		14. DATE OF REPORT (Year, Month, Day) 1988 July	
15. PAGE COUNT 196					
16. SUPPLEMENTARY NOTATION Volume I consists of pages 1 through 230; Volume II consists of pages 231 through 420					
17. COSATI CODES			18. SUBJECT TERMS (Continue on reverse if necessary and identify by block number)		
FIELD	GROUP	SUB-GROUP	Antennas                      Microstrip                      Multibeam Antennas		
			Satellite Antennas                      Reflector                      Array Antennas		
			Broad Antennas                      HF, VHF, UHF		
19. ABSTRACT (Continue on reverse if necessary and identify by block number) The proceedings of the 1987 Antenna Applications Symposium is a collection of state-of-the-art papers relating to phased array antennas, multibeam antennas, satellite antennas, microstrip antennas, reflector antennas, HF, VHF, UHF and various other antennas.					
20. DISTRIBUTION/AVAILABILITY OF ABSTRACT <input type="checkbox"/> UNCLASSIFIED/UNLIMITED <input checked="" type="checkbox"/> SAME AS RPT. <input type="checkbox"/> DTIC USERS			21. ABSTRACT SECURITY CLASSIFICATION Unclassified		
22a. NAME OF RESPONSIBLE INDIVIDUAL PETER R. FRANCHI			22b. TELEPHONE (Include Area Code) (617)-377-3067		22c. OFFICE SYMBOL RADC/EEAS

Accession For	
NTIS GRA&I	<input checked="" type="checkbox"/>
DTIC TAB	<input type="checkbox"/>
Unannounced	<input type="checkbox"/>
Justification	
By	
Distribution/	
Availability Codes	
Dist	Avail and/or Special
A-1	

Contents

- \* Keynote Speaker: "MMICs - The Key to Affordable Arrays," J. Schindler,  
Rome Air Development Center, Hanscom AFB, MA

WEDNESDAY, SEPTEMBER 23, 1987

#### PHASED ARRAYS

1. "MMIC Phased Arrays," A. I. Zaghloul and R. J. Mailloux 1
- \* 2. "Wideband Active Phased Array," C. D. Pepe, M. J. Povinelli, and  
J. J. Komiak
3. "A Ku-Band Hemispherical Array Antenna for Possible Space Station  
Application," R. W. Shaw, J. R. Carl, and G. D. Arndt 31
4. "Antenna Subsystem for Aviation Satellite Communications," S. Y. Peng,  
H. H. Chung, and W. Foy 47

\* NOT INCLUDED IN THIS VOLUME

- \* 5. "A Cavity-Backed Twin-Slot Array for IFF Applications," W. Foy, H. H. Chung, and S. Y. Peng
- \* 6. "Single Reflector Shaping Technique," A. R. Cherrette, and S. W. Lee

## CONFORMAL ANTENNAS

- 7. "Analysis of Finite Phased Arrays of Circular Microstrip Patches," M. D. Deshpande and M. C. Bailey 63
- 8. "An Experimental Investigation of Parasitic Microstrip Arrays," R. Q. Lee, R. Acosta, J. S. Dahele, and K. F. Lee 91
- 9. "A Multi-Layer Multi-Band Symmetrical Microstrip Antenna," S. Sensiper 109
- \* 10. "Conformal Microstrip Antennas," V. Clark and Y. T. Lo
- 11. "Slot-Coupled Microstrip Constrained Lens," D. T. McGrath, Capt, USAF 139
- \* 12. "Resonance Frequency of a Rectangular Microstrip Patch," W. C. Chew and Q. Liu
- \* 13. "Microwave Antenna Arrays as Contact Applicators for Clinical Hyperthermia," A. F. Peterson and E. C. Burdette

THURSDAY, SEPTEMBER 24, 1987

## ADAPTIVE ANTENNAS

- 14. "On the Behavior of Adaptive Lens and Feed Antennas," M. Santana and R. Blau 169
- 15. "A Stochastic Conjugate Gradient Algorithm for Adaptive Arrays," H. M. Ibrahim and N. M. Ibrahim 181
- 16. "Adaptive Transform Feed Test Results," M. Hayes, Capt, USAF 201
- \* 17. "Adaptive Antenna Analysis Using the Method of Moments," G. C. Thorpe, J. L. Fath, W. P. Baker, and A. J. Terzuoli
- 18. "Polarization Multiplexing Systems," T. D. Moran and B. J. Lamberty 231
- 19. "Interference Suppression Using an Adaptive Polarization Combiner," B. J. Lamberty and R. P. Friedman 247
- \* 20. "Moment Method Resolution Enhancement for Scanning Antennas," C. Marcus and W.T. Carey

\* NOT INCLUDED IN THIS VOLUME

# BROADBAND ANTENNAS

## Contents

- 21. "Performance Characteristics of Notch Array Elements Over a 6/1 Frequency Band," G. J. Monser 263
- \* 22. "Broadband Feeds for Vivaldi Antennas," K. Flantz and P. Mayes
- \* 23. "Improved Endfire Log-Periodic Dipole Array Antennas," S. C. Kuo
- \* 24. "Discone Design Using Simple N-Connector Feed," T. S. Rappaport
- 25. "An Orbiter - ACTS Communications Experiment," G. D. Arndt, L. Leopold, S. H. H. Chen, Y. C. Loh, Y. S. Kuo, R. Shaw and J. Carl 277
- 26. "MOM Analysis of a Finite Length Slot in an Infinite Conducting Sheet," H. A. Karwacki 297
- \* 27. "On the Service Area of AM Broadcast Stations: The Optimum AM Broadcast Antenna," V. Trainotti

FRIDAY, SEPTEMBER 25, 1987

# ANTENNA MEASUREMENTS AND ANALYSIS

- 28. "Near-Field Bistatic RCS Measurement at BDM," R. Rogers and E. Farr 321
- 29. "Field Uniformity Criteria for the Design of a Two-Wire EMP Simulator," C. Zuffada and N. Engheta 345
- 30. "A Unified Method of Antenna System Analysis Based on the Parametric Modeling of Component Scattering Coefficients," W. Milroy, R. Lewis, M. Thomas, and S. Drost 361
- 31. "Solving Maxwell Equations by Matrix Formulation in Antenna Design and Applications," F. C. Chang 391
- \* 32. "Scattering From the Interior of a Corner Reflector Using the Spectral Domain Technique," G. P. Saramadis and S. R. Laxpati

\* NOT INCLUDED IN THIS VOLUME

## POLARIZATION MULTIPLEXING SYSTEMS

Thomas D. Moran and Bernard J. Lamberty

Boeing Electronics Company, High Technology Center

### Abstract

In a polarization diversity system it is conceptually feasible to multiplex two orthogonally polarized signals onto a single channel. The savings in system hardware could be significant, particularly if the antenna is a phased array and multiplexing can be achieved near the front end of each element. Multiplexing however, increases T/R module complexity and could degrade polarization orthogonality below acceptable levels if isolation between channels is not preserved. A study was conducted to evaluate advantages and disadvantages of three different multiplexing techniques; frequency, quadrature, and pseudorandom code. Increase in bandwidth, phase sensitivity, and complexity relative to a two channel system are compared.

### 1.0 INTRODUCTION

A polarization diversity system receives and processes two orthogonally polarized signals simultaneously. This normally requires two independent sets of hardware throughout the system up to the location where the two signals are processed or combined. Depending on the specific application, a minimum level of isolation along with phase and amplitude balance must be preserved between the two signals to maintain polarization orthogonality. If these two signals could

be multiplexed onto a single channel while maintaining adequate channel isolation and balance, a significant system simplification and therefore cost savings is potentially available.

Radar, communications, and ECM are examples of systems which often use polarization diversity and so could benefit from polarization multiplexing. An L-band radar application was used to evaluate this concept. To provide parameter values for comparison between multiplexing candidates, the following specifications were selected for this study: channel isolation >30 dB, frequency band center = 1 GHz, bandwidths = 10 MHz and 100 MHz. Extrapolations to other applications can be made based on results of this study.

Figure 1 shows schematic diagrams of typical T/R modules used to evaluate the polarization multiplexer approaches. Figure 1a shows a module without polarization multiplexing; Figure 1b shows the same module with multiplexing incorporated. Note that transmission is on a single polarization whereas the return signal is received simultaneously on orthogonally polarized channels. Such a system might be used to suppress interfering signals via polarization nulling or to characterize target scattering as a function of polarization. The dual channel system requires at least two combiner networks compared to one for a multiplexed system. The potential to eliminate one array combiner and its phase matched cables seemed to outweigh the complexity added by a multiplexer/demultiplexer system - especially if the multiplexer could be implemented with a microwave monolithic integrated circuit (MMIC).



## 2.0 CANDIDATES

The three multiplexing candidates are frequency, quadrature and pseudorandom code. These candidates, shown in Figure 2 along with their respective frequency spectra in Figure 3, are described below.

In frequency division multiplexing a common local oscillator is mixed with each polarization channel.<sup>1</sup> The upper sideband ( $f_{RF} + f_{LO}$ ) is used by the vertically polarized channel and the lower sideband ( $f_{RF} - f_{LO}$ ) by the horizontally polarized channel. These two frequency bands are summed and sent to the N-way combiner along a common transmission line. Demultiplexing is achieved at the array output by power splitting and filtering to separate the upper and lower sidebands. These sidebands are then mixed with  $f_{LO}$  and filtered to recover the orthogonally polarized signals.

In quadrature division multiplexing the horizontal channel is mixed with the local oscillator and the vertical channel with the local oscillator phase shifted 90 degrees.<sup>2</sup> This places the mixer products (both upper and lower sidebands) of channel one and two in phase quadrature allowing both channels to be combined onto one line while preserving isolation. Demultiplexing is accomplished by power splitting the common line and re-mixing with the in-phase and quadrature local oscillator to preserve the time alignment of each channel at the multiplexer. The mixer products are such that cancellation occurs eliminating the undesired channel leaving the desired signal at the mixer output. Bandpass filtering is used to remove extraneous products incurred through the demultiplexing process.

In code division multiplexing each channel is multiplied by a unique pseudorandom code before the channels are summed and sent along a single transmission line.<sup>3,4</sup> Typically maximum linear code sequences are chosen to encode the channels. The same code sequence can be applied to each mixer within the multiplexer provided that one channel's code is delayed by at least one code bit. Since code sequences of this type have a DC component, isolation is limited by code length. This DC component is inversely proportional to code length so if sufficiently long codes are chosen a low DC component results. For example, a 31-bit code has a sufficiently small DC component to allow nearly 30 dB of isolation between channels. Since the code is pseudorandom the spectral distribution is  $\sin(x)/x$  with main lobe nulls at plus and minus the code rate about the center frequency. For a 10 MHz information bandwidth a 310 MHz code rate is needed resulting in a 620 MHz multiplexed channel bandwidth. Demultiplexing is accomplished by mixing the codes with the multiplexed channel in such a way as to maintain the same time relationship that occurred at the multiplexer. A bandpass filter is then used to separate the desired channel from the  $\sin(x)/x$  spectrum of the undesired channel.

## 2.1 IMPLEMENTATION DETAILS

Single sideband frequency division multiplexing can be implemented within each T/R module in two basic ways, through use of either single sideband modulators or single sideband filters. The single sideband modulator approach requires four mixers and two 0-180 degree hybrids per module. The single

sideband filter approach is more direct but requires phase matched, flat group delay filters within each T/R module.

Quadrature division multiplexing is simpler from a hardware standpoint, although to achieve the desired channel isolation, phase match between multiplexer and demultiplexer local oscillators must be tightly controlled ( $\pm 1.8$  degrees for 30 dB channel isolation). Additionally, this local oscillator phase sensitivity can have an effect on selection of a T/R module configuration. The common transmit/receive phase shifter shown in Figure 1b alters this phase match by delaying the multiplexed channel with respect to the local oscillator thus degrading isolation. For L-band systems of narrow bandwidth ( $\approx 1\%$ ) this effect can be tolerated because the local oscillator frequency can be very low. For wideband systems ( $\approx 10\%$ ) however, isolation degradation is sufficiently severe that if a phase shifter is to be included within the multiplexed channel (as shown in Figure 1b), phase compensation in the demultiplexed local oscillator is required. Alternately, two receiver phase shifters could be placed ahead of the multiplexer such that the multiplexed channel and local oscillator remain in time synchronization regardless of phase shifter position. This would require an additional phase shifter and thus would increase array complexity.

Code division multiplexing is similar to the quadrature technique in terms of T/R module complexity. While this technique requires a phase matched local oscillator like the quadrature case, the isolation is much more tolerant of phase mismatch. However a much higher frequency "local" oscillator must be used which offsets this. A potential advantage of this method is that more than two

channels may be multiplexed. This could be used to advantage in a dual polarization system using sum and difference channels for angle-of-arrival data.

## 2.2 MEASUREMENTS

Measurements were made of two of the multiplexed approaches, quadrature and code, to verify that the specified level of isolation was achievable. No measurements were made of the frequency technique because its performance is easily predicted.

A model of a quadrature multiplexed system was measured with the test setup shown in Figure 4a and pictured in Figure 5. Slightly different frequencies were used for each channel so that relative channel isolation could be displayed on a spectrum analyzer. Measurements were made with a 51 MHz local oscillator and 1000 MHz and 1003 MHz carriers for each of the two polarization channels. The 51 MHz local oscillator was used to accommodate the available 5% bandwidth 1 GHz tunable bandpass filters. (Note: isolators in the demultiplexer are necessary to prevent high order products reflected from the bandpass filter from reducing channel isolation via recombination within the mixer.) Measurements indicated that 30 dB of isolation could easily be obtained with the quadrature multiplexer method.

The test setup for the code division multiplexer model is similar to that of the quadrature setup except the 0-90 degree hybrids are not required and no output filtering was attempted due to the low code rate necessitated by available equipment. A [5,2] 31-bit maximum linear code with a 10 MHz chip (clock)

rate was used to drive the mixers as shown in Figure 4b. A digital delay circuit was used to generate a one-bit delay for channel 2. Isolation measured  $\approx 30$  dB as predicted for the 31-bit code.

### 2.3 COMPARISON OF ADVANTAGES AND DISADVANTAGES

The key advantage of a frequency division multiplexed system is complete insensitivity to multiplexer/demultiplexer local oscillator phase. Its most important drawback is that accurate phase matched filters both at the multiplexer and demultiplexer may prove difficult to implement.

The key advantages of the quadrature division multiplexer approach are that the multiplexer within the T/R module is simple and easy to phase match. The low frequency 5 MHz local oscillator and its quadrature can be generated digitally with a clock. Phase matching, while critical is simplified due to the low frequencies involved. This technique tends to work best for narrow bandwidth systems although it can be adapted for wide bandwidth operation by adding additional hardware.

Code division multiplexing is much less phase sensitive than quadrature multiplexing. However, because the code rate for a typical system with 1% bandwidth is more than 50 times that of the quadrature system, the low phase sensitivity of this approach is overshadowed by the other technique's lower local oscillator frequency. As a result of the high local oscillator frequency, the multiplexed channel bandwidth is quite high - nearly 1 GHz for a 1% bandwidth system and much higher for a 10% bandwidth system. Figure 6 compares

isolation vs. local oscillator line length variation for the quadrature and code division techniques.

Figure 7 summarizes advantages and disadvantages of the three multiplexing alternatives.

### 3.0 CONCLUSIONS

In a two channel radar a multiplexed system has the potential for reducing the number of high frequency power combiners and associated phase matched cables by a factor of two. This is achieved at the expense of a more complex T/R module and the distribution of phase matched local oscillator lines.

For the L-band radar example with 1% bandwidth the quadrature multiplexer approach appeared optimal. Its low frequency local oscillator requirement, low channel bandwidth, and simple module multiplexer held the greatest promise despite its phase sensitivity. Monolithic active mixers have the potential for yielding small, inexpensive, phase matched multiplexers, which because of their MMIC implementation could improve the cost/performance ratio of a phased array system.

### 4.0 REFERENCES

1. Stremier, F. G. (1977) Introduction to Communication Systems, Addison-Wesley, Massachusetts, p.222.
2. IBID., p.196.

3. Hawthorne, D. L. (1986) Polarization Measurement, Proceedings of the 1986 Antenna Applications Symposium.
4. Dixon, R. C. (1984) Spread Spectrum Systems, Wiley, New York, p. 87.

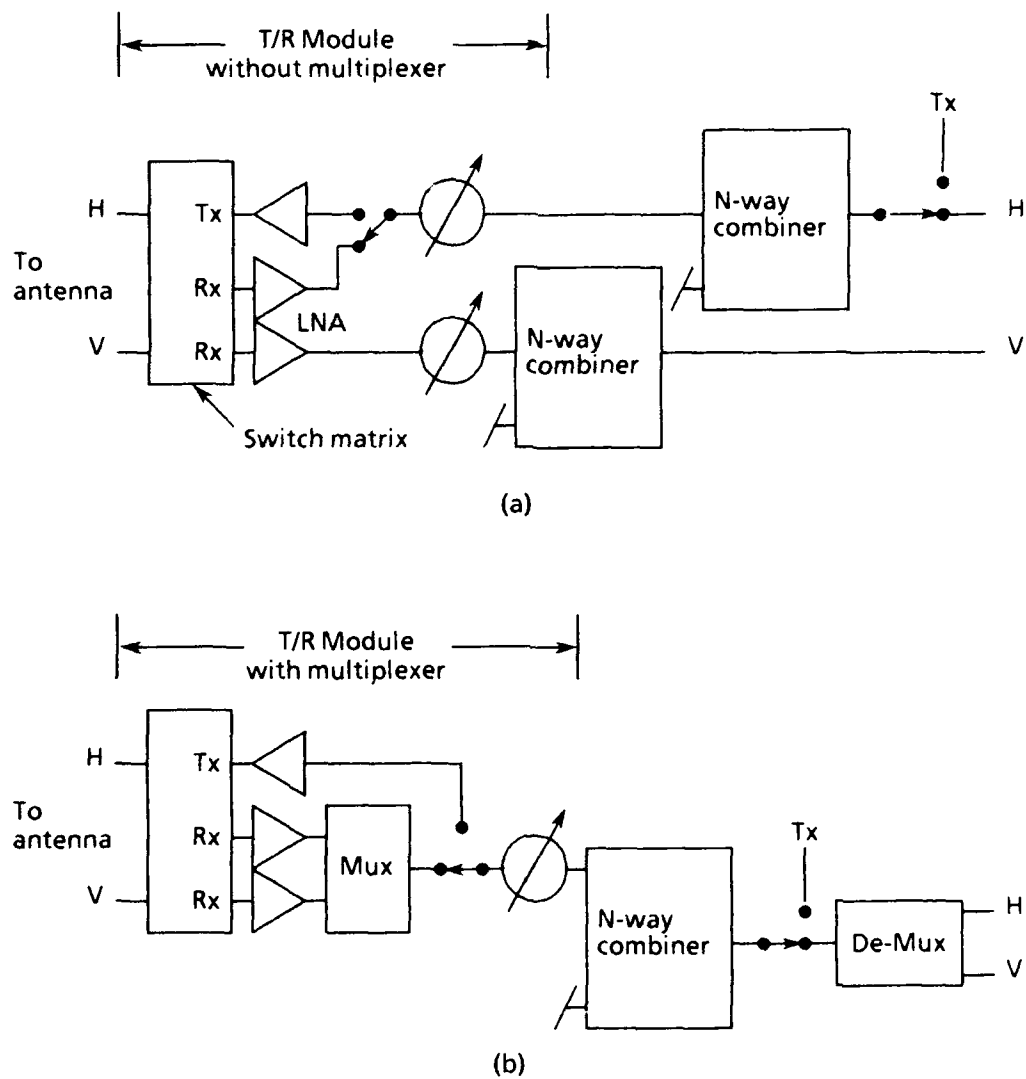


Figure 1. T/R Module and Combiner Network



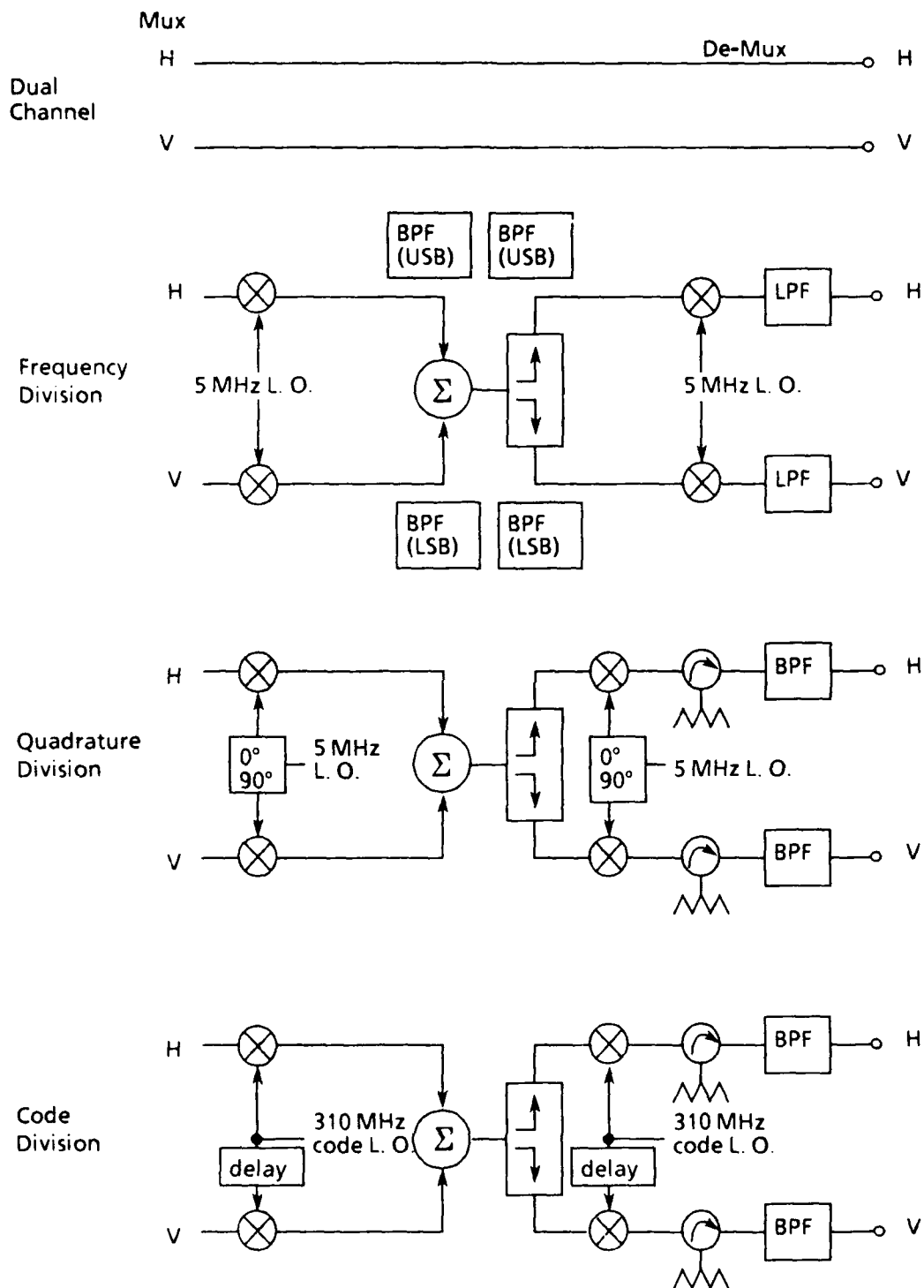


Figure 2. Polarization Multiplexer Approaches

## Multiplexing

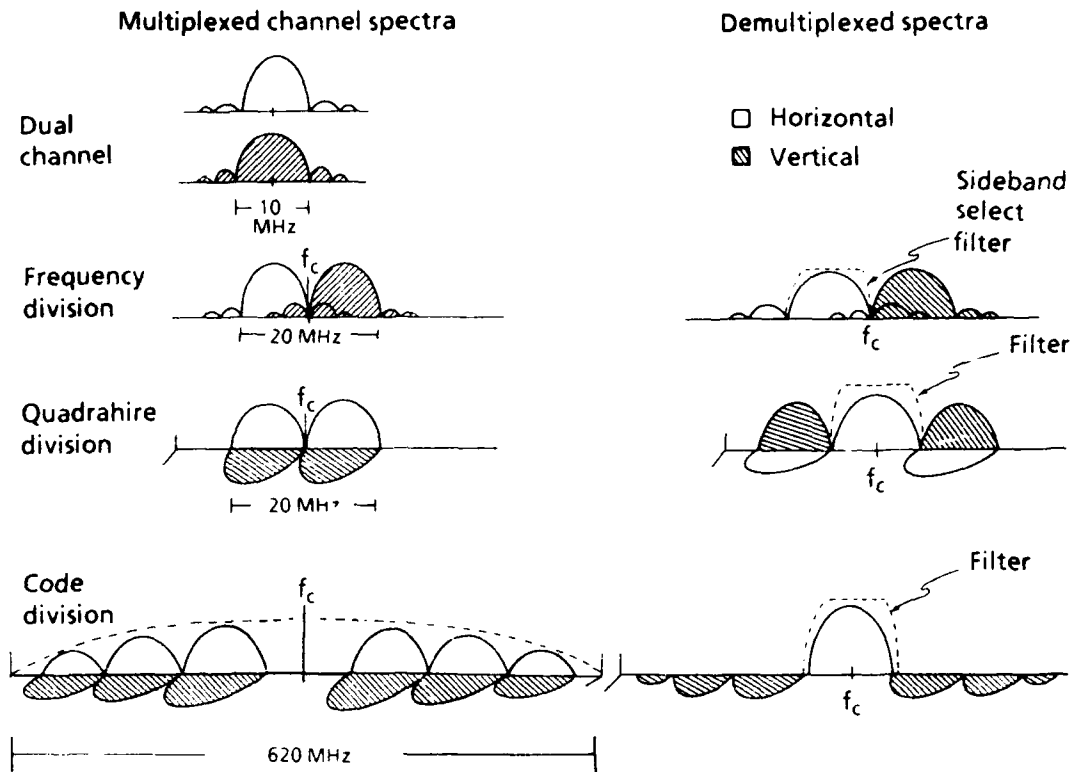


Figure 3. Spectral Distribution for Dual Polarization

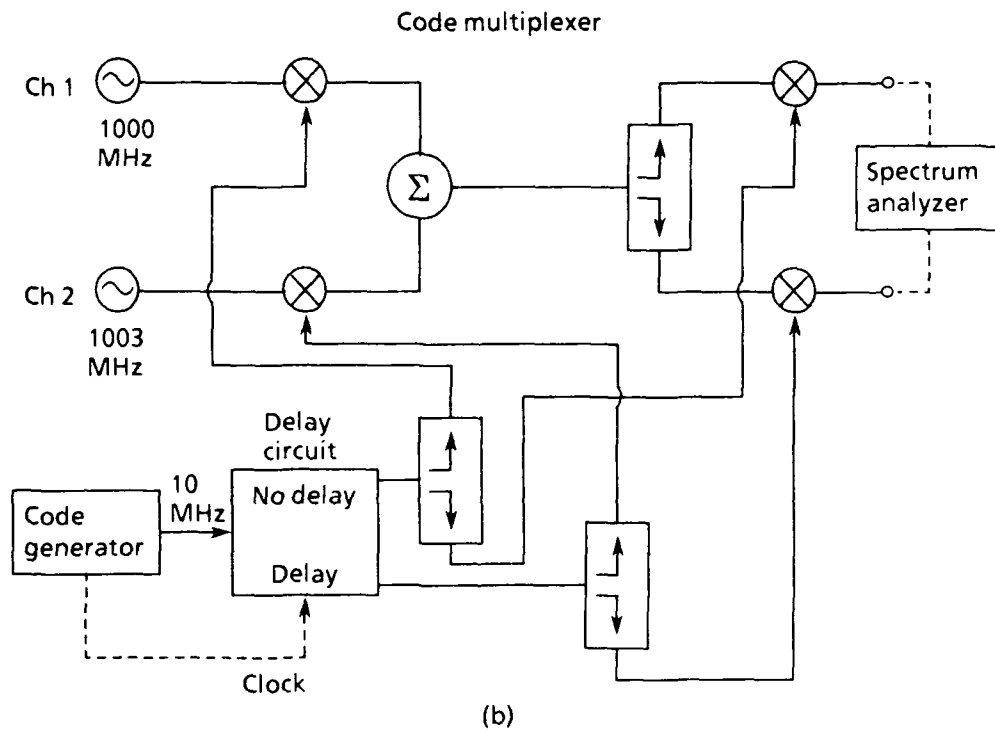
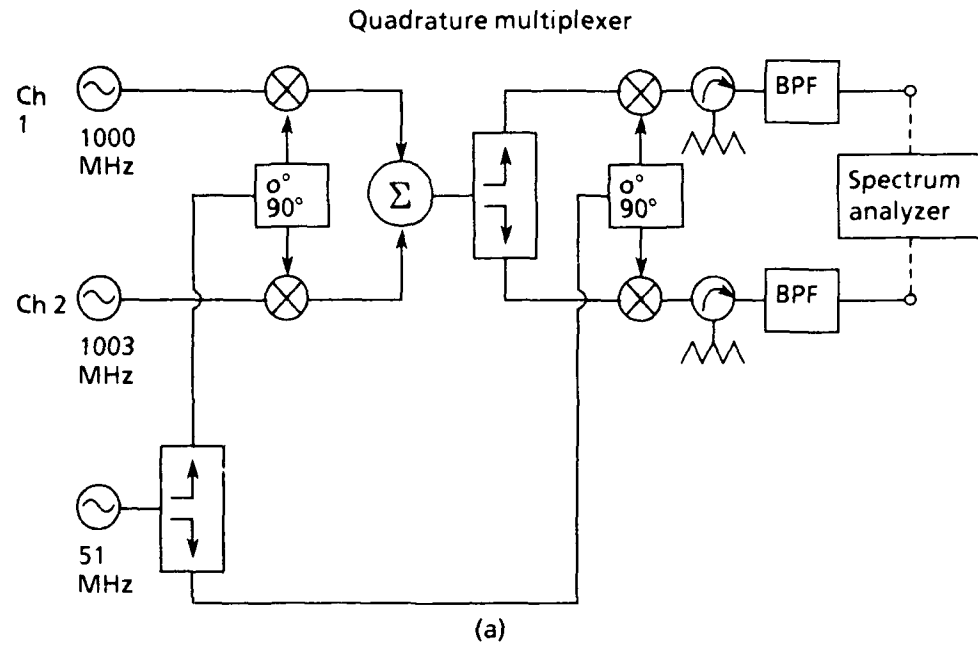


Figure 4. Measurement Test Setup

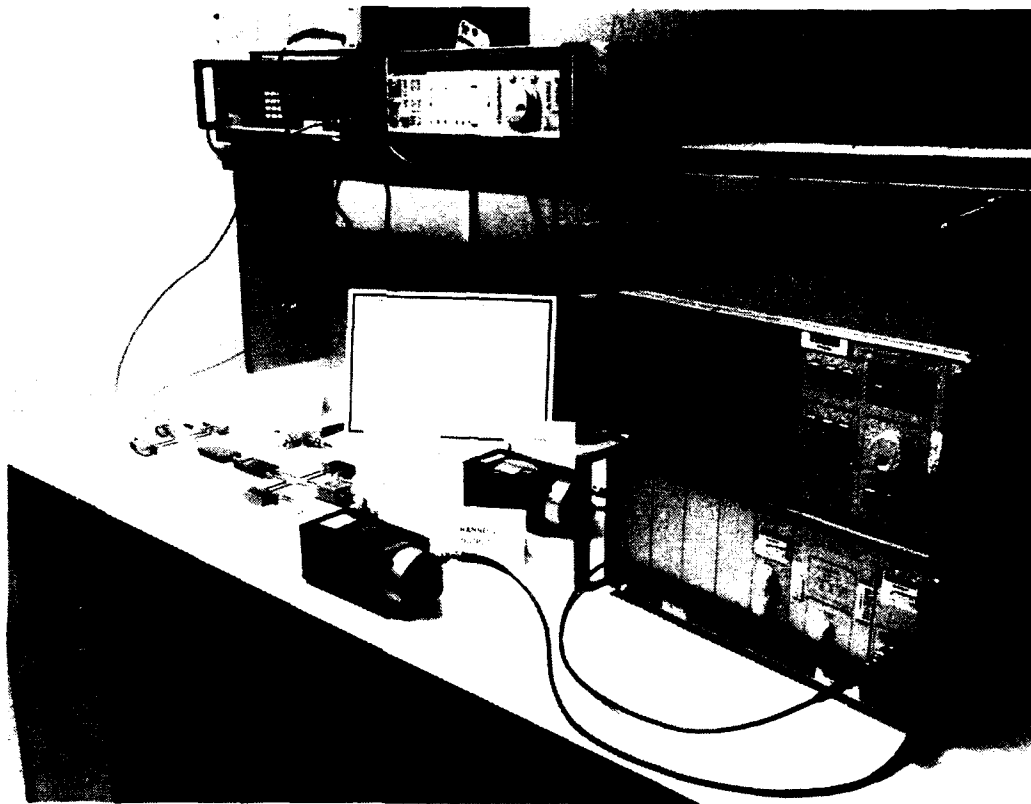


Figure 5. Quadrature Division Multiplexer/Demultiplexer Test Setup

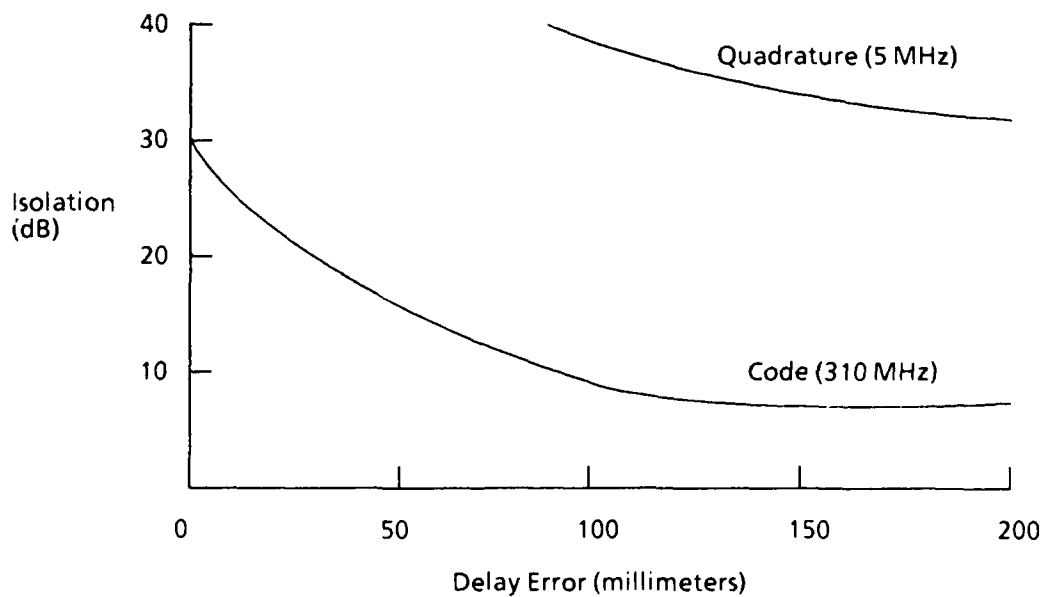


Figure 6. Quadrature vs. Code Division Isolation Sensitivity (10 MHz BW)

Candidates	Minimum Required Channel Bandwidth (10 MHz info BW)	Main Advantages	Key Limitations
Dual Channel (reference)	10 MHz	Simple module design Lowest channel bandwidth	Requires twice as many external combiners and RF phase matched cables/module as multiplexer approaches
Frequency Division Multiplexing (single-sideband)	20 MHz	Isolation independent of L.O. phase Allows direct conversion to IF Low frequency L.O.	Requires linear phase single sideband filters or modulators within module and at demultiplexer
Quadrature Division Multiplexing	20 MHz	Simple multiplexer at module Low frequency L.O.	Accurate L.O. synchronization must be maintained No direct conversion to IF Dual channel only
Code Division Multiplexing (31-bit maximal linear code)	620 MHz	Low sensitivity to L.O. synchronization Multiple channel capacity	Requires very wide channel BW No direct conversion to IF Channel isolation depends on code length

*Figure 7. Polarization Diversity Implementation Trade Study*

## INTERFERENCE SUPPRESSION USING AN ADAPTIVE POLARIZATION COMBINER

Bernard J. Lamberty and Robert P. Friedman

Boeing Electronics Company, High Technology Center

### ABSTRACT

Polarization diversity systems receive and process dual, orthogonally polarized signals. A circuit consisting of hybrids and phase shifters can be used for combining these signals which may be of arbitrary magnitude and phase. With proper adjustment of the phase shifters, either open-loop or adaptively, total input power is sent to one output port while a signal null occurs at the other. Thus the circuit is suited for either optimizing received power from a desired signal or for suppressing undesirable in-band interfering signals. A study was conducted to evaluate this polarization combining network including determination of effects of component errors on null depth. Of particular interest were quantization effects of using digital phase shifters and amplitude detectors in the circuit. Null depth as a function of amplitude and phase of input signals was calculated and compared with measurements for combiners using both 4- and 5-bit phase shifters and for amplitude detection quantization levels of up to 3 dB. Results are used to predict effectiveness of interfering signal suppression as a function of incident signal polarization.

## 1.0 INTRODUCTION

Polarization diversity can be used for signal enhancement or to suppress an interfering signal whose polarization is different from the desired signal. Figure 1 is a schematic of a simple network that can be used to do this.  $V_1$  and  $V_2$  are the incident signal voltages received by the orthogonally polarized antennas of the diversity system. These voltages are of arbitrary relative magnitude and phase. The first phase shifter, PH1, is used to equalize their phases. When these equal phase voltages are passed through the first hybrid, H1, its output voltages are of equal magnitude. The second phase shifter, PH2, is used to adjust these equal magnitude voltages to be orthogonal in phase. Finally, when the equal magnitude, orthogonal phase voltages pass through the second hybrid, H2, they add in phase at one output and cancel at the other. Thus, the combiner can be used to either extract all the power from an arbitrarily polarized signal at the sum output port, or to cancel an in-band interfering signal at the null output port.\* This paper concentrates on the level of cancellation available from practical polarization combiner circuits.

## 2.0 DETAILS OF OPERATION

Voltage magnitude and phase relationships at successive junctions of the polarization combiner circuit shown in Figure 1 are:

$$V_1 = V_1 e^{j\theta^\circ}, \quad V_1' = V_1 e^{j0^\circ}, \quad V_2 = V_2 e^{j0^\circ} \quad (1)$$

---

\* For processing, the interfering signal must have some parameter to distinguish it from the desired signal (e.g. bandwidth)

$$V_1'' = \frac{1}{\sqrt{2}} (V_1 e^{j0^\circ} + V_2 e^{-j\pi/2}) \quad (2)$$

$$V_2'' = \frac{1}{\sqrt{2}} (V_1 e^{-j\pi/2} + V_2 e^{j0^\circ}) \quad (3)$$

$$V_1''' = \frac{1}{\sqrt{2}} (V_1 e^{-j\alpha} + V_2 e^{-j(\alpha+\pi/2)}) \quad (4)$$

$$V_{AO} = \frac{1}{\sqrt{2}} (V_1 e^{-j\alpha} + V_2 e^{-j(\alpha+\pi/2)} + V_1 e^{-j\pi} + V_2 e^{-j\pi/2}) \quad (5)$$

$$V_{BO} = \frac{1}{\sqrt{2}} (V_1 e^{-j(\alpha+\pi/2)} + V_2 e^{-j(\alpha+\pi)} + V_1 e^{-j(\pi/2)} + V_2 e^{-j0^\circ}) \quad (6)$$

To find the values of alpha that sends all the input power to Port A and zero power to Port B, the real and imaginary parts of  $V_{BO}$  are each set equal to zero. This results in:

$$\cos \alpha = \frac{1 - \left(\frac{V_1}{V_2}\right)^2}{1 + \left(\frac{V_1}{V_2}\right)^2} \quad (7)$$

$$\sin \alpha = \frac{2 \left(\frac{V_1}{V_2}\right)}{1 + \left(\frac{V_1}{V_2}\right)^2} \quad (8)$$



Alpha, plotted as a function of  $|V_1/V_2|$  in Figure 2, varies from 0 degrees for  $V_1=0$  to 90 degrees for  $V_1=V_2$  to 180 degrees for  $V_2=0$ . If the values of alpha shown in Figure 2 are increased by 180 degrees, maximum power appears at  $V_{BO}$  and the null appears at  $V_{AO}$ . Relative phase between input signals is arbitrary so PHI1 must provide 360 degrees of phase shift.

### 3.0 ADAPTIVE COMBINER EVALUATION

If the polarization combiner is to be adjusted or controlled remotely, digital phase shifters may be more convenient for PHI1 and PHI2 than continuously variable designs. Then since only a limited number of discrete values of phase shift are available, total signal cancellation can only be achieved for certain specific input signal amplitude ratios and relative phases. (See Figure 2). The null depth for other input signal combinations is a function of number of bits in the phase shifters.

In addition, if the combiner is adaptive, the phase shifters must be driven by closed loop circuits as shown conceptually in Figure 3. Here the phase detector circuit drives the first phase shifter, PHI1, until  $V_1$  and  $V_2$  are in-phase or as close to in-phase as that digital phase shifter will allow. Then the amplitude detection circuit drives the second phase shifter, PHI2, until a minimum signal is present at  $V_B$ . In another concept, the amplitude detection circuit is located between PHI1 and H1. PHI2 is then driven to its appropriate phase setting based on stored lookup tables taken from Figure 2. Because these or other implementations could involve measurement of  $|V_1/V_2|$ , effects of amplitude measurement resolution on null depth were examined for quantization levels of 1

dB, 2 dB and 3 dB. Hybrid and phase shifter error effects can also affect null depth and so were included in the study.

### 3.1 PASSIVE COMPONENTS ERROR EFFECTS ANALYSIS

The sources of error in the adaptive polarization combiner circuit are; (1) phase shifter errors (quantization, phase detection, and other deviations from ideal phase settings), (2) input voltage ratio amplitude detection errors, (3) 90 degree hybrid amplitude and phase imbalances, (4) phase shifter insertion loss variations, (5) phase shifter and hybrid VSWR and (6) hybrid isolation. These error terms are listed in decreasing order of importance under the assumption that the combiner uses typical hybrids and digital phase shifters with a least significant bit of a few degrees. Equations 1-8, expanded to include the first 4 of these error sources, were used to predict null depths for input voltage ratios of 0 to 60 dB. Effects of the most important sources were calculated first with less important sources added in successive iterations.

Figure 4 shows null depth (dB below total input power) as a function of input voltage ratio if  $V_1$  and  $V_2$  are in phase. Note that PHI2 is the only source of quantization phase error for this case since PHI1 phase = 0. There are four shallow nulls of approximately 20 dB each when a 4-bit phase shifter is used (22.5 degree phase increment) and eight shallow nulls of approximately 26 dB each when a 5-bit phase shifter is used (11.25 degree phase increments). The deep nulls between each of these correspond to input voltage magnitudes where the required phase for optimum nulling is exactly equal to one of the phase shifter bit settings. Shallowest nulls occur when the required phase for optimum

nulling is half a bit from the two nearest available phase shifter bit settings. Shallow nulls are lower by 6 dB for every additional bit in the phase shifter. Identically shaped curves exist for input voltage magnitude ratios of 0 to -60 dB. (See Figure 2).

Figure 5 is the same as the 4-bit case in Figure 4 except that the input voltage phase differences range from 0 to 11.25 degrees. PH1, used to co-phase these voltages, now can introduce an additional quantization error which is greatest at input voltage phase differences halfway between phase shifter bits (11.25 degrees). Here the first deep null degrades to 20 dB and the first shallow null to 17 dB. Degradations of both the shallow and deep nulls are less severe as input voltage ratios increase. However, all nulls are less than 30 dB. Similar curves were computed for the 5-bit case. Nulls were deeper by about 6 dB. Responses are periodic with input signal phase difference. The periodicity is related to quantization bit increments, that is, the same response occurs for input voltage phase differences of  $N \times (\text{bit increment})$  with  $N$  an integer.

Figure 6 is similar to the case shown in Figure 4 except that amplitude ratio measurement quantization errors are included. Here the decision to switch phase shifter settings is made in 1 dB, 2 dB or 3 dB increments of  $|V_1/V_2|$ . The resulting null depth is compared to 0 dB amplitude resolution. Using the 2 dB increment as an example, if  $|V_1/V_2|$  is between 4 dB and 7 dB, PH12 is set as if that ratio were 6 dB. This degrades null depth for  $|V_1/V_2|$  between 5 and 5.4 dB, since the phase shifter would have a different setting in that range for zero amplitude resolution error. For the 4-bit phase shifter case, this range of

amplitude resolution errors affects the shallow nulls only which are degraded by 0.9 dB, 2.2 dB and 3.7 dB respectively.

Similar calculations were made for 5-bit phase shifters in the combiner. Shallow nulls degrade by about 3 dB for both the 1 dB and 2 dB amplitude resolution cases and by over 6 dB for the 3 dB resolution case. Also, the 3 dB resolution case results in the loss of two deep nulls completely. Further null degradation occurs if the input voltage phases are separated by half a bit. Then the worse case null is about 16 dB for the 4-bit case and about 19 dB for the 5-bit case.

Figure 7 shows the added error effects of hybrid amplitude imbalances and phase shifter loss variations. Measured values of individual components were used for these predictions. As shown in the figure, results depend on which input voltage is larger since hybrid imbalance is constant. If its insertion loss is greater on the  $V_1$  side, the effect will be different for  $V_1 > V_2$  than for  $V_1 < V_2$  and vice versa.

### 3.2 MEASUREMENT OF ERROR EFFECTS IN PASSIVE COMPONENTS

The error analyses were verified by measurements using the polarization combiner model and test setup shown in Figures 8 and 9. Tests were conducted over the 950 MHz to 1150 MHz band. A single RF source feeds a 3 dB power divider which in turn feeds the sum and null lines in the test setup. In the sum line there is a discrete level variable programmable attenuator with attenuation bits of 1, 2, 4, 10, 20 and 40 dB. a variable analog phase shifter is used to set input signal phase differences. Pads are used between components to minimize

VSWR interactions. The model uses four digital phase shifters, but only the two in the sum line are used to adjust phase. The two difference line phase shifters are always set to 0 degrees and are only used to balance insertion loss and phase of the operated phase shifters.

Output null depths were measured from 950 MHz to 1150 MHz on the HP 8573 network analyzer with a marker on 1000 MHz to record data for single frequency analysis comparison verification.

Figure 10 shows a comparison of measured null depths versus those computed from the single frequency analyses. This plot is for an input signal phase difference of 80 degrees and input magnitude ratios of 0 to 60 dB. All measured component error terms are included in the analysis. The agreement is excellent between measured and computed values. Similar comparisons for input phase difference of 0 and 40 degrees also showed excellent agreement.

Figure 11 shows a comparison of measured and calculated data over a 20% frequency band for an input voltage amplitude ratio of 10 dB and phase difference of 40 degrees. The calculated data predicts the deepest null to occur at a frequency greater than 1000 MHz which is in agreement with the measured data.

#### 4.0 CONCLUSIONS

A simple polarization combiner can be used in a polarization diversity system to suppress interfering signals where the level of suppression depends on the quality of the components.

Analysis can predict combiner performance based on realistic specifications and/or measurements of its components.

Digital phase shifters and amplitude detection circuits may be required to make the combiner adaptive. Over 17 dB of interference suppression can be attained using 4-bit phase shifters and over 23 dB using 5-bit phase shifters.

The two largest contributors to degraded nulls are the quantization errors of these digital phase shifters and amplitude ratio detectors.

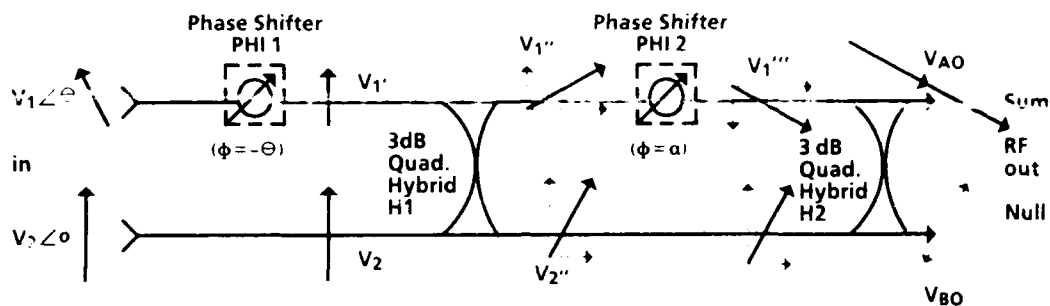


Figure 1. Polarization Combiner Network and Vector Diagram

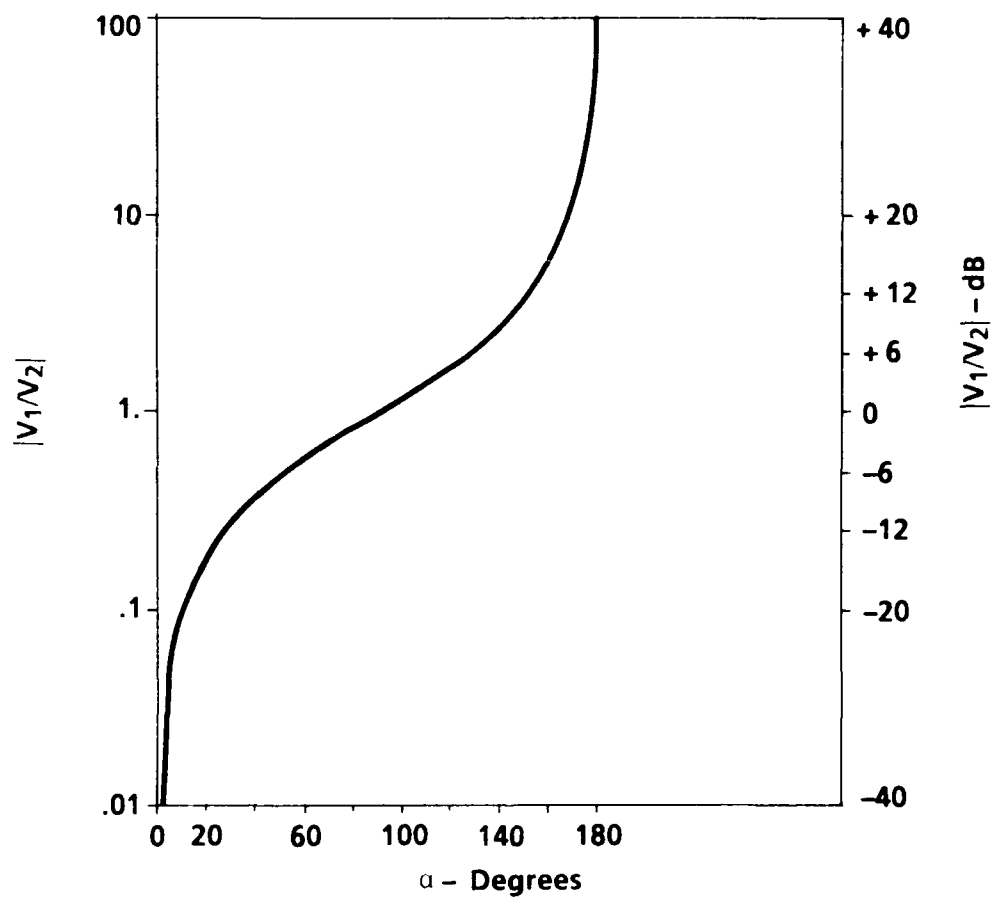


Figure 2. Phase Shift Required for Unequal Signal Combining

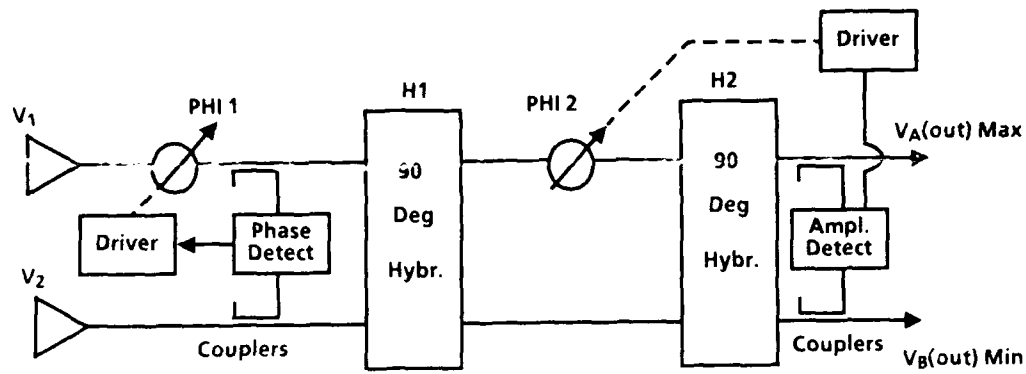


Figure 3. Adaptive Polarization Combiner

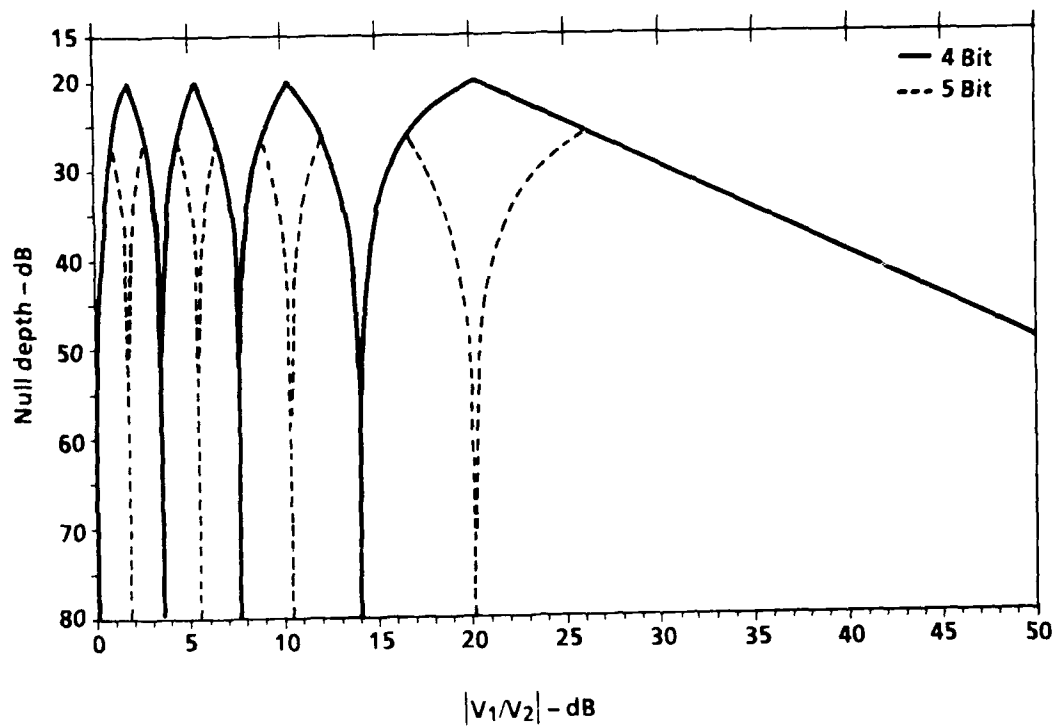


Figure 4. Polarization Combiner Predicted Null Depths; 4-Bit and 5-Bit Phase Shifter; Input Voltages in Phase



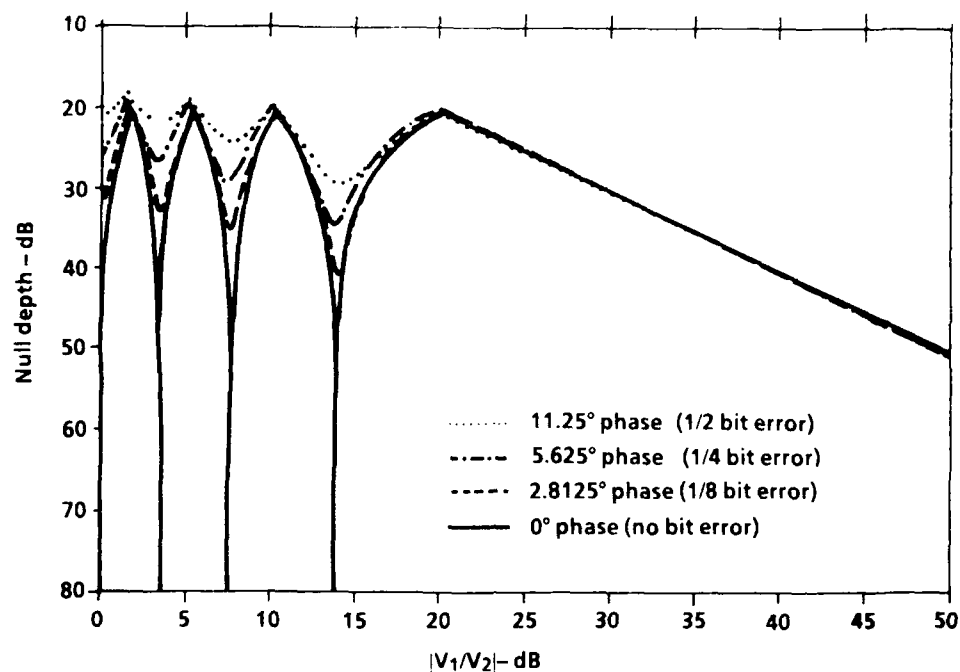


Figure 5. Polarization Combiner Predicted Null Depth; 4-Bit Phase Shifters; Input Voltage Phases Variable

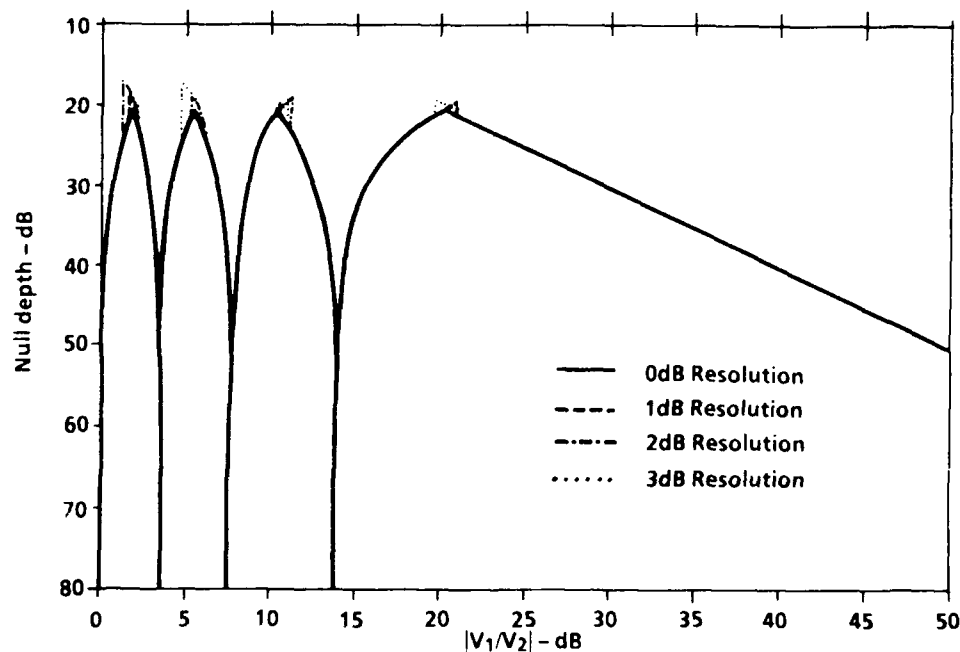


Figure 6. Predicted Null Depth; 4-Bit Phase Shifters; Input Voltages in Phase; Amplitude Detection Levels Variable

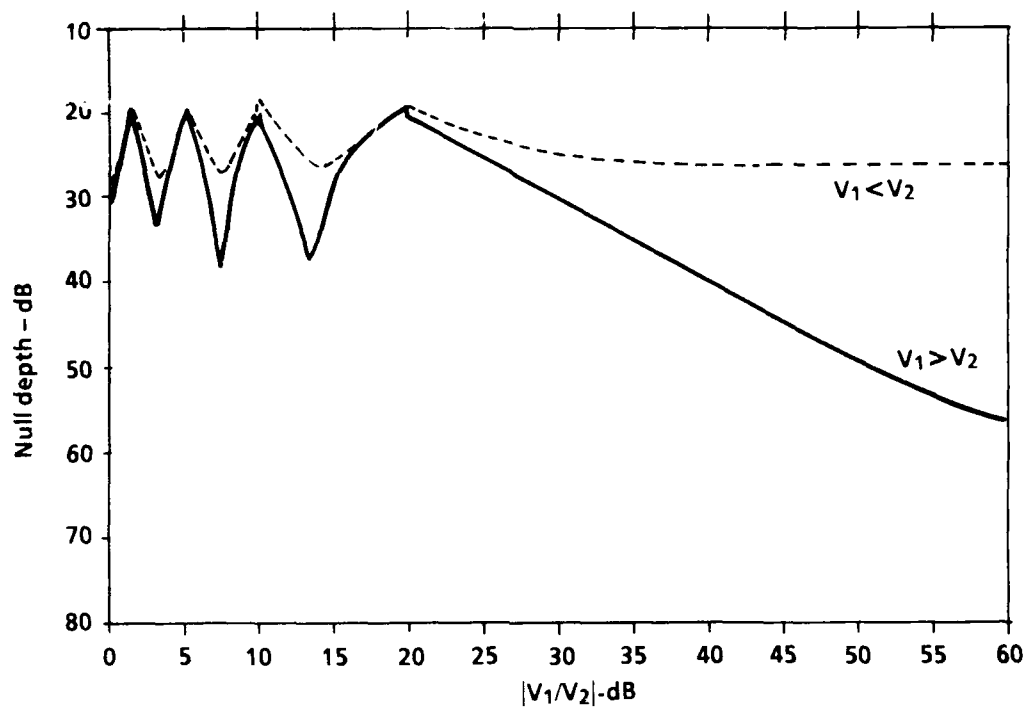


Figure 7. Polarization Combiner Predicted Null Depths; 4-Bit and 5-Bit Phase Shifter; Input Voltages in Phase, All Imbalances

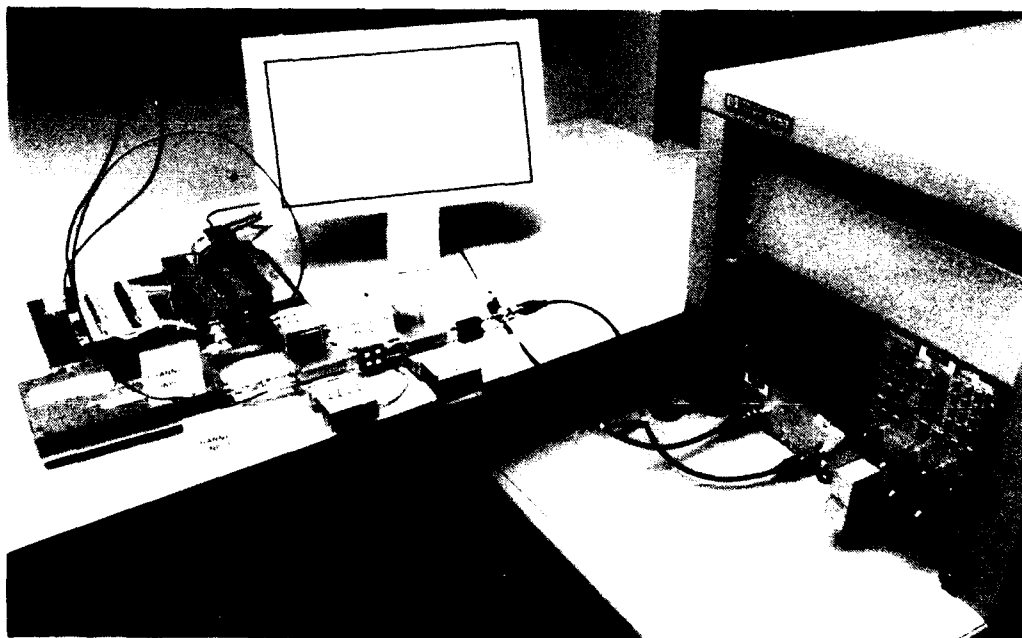


Figure 8. Photograph of Polarization Combiner Model Test Setup



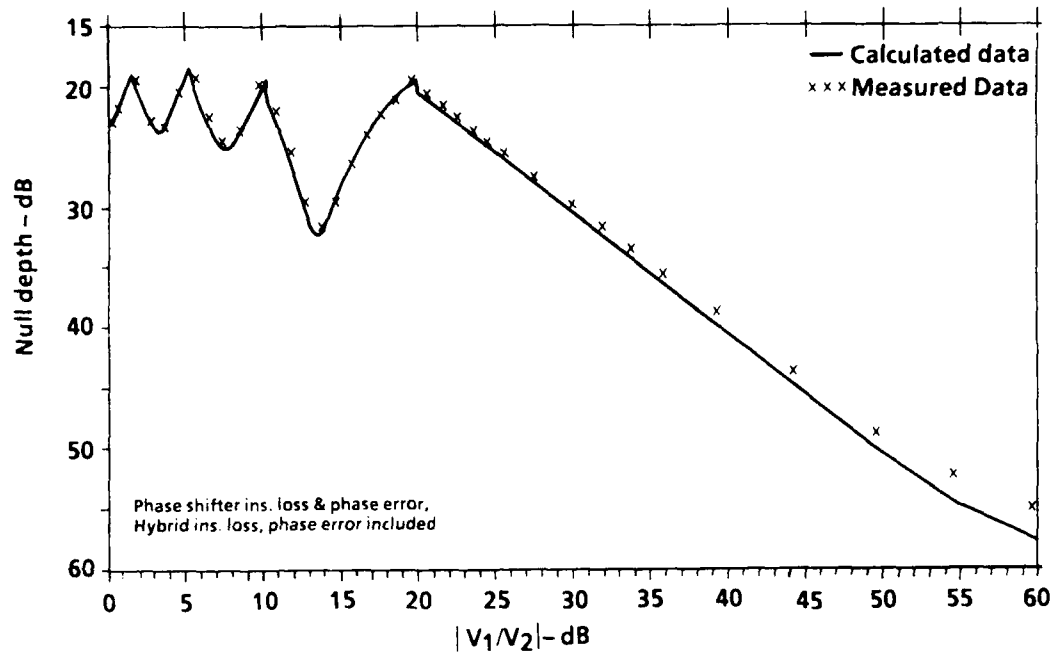


Figure 10. Comparison Between Calculated and Measured Null Depths; Combiner With 4-Bit Phase Shifters;  $80^\circ$  Input Voltage Phase Difference; 1 GHz

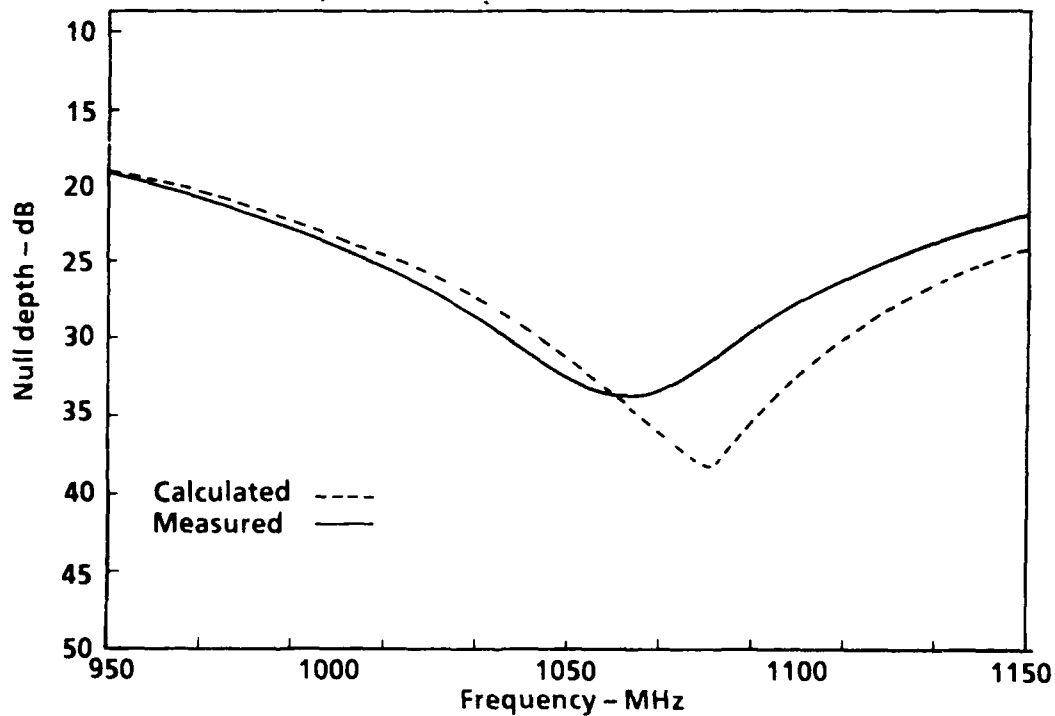


Figure 11. Measured and Calculated Null Depths.  $[V_1/V_2] = 10$  dB, at  $+40^\circ$  Phase

PERFORMANCE CHARACTERISTICS OF NOTCH ARRAY  
ELEMENTS OVER A 6/1 FREQUENCY BAND

George J. Monser  
Consulting Engineer

Raytheon Company  
Electromagnetic Systems Division  
Goleta, California

1987 Antenna Applications Symposium  
23-25 September 1987  
Monticello, Illinois

Sponsored by  
Electromagnetic Science Division  
Rome Air Development Center  
USAF Systems Command  
and  
Electromagnetics Laboratory  
University of Illinois

ABSTRACT

PERFORMANCE CHARACTERISTICS OF NOTCH ARRAY  
ELEMENTS OVER A 6/1 FREQUENCY BAND

George J. Monser

This paper presents pattern and gain characteristics for a notch array element over a 6 to 1 frequency band.

It is shown that the lower frequency limit occurs independently of the notch design, and that the upper frequency limit depends upon the element design.

Refinements to the design are discussed, leading to a design operable from 2.5 to 19.0 GHz.

PERFORMANCE CHARACTERISTICS OF NOTCH ARRAY  
ELEMENTS OVER A 6/1 FREQUENCY BAND

George J. Monser

1.0 INTRODUCTION

The dual-polarized array consisting of printed-notches in the walls of the horn elements was reported in the literature<sup>1</sup> where good performance characteristics were displayed over the continuous frequency band from 4 to 18 GHz. Since the printed notches appeared to have an even greater bandwidth, their bandwidth potential was checked.

This paper shows that the useful bandwidth for this type of printed-notch array is greater than 6/1 (i.e., 3 to 19 GHz); with further design, performance from 2.5 to 19 GHz may be realized.

2.0 THE TEST MODEL

Figure 1 shows a photograph of the dual-polarized array with the notches built into the walls of the horn elements. Each consists of four notches fed by a corporate power-divider structure as shown in Figure 2. The transformers within the dividers

1. Monser, G.J. (1984) Considerations for Extending the Bandwidths of Arrays Beyond Two Octaves. Paper presented at the Antenna Application Symposium.

were designed to work best over the 4 to 18 GHz range so that part of the element rolloff below 4 GHz is due to added divider losses which is further aggravated by increased coupling between the notch, sub-array elements.

### 3.0 TEST RESULTS

Two regions of bandwidth extension are reported; 18 to 19 GHz and 3 to 4 GHz. These extensions are then merged with the existing band.

#### 3.1 ABOVE 18 GHz

Figures 3 through 5 show patterns and swept gain on antenna boresight.

The array-plane patterns (smooth and broad) (Figure 3) shows that adequate coverage is provided for use as an array element.

In the elevation plane the patterns (Figure 4) are similarly acceptable.

Figure 5 shows that the gain is a smooth function with no drop-outs in gain.

#### 3.2 BELOW 4 GHz

Figures 6 through 9 show patterns and swept gain on antenna boresight.

The array-plane patterns (Figure 6) show that adequate broad coverage is provided for use as an array element.



Figure 7 shows that the elevation coverage is acceptable.

Figure 8 shows that the gain is a smooth function with no drop-outs in gain.

Active VSWR for this element is shown in Figure 9 showing that reasonably good transmission efficiency results even with the electrically close spacing between array elements.

### 3.3 FULL BAND

Figure 10 shows antenna element gain over the full band from 3 to 19 GHz.

Figure 11 shows the elevation coverage (orthogonal-to-array) from 3 to 19 GHz.

### 4.0 NOTCH DESIGN

The basic building block in the assembly shown in Figure 2 is the printed circuit notch. Each notch is excited by a strip-line, button-hook, capacitively coupled line (Figure 12). The feed-line cross-over position (distance to the notch) as well as the extension after cross-over and geometry (disk) were empirically determined for best active VSWR corresponding to a scan angle of  $\pm 30^\circ$ . Both active and passive VSWR's were measured over the 4 to 18 GHz band.

The slot-to-notch transition was then developed from a step to a flare-step configuration (Figure 13) which showed

improved passive match without affecting the active match. A total of four notches, spaced 0.42 inch between centers and fed by a four-way, equal-split divider comprise each array element. The equal power division was selected to yield the highest gain and two section transformers were designed and incorporated in the corporate feed to assure a good match at the input.

#### 5.0 DISCUSSION OF RESULTS

The upper frequency limit of 19 GHz is primarily due to pattern degradation although the transformers in the corporate feed are beyond their design band. The lower frequency limit of 3 GHz is primarily due to poor active match and low antenna gain. Active match increased primarily because the total coupling was insufficient to cancel the significant passive reflection coefficient associated with the electrically small notch. The low antenna gain is attributed to the poor passive match, a characteristic of electrically small antennas.

#### 6.0 CONCLUDING REMARKS

The feasibility of using notch array elements over a 6/1 frequency band has been demonstrated.

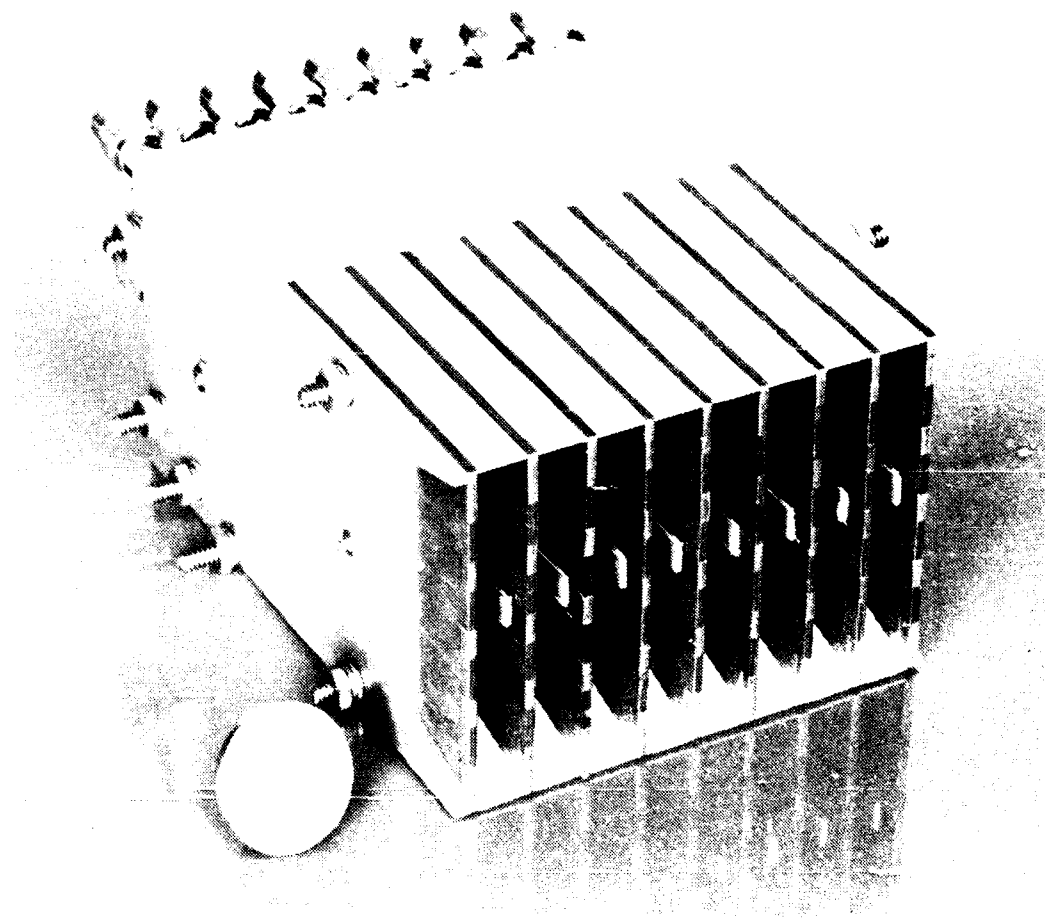


Figure 1. Dual Polarized Array

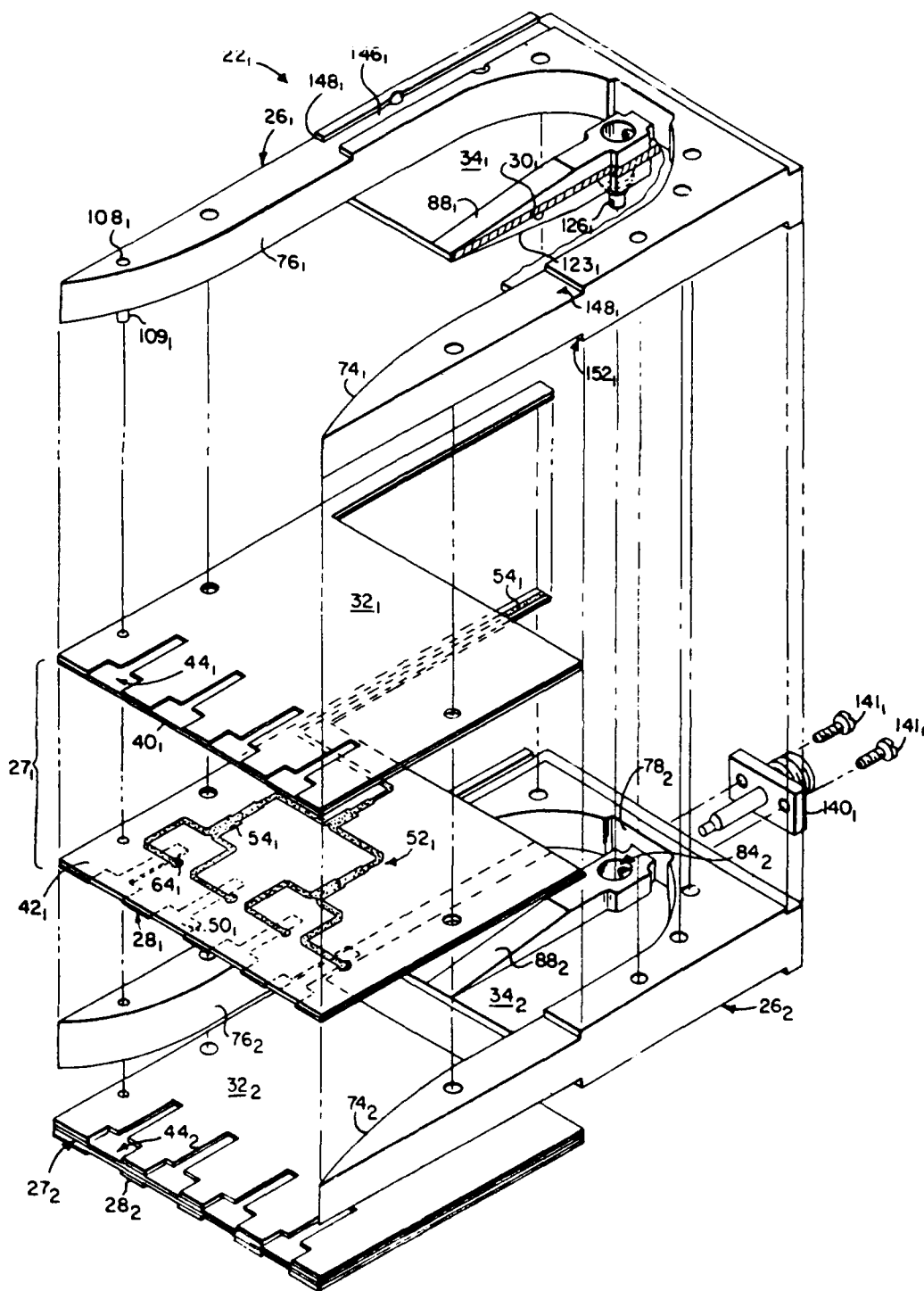


Figure 2. Strip-Line Array Corporate Feed

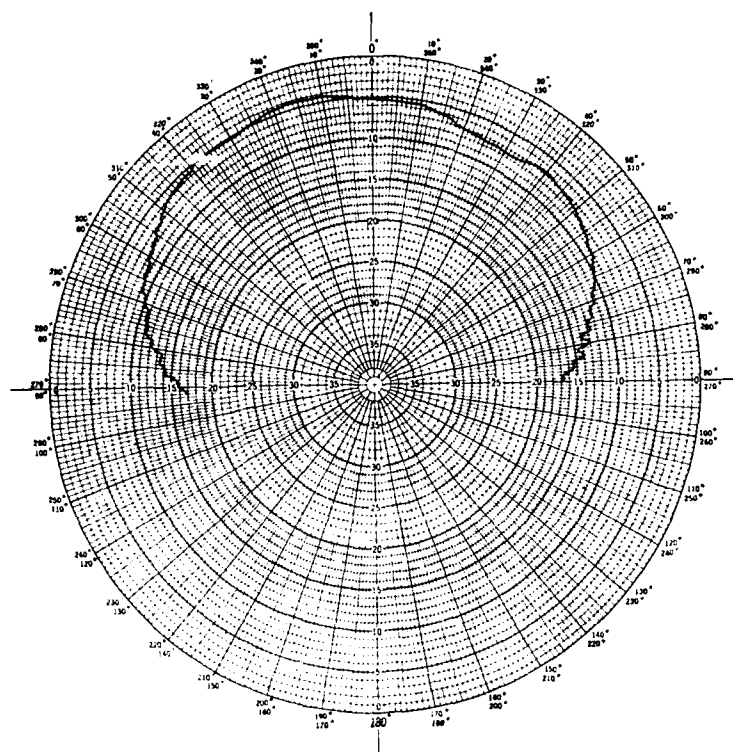


Figure 3. Array Plane Pattern (19.3 GHz)

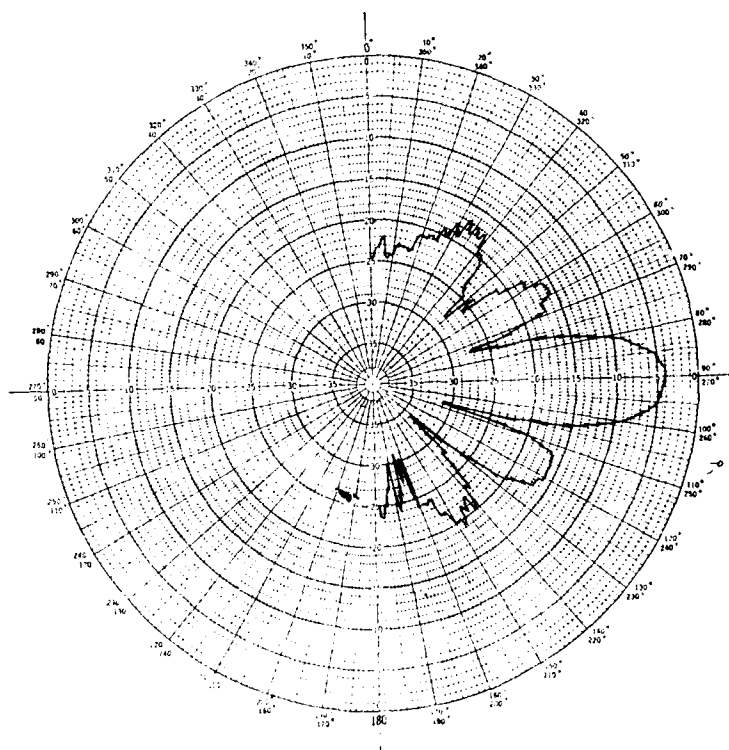


Figure 4. Elevation Plane Pattern (19.3 GHz)

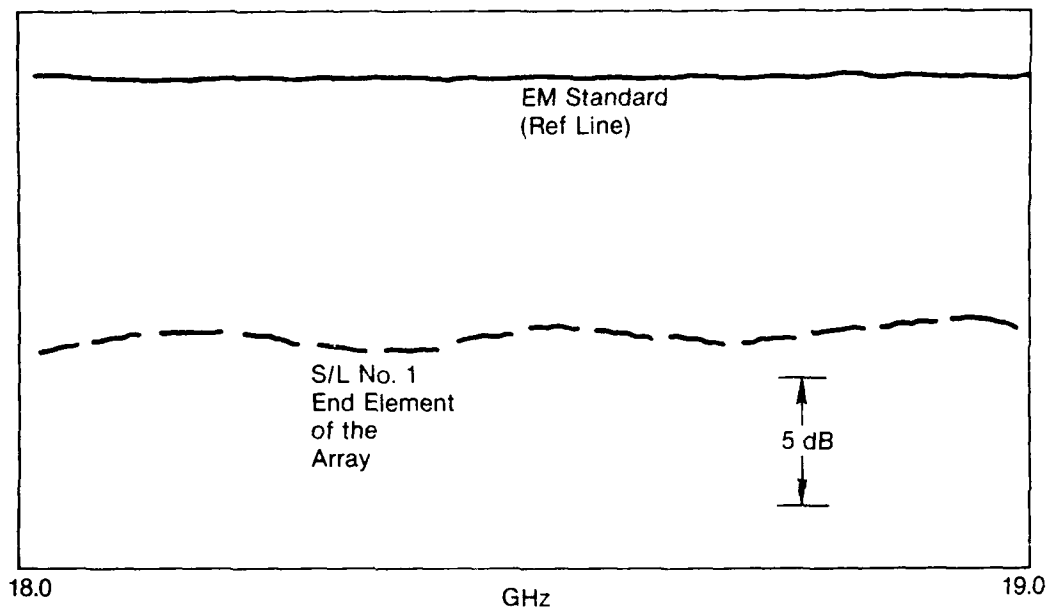


Figure 5. Element Swept Gain (18 to 19 GHz)

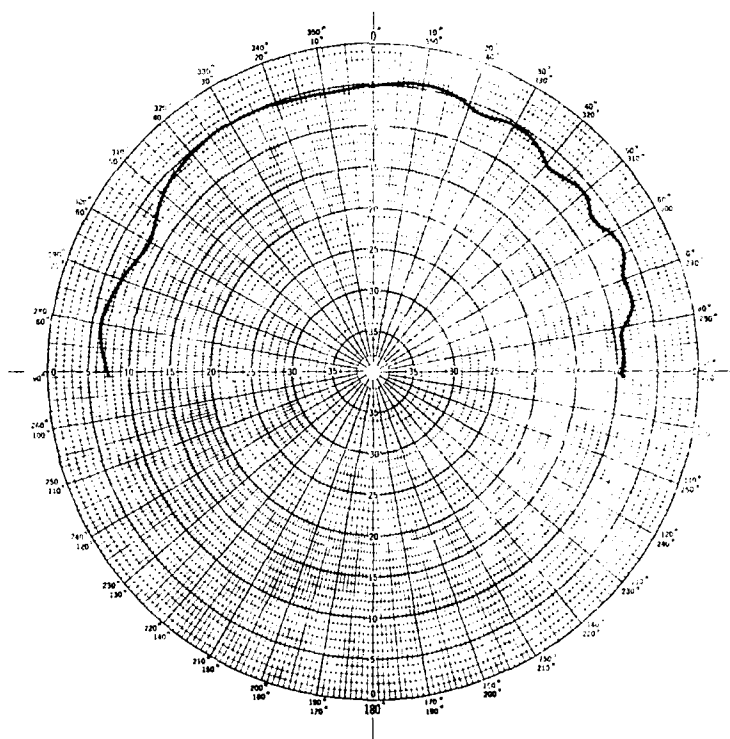


Figure 6. Array Plane Pattern (3 GHz)

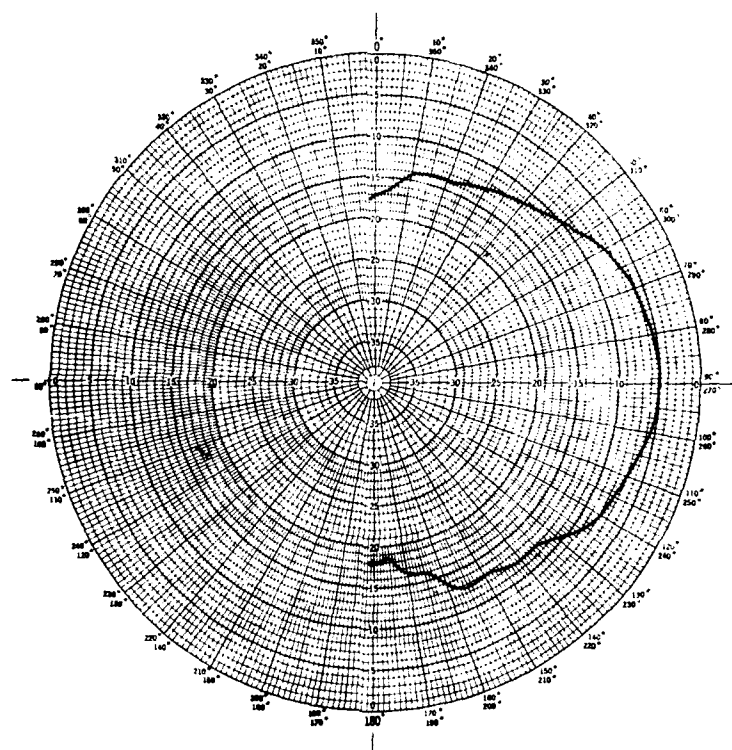


Figure 7. Elevation Plane Pattern (3.0 GHz)

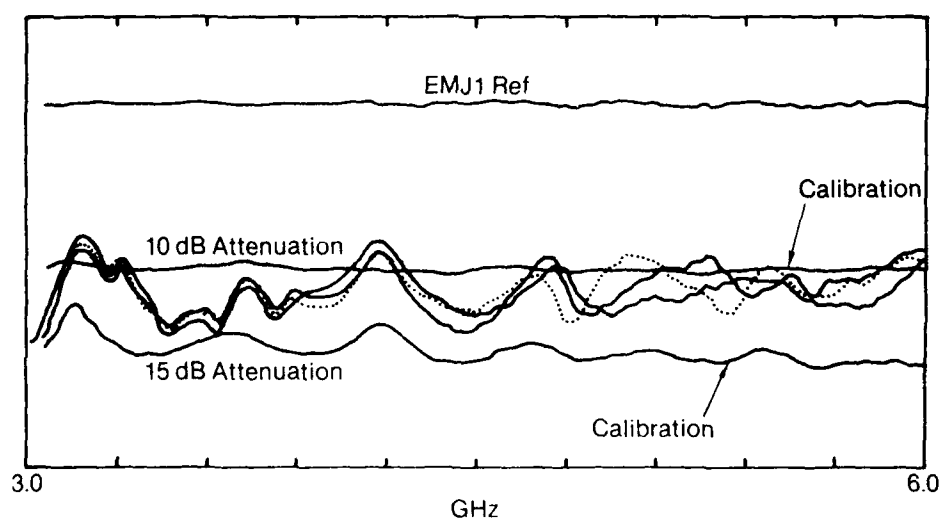


Figure 8. Element Swept Gain(s) Relative To Standard (3.0 to 6.0 GHz)

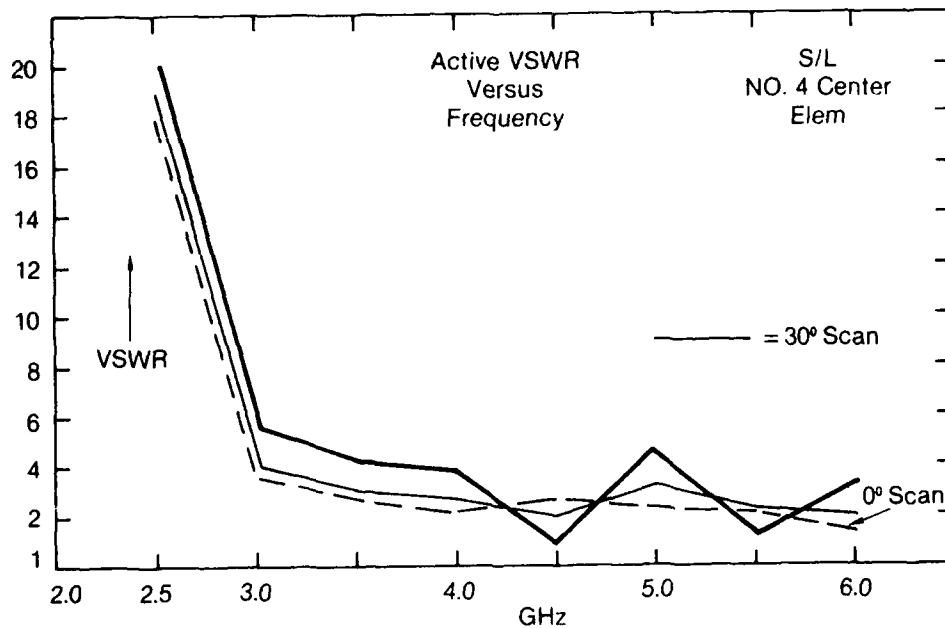


Figure 9. Active VSWR, 0° and 30° Scan, 2.5 to 6.0 GHz

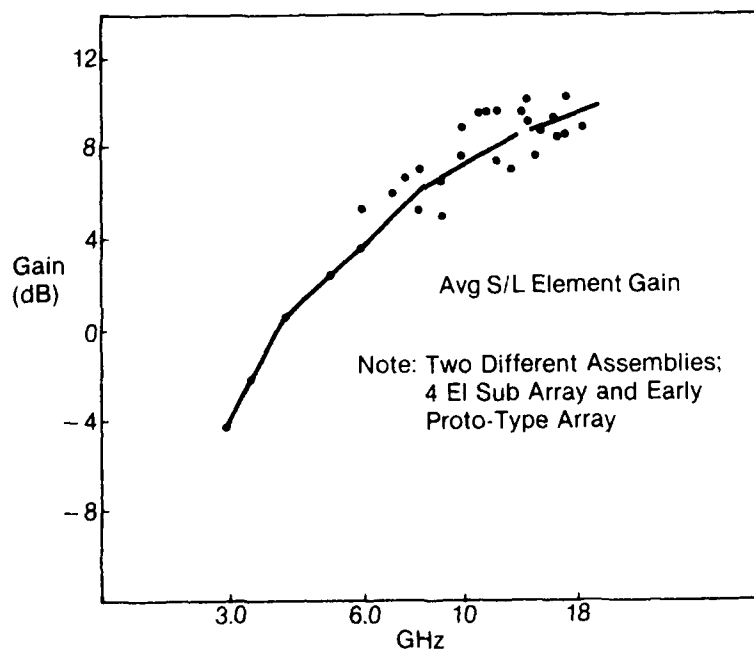


Figure 10. Element Gain, 3 to 19 GHz



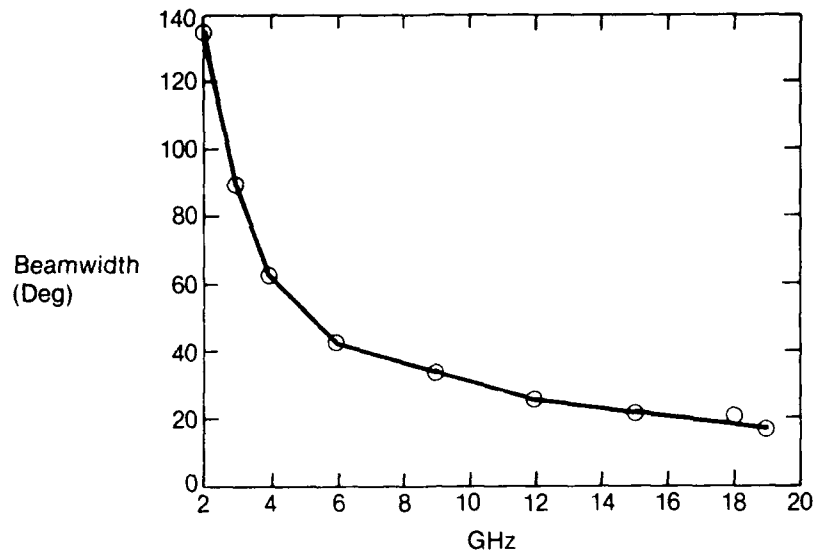


Figure 11. Elevation-Plane Half-Power Beamwidth (2 to 19 GHz)

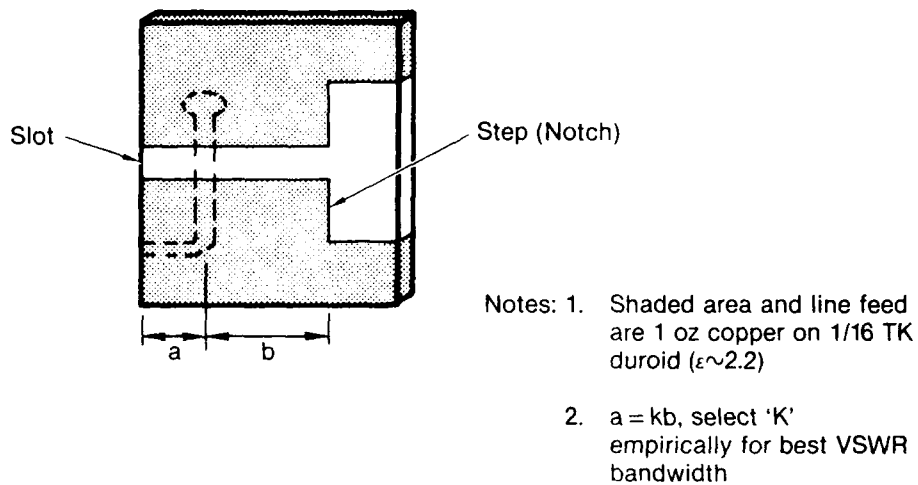


Figure 12. Button-Hook-Fed Coupling to Slot

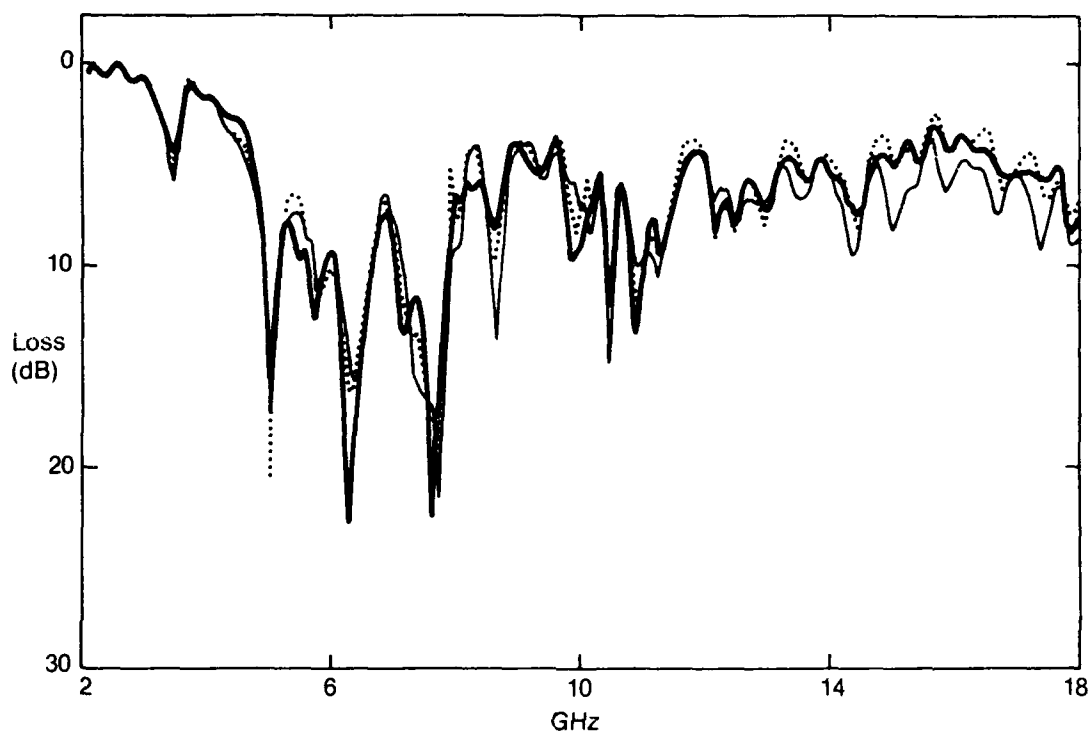


Figure 13. Passive Return Loss (2 to 18 GHz)

## AN ORBITER-ACTS COMMUNICATIONS EXPERIMENT

G. D. Arndt, L. Leopold, S. H. H. Chen - NASA/Johnson Space Center  
Y. C. Loh, Yeng S. Kuo, R. Shaw, J. Carl - LEMSCU

### Abstract

A proposed communication experiment between the Shuttle Orbiter and the ACTS (Advanced Communications Technology Satellite) is described. The experiment includes 20/30 GHz technology, a high gain antenna (52 dB) aboard the Shuttle, and two ground stations.

### Introduction

The Advanced Communications Technology Satellite (ACTS) is an experimental, geosynchronous satellite scheduled to be launched in 1991. This satellite, transmitting at 20 GHz and receiving at 30 GHz, provides spot beams to fixed ground locations within the United States. It also has a program steerable, 1 meter antenna which can communicate with spacecraft in low-earth orbit.

This paper describes a proposed communication experiment between the Shuttle Orbiter and the ACTS. The objectives of the experiment include (1) operate a high gain antenna (52 dB) with both autotracking and computer pointing in the dynamic environment of a maneuvering Orbiter, (2) develop and test space qualified antenna and RF technology at 20/30 GHz, and (3) evaluate multibeam communication links for direct distribution of high rate data for manned space applications. The experiments will involve the Orbiter, the ACTS, the Lewis Research Center Ground Station and the Johnson Space Center (JSC) Communications Test Facility.

Initial in-house studies have been funded using the Johnson Space Center's Director's Discretionary Funds for fiscal years FY87 and FY88. These studies included system sizing tradeoffs, Shuttle compatibility issues, 20 GHz electronic fabrication and testing, equipment/technology surveys, and costing. The study results are summarized in this paper.

#### ACTS Configuration

There are two possible modes of operation for the ACTS system. The first is the microwave switch matrix mode which provides a flexible format capability (Figure 1). A ground user transmits at 30

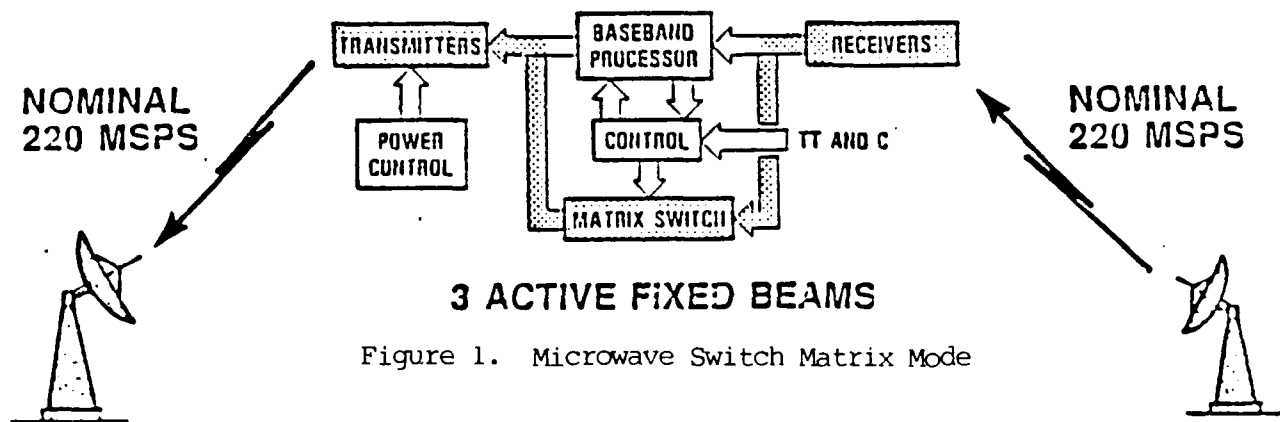


Figure 1. Microwave Switch Matrix Mode

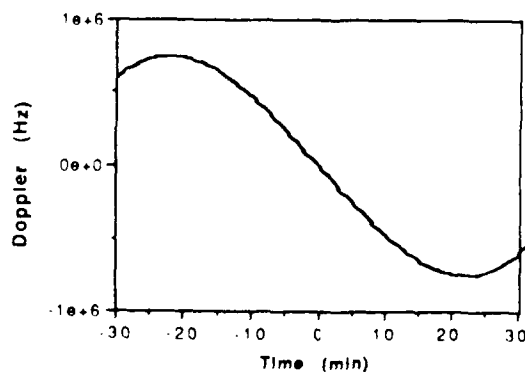
GHz to the satellite receiver, through the microwave switch, to the 20 GHz transmitters, and then down to a ground station. The matrix switch in ACTS is a 4\*4 switching system with one redundant channel. This makes a 3\*3 matrix switch available to the user. The switch can handle up to three distinct antenna inputs at any one time, regardless of the signal origin. Three different signals can come

from any of the three fixed beams, the East scanning beam, and/or the West scanning beam. Although the scanning beam can be in only one place at a time, it can move to different locations within the sector. The beam can hop around continuously - up to 40 times in a given frame. Basically, this is a bent-pipe mode and any modulation type in either a TDMA or FDMA format can be supported. The frequency plan accommodates 900 MHz of useable bandwidth, permitting the transmission of a very high burst rate signal, as well as a very low burst rate signal.

The second method of operation is a baseband processor mode in which the signal is detected, processed at baseband, and then remodulated onto the downlink carrier. Because the proposed experiment is Space Shuttle based, the relative velocity between the transmitting and receiving antennas varies drastically, thereby causing large doppler shifts. Figure 2 shows the doppler profile for the proposed experiment. The maximum doppler shift during the experiment is approximately 700 KHz which exceeds the operating capability of the baseband processor.

Figure 2.

**Doppler (SSO-ACTS worst cast @ 29.5 GHz)**



### Experiment Configuration

Because of frequency spectrum congestion, future high capacity communication links are moving towards Ka-band (or higher) frequencies. A high frequency, high data rate link to a low-earth-orbit (LEO) spacecraft presents unique requirements not seen in previous programs. This experiment is intended to provide answers to the following questions:

(1) How to acquire and track very narrow beams of RF signals at 20/30 GHz in the dynamic environment of an orbiting vehicle? The dynamic environment consists of position changes as the vehicle moves along its trajectory as well as attitude changes when reaction control system (RCS) jets are fired to maintain a given attitude. The obvious platform to carry out this test is the Space Shuttle Orbiter, which has an orbital velocity of about 7.5 Km/sec and a maximum attitude rate of  $9^{\circ}$ /second.

(2) What is the technology required to provide efficient high gain antennas that will perform in this environment? Some specific concerns are surface tolerances, feed design, and tracking mechanism needed to provide the tight pointing accuracy required.

(3) How readily available is the RF technology and what kind of risk is involved to develop space qualified components such as low noise amplifiers at 20 GHz and high power TWAs at 30 GHz? What is the noise figure and DC to RF efficiency of these devices?

(4) What kind of working environment will the satellite's multibeam architecture provide for direct distribution of high rate data for applications such as the Space Station?



The experiment is designed for the maximum data rate possible under the constraint that the antenna onboard the Orbiter must be small enough to fit inside the payload bay. The system parameters of the ACTS are summarized in the following tables:

ACTS TRANSMITTING	TO ORBITER	TO ESTL	TO LeRC
Diameter	1 m	3.3 m	3.3 m
Gain	such 42 dB	50 dB	51 dB
TWTA Transmitter	10 W/43 W	Same	Same

ACTS RECEIVING	From Orbiter	From ESTL	From LeRC
Diameter	1 m	2.2 m	2.2 m
Gain	45 dB	50 dB	51 dB
LNA Noise Figure	5 dB	Same	Same

With these parameters, the goal is to design a system that is able to support slow scan TV (5 MBPS) for the uplink and full motion color TV (50 Mbps) for the downlink during the test. A more detailed configuration is shown in Figure 4 where ESTL will be the



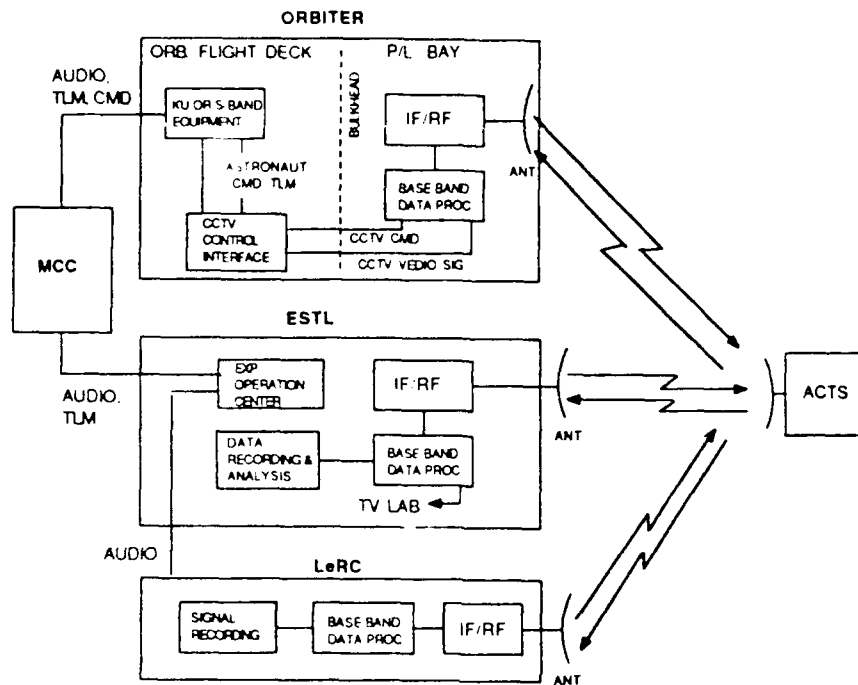


Figure 4. - Detail Experiment Setup

experiment operations as well as the data analysis center. Commands and telemetry are routed to the Orbiter via the S-band or Ku-band system and coordination with LeRC will be by prior arrangement and real time audio circuits. System configurations for each of the ground stations are shown in Figure 5. The uplink data from ESTL will be either 5 Mbps of PN code or digitized slow scan TV which will be BPSK modulated onto the 29.6 GHz carrier. The ESTL power amplifier will be a 10 W TWTA and the antenna will be a 1.8 m reflector with monopulse feed. The ESTL ground receiver will receive a rate 1/2, convolutionally encoded 55 Mbps (110 Mbps total) signal at 19.7 GHz. This unbalanced QPSK signal will be demodulated into the I/Q components. If PN sequences are transmitted, bit error

rate measurements will be performed while the uplink and downlink RF powers are varied. If a TV signal is transmitted, the base band data will be routed to the TV laboratory at the Tracking and Communication Division at JSC for evaluation of future EVA/Space Station applications. The LeRC station will be an adjunct to the ESTL site and will mainly be used to evaluate the effect of real time routing of the 110 Mbps data by ACTS switching network. Its equipment will consist of an uplink modem using a 5 Mbps PN generator as the data source while the receiver will consist of a QPSK demodulator and a high data rate recorder where the data will be saved for post analysis. The BPSK signal sent from either of the ground stations will be demodulated in the Orbiter receiver and then turned around to modulate the Q channel of the downlink QPSK signal. If slow scan TV is used as the uplink, the signal will be converted to the Orbiter CCTV format and distributed via the CCTV network. The 50 Mbps high rate data will be generated either from a PN generator or via a special TV signal digitizer. The TV signal obtained from the Orbiter CCTV system allows the crew to select any of the cameras located in the payload bay. This signal will then be used to modulate one channel of the modulator.

The antenna used in the Orbiter is the same 1.8 m antenna used in ESTL except that it will be mounted inside the payload bay for safety reasons as shown in Figure 6. Although the scan angle is limited and the pattern is affected by the bulkheads of the payload bay, the cost is minimized by not mounting the antenna on a moveable boom.

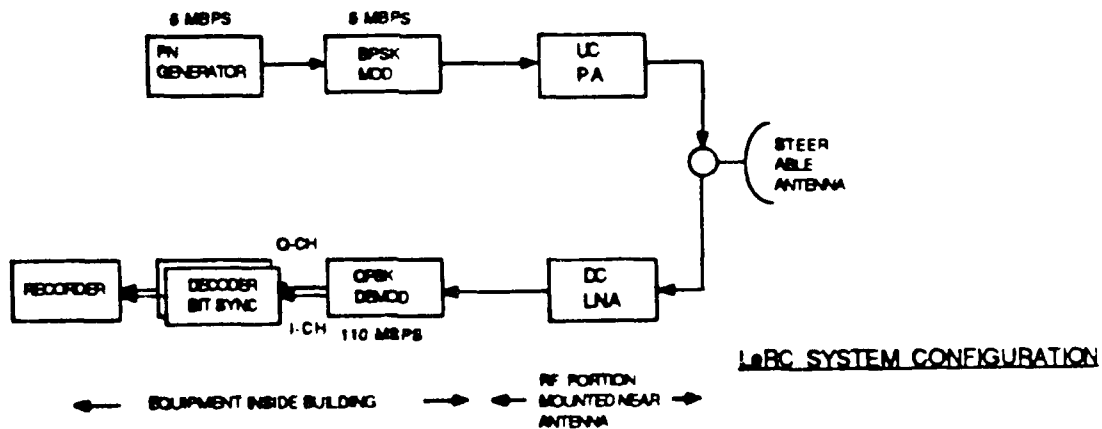
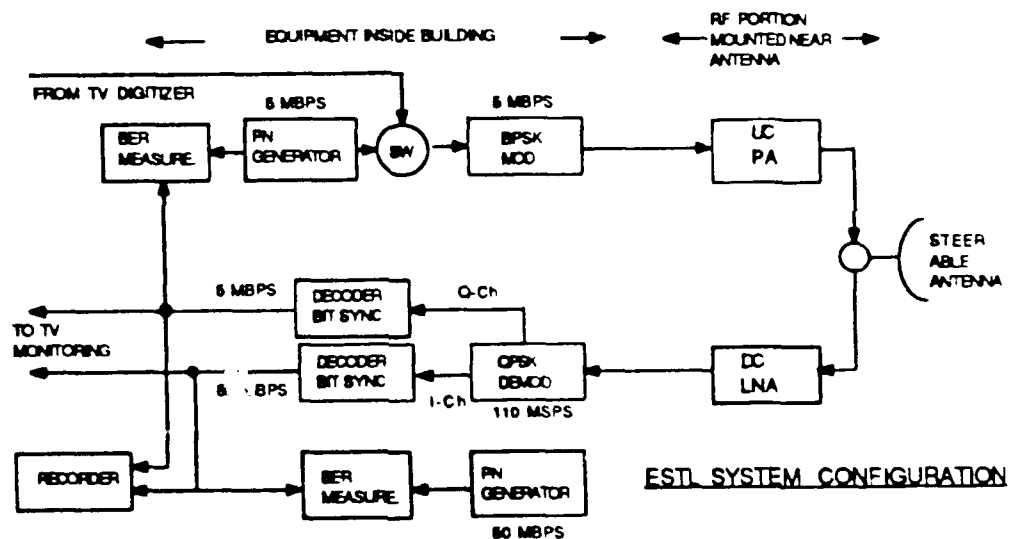
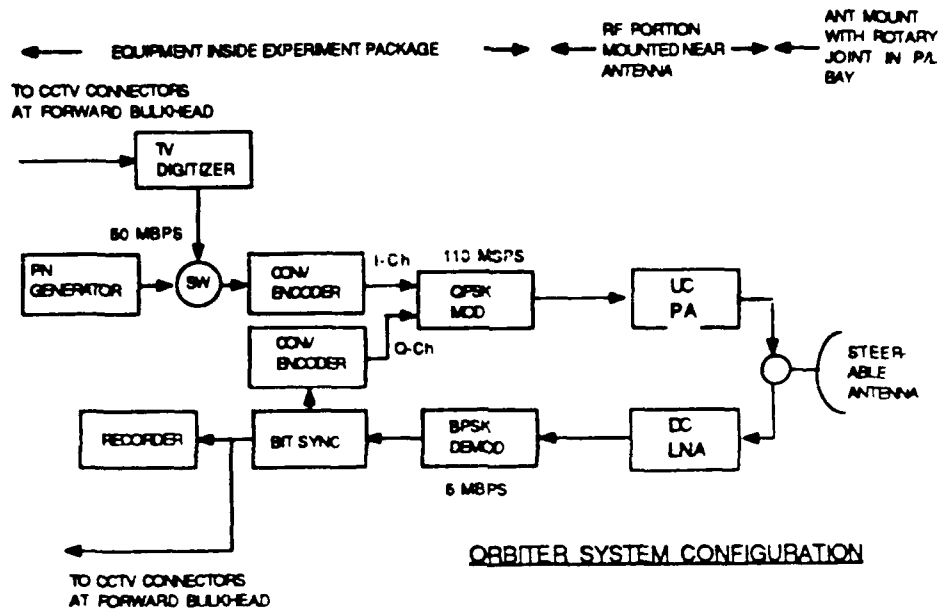


Figure 5: Ground Stations and Orbiter Systems

# ANTENNA AND EXPERIMENT PLACEMENT

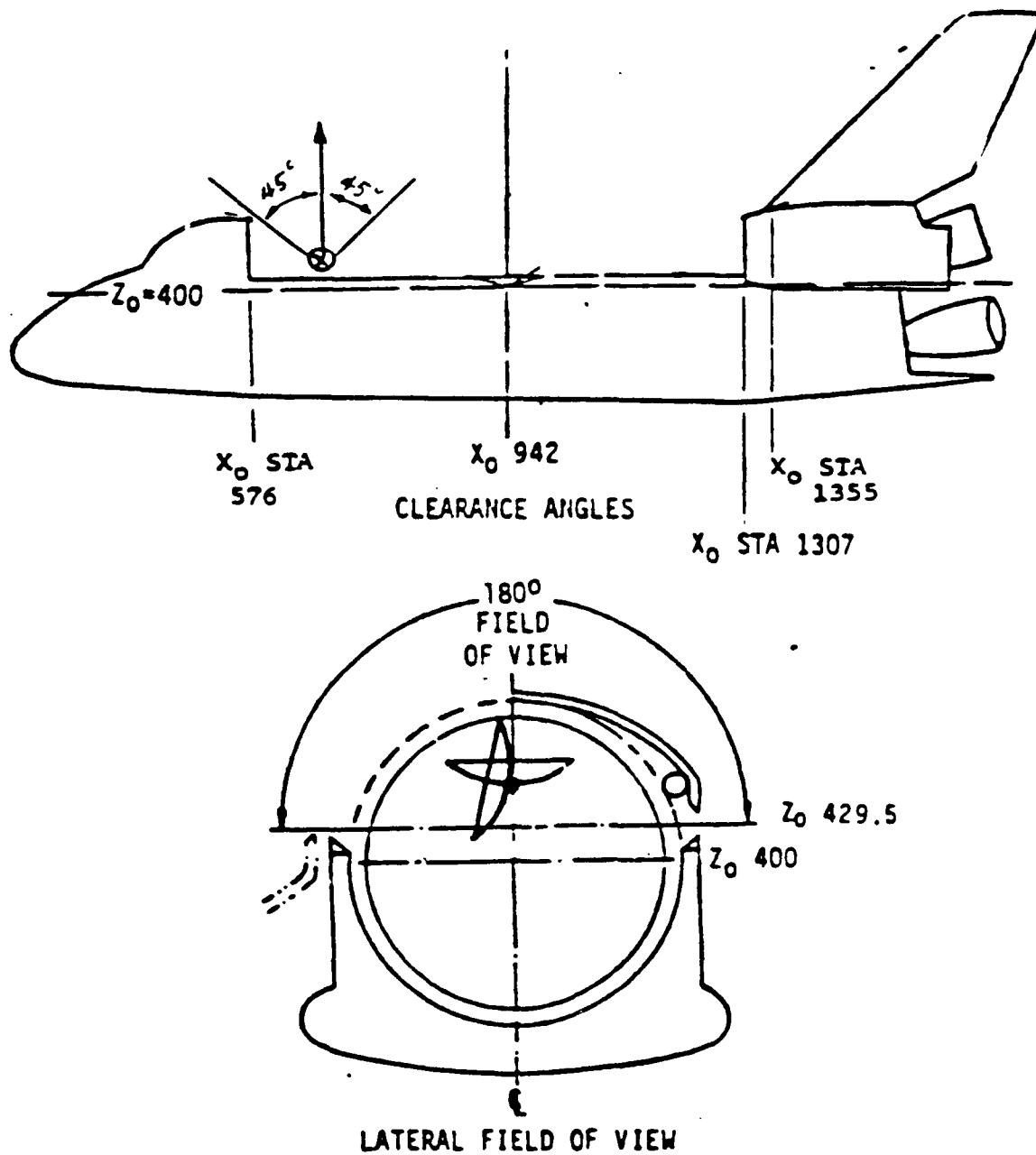


Figure 6. Antenna and Experiment Placement

With the links configured as shown in Figures 4 through 6, the performance is satisfactory between all the stations and the Orbiter. Using a 50 watt TWTAs, 30 GHz transmitter on the Orbiter, the worst case downlink channel (50 Mbps) has 5.7 dB of RF circuit margin as given in Tables A and B. A summary of the requirements for the different types of antennas is given below. Development efforts will concentrate on the 1.8 m antenna, low noise amplifiers, TWTAs, and the necessary baseband equipment.

Summary of Antenna and TWTAs Power Requirements

	SSO to ACTS	ACTS to SSO
Pt (W)	50	43
TX Ant (m)	1.8	1
Polarization	Circular	Horizontal
Pointing Accuracy	$\pm 0.06^\circ$	$\pm 0.15^\circ$
RX Ant (m)	1	1.8
Polarization	Vertical	Circular
Pointing Accuracy	$\pm 0.1^\circ$	$\pm 0.09^\circ$
Circuit Margin (dB)	5.7	8.0
	ESTL to ACTS	ACTS to ESTL
Pt (W)	10	43
TX Ant (m)	1.8	3.3
Polarization	Vertical	Horizontal
Pointing Accuracy	$\pm 0.06^\circ$	$\pm 0.05^\circ$
RX Ant (m)	2.2	1.8
Polarization	Vertical	Horizontal
Pointing Accuracy	$\pm 0.075^\circ$	$\pm 0.09^\circ$
Circuit Margin (dB)	11.7	12.0

#### Hardware Studies

As part of the initial definition of the experiment, several in-house studies into hardware availability are underway. Results to date are summarized:

TABLE A

CIRCUIT MARGIN - SSO to ACTS (50 mbps Channel)

Pt @ 50 W	17.0	dBW
Ckt Loss	-2.0	dB
Polarization Loss (circular to vertical)	-3.0	dB
Pointing Loss ( $\pm 0.06^\circ$ SSO, $\pm 0.1^\circ$ ACTS)	-0.5	dB
TX antenna, 1.8 m @ 50% $\eta$	52.0	dB
EIRP	63.5	dBW
Path loss (30 GHz, 22000 nmi)	-214.2	dB
RX antenna, 1m @ 30% (per RCA)	45.0	dB
Ckt Loss	-3.0	dB
Total Rec. Power	-108.7	dBW
QPSK modulation loss (80 %)	-1.0	dB
QPSK demodulation loss	-1.0	dB
Ts (5 dB NF, Ta = 290° K)	29.6	dBK
N <sub>o</sub>	-199.0	dB(W/Hz)
Bit rate bandwidth (50 Mbps)	77.0	dBHz
E <sub>b</sub> /N <sub>o</sub> in bit rate bandwidth	11.3	dB
Req'd E <sub>b</sub> /N <sub>o</sub> ( $10^{-5}$ BER)	9.6	dB
Coding gain (r=1/2, k=7)	5.0	dB
Bit sync Loss	-1.0	dB
Actual E <sub>b</sub> /N <sub>o</sub> required	5.6	dB
Margin	5.7	dB

TABLE B

CIRCUIT MARGIN - ACTS to ESTL (50 mbps Channel)

Pt @ 43 W	16.3	dBW
Ckt Loss	-3.0	dB
Polarization Loss (both are horizontal)	-1.0	dB
Pointing Loss ( $\pm 0.05^\circ$ ACTS, $\pm 0.09^\circ$ ESTL)	-0.5	dB
TX antenna, 3.3 m fix mounted on ACTS	50.0	dB
EIRP	61.8	dBW
Path loss (20 GHz, 22000 nmi)	-210.7	dB
RX antenna, 1.8 m @ 50% $\eta$ at ESTL	48.5	dB
Ckt Loss	-2.0	dB
Total Rec. Power	-102.4	dBW
QPSK modulation loss (80 %)	-1.0	dB
QPSK demodulation loss	-1.0	dB
Ts (5 dB NF, Ta = 290° K)	29.6	dBK
N <sub>o</sub>	-199.0	dB(W/Hz)
Bit rate bandwidth (50 Mbps)	77.0	dBHz
E <sub>b</sub> /N <sub>o</sub> in bit rate bandwidth	17.6	dB
Req'd E <sub>b</sub> /N <sub>o</sub> ( $10^{-5}$ BER)	9.6	dB
Coding gain (r=1/2, k=7)	5.0	dB
Bit sync Loss	-1.0	dB
Actual E <sub>b</sub> /N <sub>o</sub> required	5.6	dB
Margin	12.0	dB

(1) Low-Noise Amplifier - One of the key components in the implementation of the ACTS experiment is the receiver low-noise amplifier. This low-noise amplifier should add minimum noise power to the received K-band signal for the system to achieve maximum signal-to-noise ratio. In addition, the gain of the LNA should be high enough to mask second stage noise contributions of the filters, mixers, and pre-amplifiers.

Due to the recent advances in HEMT (high electron mobility transistor) device technology, development of a prototype hybrid microwave integrated amplifier has been undertaken at NASA/JSC. This amplifier has been implemented using a 0.5 micron gate length HEMT device. The design goals for the single-stage amplifier unit are a gain of 7 dB and a noise figure of 4.5 dB. The amplifiers have been realized in a single-ended configuration with maximum power gain matching networks on the input and output. The complete low-noise amplifier is a 3-stage cascaded circuit with interstage gain compensation networks to achieve  $20 \pm 1$  dB gain and 5.0 dB noise figure.

(2) Pan-Tilt Units vs. Gimbals - Gimbals are normally used for closed loop tracking and positioning applications of high gain, spaceflight antennas. After being space qualified, gimbals are very reliable and efficient during acquisition and tracking maneuvers. However, the cost can reach \$3M to \$8M for design, development, testing, and space qualifying of the gimbals and associated control electronics.



A possible alternative to the gimbals are pan-tilt devices employing stepper motors. The pan-tilt unit makes use of a rotary incremental activator to produce a simple and flexible way of gimbaling a load. The rotary incremental activator is a compact, closely integrated design made up of two key elements - a motor and a harmonic drive. These activators have been used in such varied applications as antenna deployment mechanisms, latching devices, large mirror positioning systems, antenna gimbal drives, and instrument pointing.


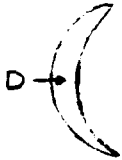
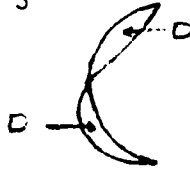
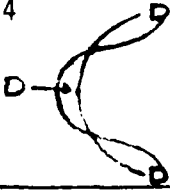
If a pan-tilt unit can operate efficiently for monopulse tracking applications of large space antennas, the cost advantage over a conventional gimbal system makes it an attractive alternative for this experiment. A detailed engineering comparison of the two techniques is underway.

#### Orbiter Antenna Design Considerations

The requirement for a large Orbiter antenna at 20/30 GHz may conflict with the general Orbiter requirement for a light weight design. A simulation program was developed to ascertain the requirements for rigidity, smoothness, and mechanical precision in the 1.8 meter reflector and feed in order that 50 dB could be reliably obtained from the antenna. It is assumed that the antenna uses a four horn monopulse autotrack feed with the feed cluster located directly above the reflector's vertex. For the sake of compactness, a shallow F/D of 0.35 was assumed. The aperture

illumination  $AI(r)$  is given by:  $AI(r) = 1 - (r/r_m)^2$  where  $r$  is the local radius and  $r_m$  is the maximum radius. An overall efficiency of 40% is assumed.

Table C  
Effects of Reflector Deformation on Antenna Performance

Deformation Type	D(mm)	Effect on Radiation Pattern
Type 1 	2	Loss of Boresight Gain = 0.22 dB Beam Shift $\approx 0.07^\circ$ (in AZ)
	4	Loss of Boresight Gain = 0.99 dB Beam Shift $\approx 0.14^\circ$ (in AZ)
Type 2 	2	Loss of Boresight Gain = 0.19 dB Beam Shift = $0.0^\circ$
	4	Loss of Boresight Gain = 1.34 dB beam Shift = $0.0^\circ$
Type 3 	2	Loss of Boresight Gain = 1.68 dB Beam Shift $\approx 0.2^\circ$ (in AZ)
	4	Loss of Boresight Gain = 7.9 dB Beam Shift $\approx 0.4^\circ$ (in AZ)
Type 4 	2	Loss of Boresight Gain = 1.36 dB Beam Shift = $0.0$
	4	Loss of Boresight Gain = 7.39 dB Beam Shift = $0.0$

#### a. Reflector Deformations

Reflector deformations may be caused by thermal, mechanical, or inertial stresses, or by distortion from a true parabola during the fabrication process. Representative deformations and the associated degradations are summarized in Table C. A typical gain versus degradation plot is shown in Figure 7.

Types 2 and 4 are radially symmetrical deformations and consequently, produce gain loss but no beam shift. Types 1 and 3 produce both beam shift and gain loss. The results indicate a reasonable distortion limit of 2 mm produces .2 to 1.7 dB of antenna loss, depending upon the particular type of deformation.

#### b. Surface Roughness

Figures 8 and 9 indicate that the surface of the reflector should be smooth to within approximately one-half millimeter (1mm) in order to keep the gain degradation to 0.3 dB and the first side lobe level increase to 1.5 dB. The surface material and fabrication technique must, therefore, be capable of obtaining and maintaining smoothness to 0.5 mm or less.

#### c. Lateral Feed Mislocation

Lateral feed mislocation is defined here as a mislocation along any line orthogonal to the boresight axis of the reflector. Displacement is in the "y" or "Azimuth" direction. For small lateral feed mislocation, the principle effect is beam steering as

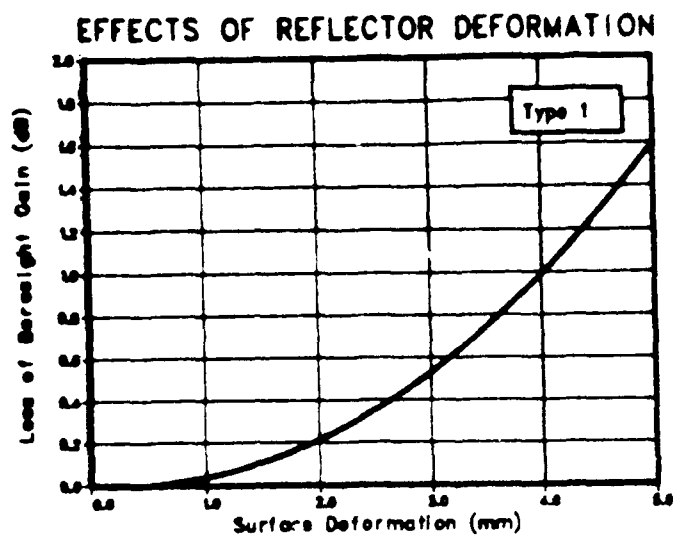


Figure 7.

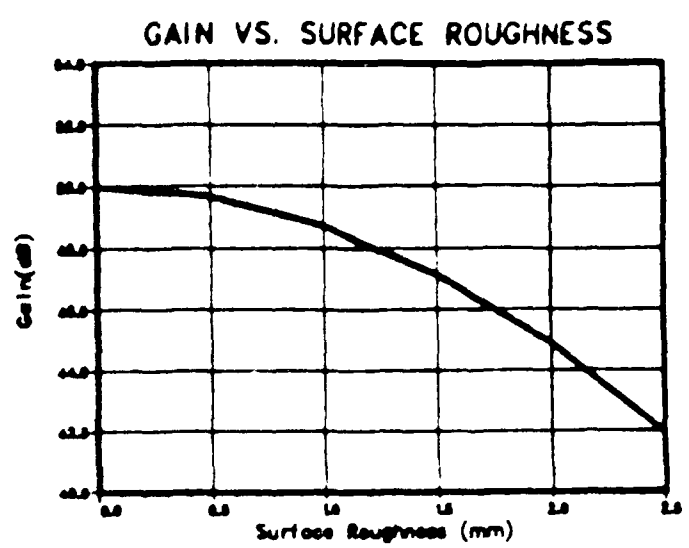


Figure 8.

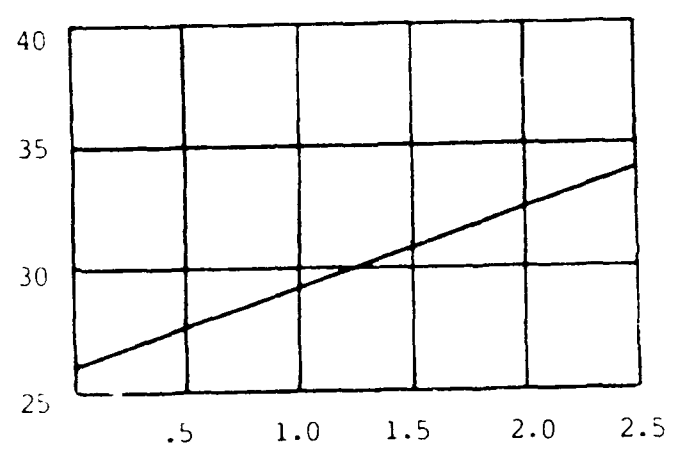


Figure 9.  
First Side Lobe Level vs. Surface Roughness

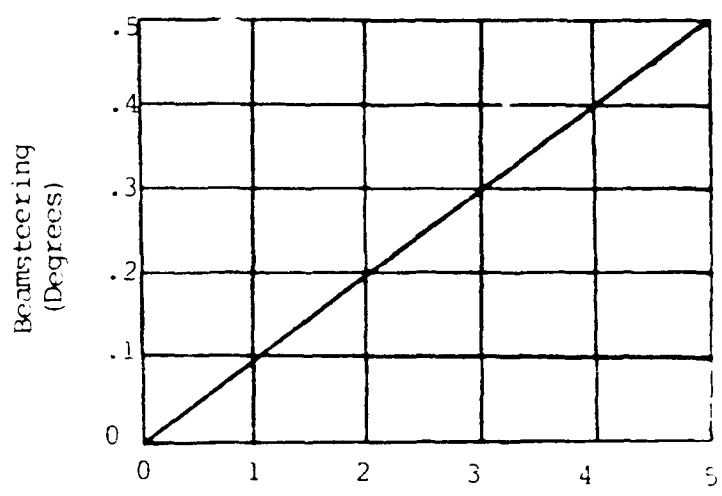


Figure 10.

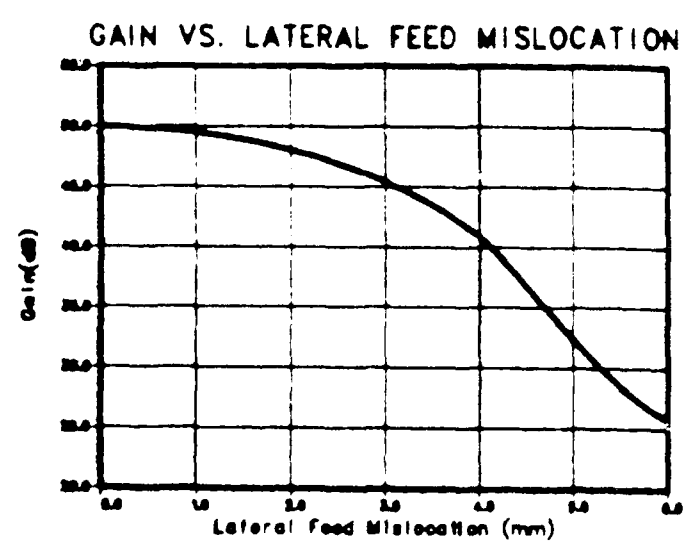


Figure 11.

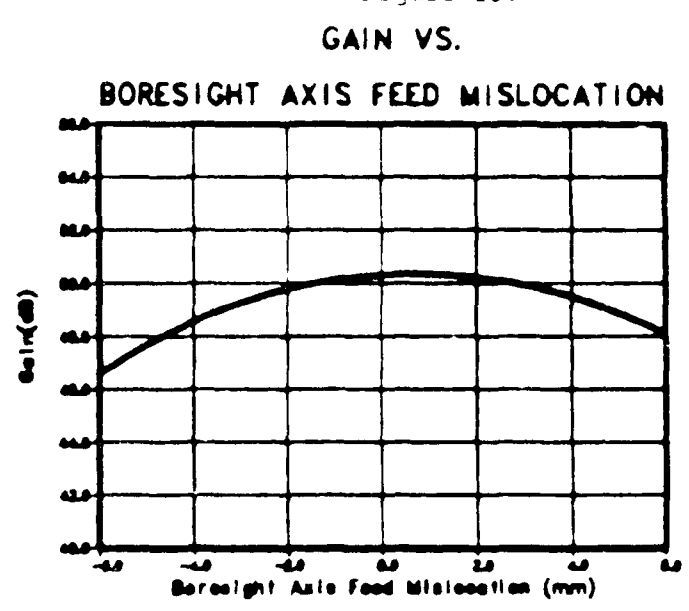


Figure 12.

shown in Figure 10 with little loss of peak gain. However, loss of boresight gain can result as can be seen from Figure 11.

d. Boresight Axis Feed Mislocation

Feed mislocation "in" or "out" along the reflector boresight axis causes defocusing of the antenna. This results in a loss of gain and a smearing of the first sidelobe into the main beam. (It is interesting to note that the smearing effect starts to occur before serious gain loss. This phenomenon could be used to avoid false tracking on the first side lobe.) This type of feed mislocation does not cause the beam to shift from boresight. Figure 12 shows the relationships between boresight axis feed mislocation and gain.

Summary:

A 20/30 GHz experiment between the ACTS and the Orbiter is technically feasible with much of the spacecraft hardware derived from ground equipment already developed as part of the ACTS program. The experiment can be self-contained, with no scarring to the Orbiter. In addition to the space flight aspect of operating a high gain, high rate data system from the Orbiter, the advantages of direct satellite broadcast to the Johnson Space Center can be evaluated.

MOM Analysis of a Finite Length Slot  
In an Infinite Conducting Sheet

Henry A. Karwacki

Sanders Associates, Inc.  
Nashua, New Hampshire, 03061

Abstract

This paper presents a method of moments analysis of a finite length and width slot in an infinite conducting sheet.

The analysis uses entire domain basis and testing functions (i.e. sinusoids) and image theory to model the scattering from a finite length and width slot in a ground plane for an incident TM wave.

The computations performed for a single cosine basis function and for a five term summation demonstrated very little difference since all higher order terms were 9 dB or more below the first term. The solutions also demonstrated that the form of the scattered far field was the same as the far field of a radiating rectangular aperture.

## 1. Introduction

The scattered field from a narrow width, finite length slot in an infinite perfectly conducting sheet excited by an incident transverse magnetic (TM) plane wave (as shown in Figure 1) is examined. A method of moments solution is formulated using entire domain basis functions with a Galerkin testing procedure. It is of interest to quantitatively compare the relative amplitudes of the higher order slot mode excitations to the lowest order slot mode. It is evident that the entire domain expansion needed converges very rapidly.

The inner products which fill the system matrix usually involve two sets of integrations, in this formulation the inner products are reduced to a single set of numerical integrations thereby conserving computer resources. If the field produced by the slot magnetic current is considered as the convolution of the current with the free space Green's function, it is possible to interchange the testing function and the Green's operator through a proper change of variables. The Green's operator will then act on the convolution of the currents and the testing functions. This formulation can also be used to compute the self-

impedance of a dipole or slot or the mutual impedance between two dipoles<sup>[1,2]</sup>.

## 2. Formulation

Consider a slot which is oriented as shown in Figure 1 on a perfectly conducting sheet of infinite extent in the x and y dimensions and vanishingly thin in the z dimension. The slot has a finite length L and a finite width W. A plane wave which is TM to the slot is incident on the sheet. The incident H-field is given by

$$\vec{H}_{inc} = \hat{x} |H_{inc}| \quad (1)$$

The boundary conditions which must be met at the slot/sheet interface is that the tangential E-field and the total H-field across the slot is continuous, and the tangential E-field on the sheet is zero. The tangential electric field in the slot excited by the plane wave can be replaced by equivalent magnetic current sources distributed over the slot area on both



sides of the conductor after closing the slot with a conductor. By applying image theory as shown in Figure 2, the field on the incident side of the sheet is reduced to the field produced by twice the magnetic current in free space, the incident field and its image<sup>[3,4]</sup>. Setting the total magnetic field at the slot on side 1 equal to that on side 2 an equation is obtained relating the incident field to the magnetic field produced by the magnetic current source M only.

$$H(M) = H_{inc} \quad (2)$$

The electric vector potential derived from the slot current is given by

$$\begin{aligned} \vec{F}^{\>} &= \frac{1}{4\pi} \iiint \vec{M}^{\>} \frac{e^{-jk|\vec{r}-\vec{r}'|}}{|\vec{r}-\vec{r}'|} d\vec{r}' ; \quad \vec{M}^{\>} = M\hat{x} \\ &= \frac{1}{4\pi} \int_{-\infty}^{\infty} \int_{-w/2}^{w/2} \int_{-L/2}^{L/2} M\hat{x} \frac{e^{-jk\sqrt{(x-x')^2 + (y-y')^2 + (z-z')^2}}}{\sqrt{(x-x')^2 + (y-y')^2 + (z-z')^2}} dx' dy' dz' \end{aligned} \quad (3)$$

and the electric and magnetic fields are given by

$$-j\omega\mu_0\vec{H}_S^{\>} = k_0^2 \vec{F}^{\>} + \vec{\nabla}^{\>} (\vec{\nabla}^{\>} \cdot \vec{F}^{\>}) \quad (4)$$

$$\vec{E}_s^> = \frac{1}{j\omega\epsilon_0} \vec{\nabla}^> \times \vec{H}^> = -\frac{1}{\epsilon_0} \vec{\nabla}^> \times \vec{F}^>$$

(5)

(see appendix A for definitions of variables)

The basis functions chosen for the method of moments solution are entire domain basis functions based upon a sum of cosine functions of integral multiples of  $x$  having support over the slot region. The testing functions are chosen to be the same as the basis functions according to Galerkin's method.

The equivalent magnetic current in the slot can be expressed as

$$\begin{aligned} \vec{M}^>(x', y', z') = & \hat{x} \sum_{n=1}^N a_n \cos\left(\frac{n\pi}{L}x'\right) \cdot [u(x'+L/2)-u(x'-L/2)] \\ & \cdot [u(y'+w/2)-u(y'-w/2)] \cdot \delta(z') \end{aligned} \quad (6)$$

which when substituted into the equation for the electric vector potential  $F$  yields

$$\vec{F}^> = \hat{x} \frac{1}{4\pi} \int_{-\infty}^{\infty} \int_{-w/2}^{w/2} \int_{-L/2}^{L/2} \sum_{n=1}^N a_n \cos\left(\frac{n\pi}{L}x'\right) \frac{e^{-jkR}}{R} \delta(z') dx' dy' dz' \quad (7)$$

where;  $R = \sqrt{(x-x')^2 + (y-y')^2 + (z-z')^2}$

then

$$-j\omega\mu_0\vec{H} = \hat{x} k_0^2 \frac{1}{4\pi} \int_{-\infty}^{\infty} \int_{-w/2}^{w/2} \int_{-L/2}^{L/2} \sum_{n=1}^N a_n \cos\left(\frac{n\pi}{L}x'\right) \frac{e^{-jkR}}{R} \delta(z') dx' dy' dz' \quad (8)$$

$$+ \hat{x} \frac{1}{4\pi} \int_{-\infty}^{\infty} \int_{-w/2}^{w/2} \int_{-L/2}^{L/2} \nabla^2 \left[ \sum_{n=1}^N a_n \cos\left(\frac{n\pi}{L}x'\right) \right] \frac{e^{-jkR}}{R} \delta(z') dx' dy' dz'$$

This equation can be rewritten as convolution integral in x

$$P(x) = \cos\left(\frac{n\pi x}{L}\right) \left[ u\left(x + \frac{L}{2}\right) - u\left(x - \frac{L}{2}\right) \right];$$

$$Q(x) = \frac{e^{-jkR}}{R}$$

then

$$-j\omega\mu_0\vec{H} = \frac{\hat{x}}{4\pi} \sum_{n=1}^N a_n k_0^2 \int_{-\infty}^{\infty} \int_{-w/2}^{w/2} P(x) \circledast Q(x) dy' \delta(z') dz' + \sum_{n=1}^N a_n \int_{-\infty}^{\infty} \int_{-w/2}^{w/2} \vec{\nabla}^2 (\vec{\nabla}^2 (P(x) \circledast Q(x))) dy' \delta(z') dz' \quad (9)$$

(where  $\circledast$  represents convolution)

Applying the distributive properties of the convolution integral with regard to differentiation, the Laplacian can operate on either P or Q prior to performing the convolution.

$$\nabla^2 (P(x) \otimes Q(x)) = P(x) \otimes (\nabla^2 Q(x)) = (\nabla^2 P(x)) \otimes Q(x)$$

Since the incident magnetic field has only an x component the Laplacian reduces to the second partial derivative on x.

$$\begin{aligned} \frac{d^2}{dx^2} P(x) &= -\left(\frac{n\pi}{L}\right)^2 \cos\left(\frac{n\pi}{L}x\right) \left[u\left(x + \frac{L}{2}\right) - u\left(x - \frac{L}{2}\right)\right] \\ &+ \frac{2n\pi}{L} \left[\sin\left(\frac{n\pi}{2}\right) \left[\delta\left(x + \frac{L}{2}\right) - \delta\left(x - \frac{L}{2}\right)\right]\right] \\ &+ \cos\left(\frac{n\pi}{2}\right) \left[\delta'\left(x + \frac{L}{2}\right) - \delta'\left(x - \frac{L}{2}\right)\right] \end{aligned} \quad (10)$$

which for n even reduces to;

$$\begin{aligned} &= -\left(\frac{n\pi}{L}\right)^2 \cos\left(\frac{n\pi}{L}\right) \left[u\left(x + \frac{L}{2}\right) - u\left(x - \frac{L}{2}\right)\right] \\ &+ \cos\left(\frac{n\pi}{2}\right) \left[\delta'\left(x + \frac{L}{2}\right) - \delta'\left(x - \frac{L}{2}\right)\right] \end{aligned} \quad (11)$$

and for n odd ;

$$\begin{aligned} \frac{d^2}{dx^2} P(X) = & -\left(\frac{n\pi}{L}\right)^2 \cos\left(\frac{n\pi}{L}x\right) \left[u\left(x + \frac{L}{2}\right) - u\left(x - \frac{L}{2}\right)\right] \\ & + \frac{2n\pi}{L} \sin\left(\frac{n\pi}{2}\right) \left[\delta\left(x + \frac{L}{2}\right) + \delta\left(x - \frac{L}{2}\right)\right] \end{aligned} \quad (12)$$

The choice of n even implies that an E-field maximum at  $x = \pm L/2$  which is inconsistent with the physical assumptions, therefore the choice of n odd is employed. Substituting (11) into (8) results in the following equation for the magnetic field in the x direction

$$\begin{aligned} -j\omega\mu_0 H_x = & \frac{1}{4\pi} \sum_{n=1}^N a_n \int_{-w/2}^{w/2} \int_{-L/2}^{L/2} \left(k^2 - \left(\frac{n\pi}{L}\right)^2\right) \cos\left(\frac{n\pi}{L}x'\right) \\ & \frac{e^{-jkR'}}{R} dx' dy' \\ & + \frac{1}{4} \sum_{n=1}^N a_n \int_{-w/2}^{w/2} \left(\frac{2n\pi}{L} - \frac{2L}{n\pi}\right) \sin\left(\frac{n\pi}{2}\right) \frac{e^{-jkR'}}{R} dy' \end{aligned} \quad (13)$$

where  $R'$  is  $R$  evaluated at  $z = 0$ ,

$$R' = \sqrt{(x-x')^2 + (y-y')^2}$$

and  $R''$  is  $R$  evaluated at  $z = 0$ ,  $x' = \pm L/2$

$$R'' = \sqrt{(x \pm L/2)^2 + (y - y')^2}$$

The choice of testing function is made according to Galerkin's method<sup>[5]</sup>. Hence an element of the set is given by

$$T_m(x) \Big|_{m \text{ odd}} = \cos\left(\frac{m\pi}{L}x\right) \left[u\left(x + \frac{L}{2}\right) - u\left(x - \frac{L}{2}\right)\right] \cdot \left[u\left(y + \frac{w}{2}\right) - u\left(y - \frac{w}{2}\right)\right] \quad (14)$$

When (2) is tested by (13) over the support of the slot a set of simultaneous linear equations result from which the unknown current coefficients  $a_n$  can be determined.

$$\begin{bmatrix} \langle T_1(x), H_1^S(x) \rangle & - & - & - & \langle T_1(x), H_N^S(x) \rangle \\ \vdots & & & & \vdots \\ \langle T_N(x), H_1^S(x) \rangle & - & - & - & \langle T_N(x), H_N^S(x) \rangle \end{bmatrix} \begin{bmatrix} a_1 \\ \vdots \\ a_N \end{bmatrix} = \quad (15)$$

$$\begin{bmatrix} \langle T_1(x), H_1^i(x) \rangle \\ \vdots \\ \langle T_N(x), H_N^i(x) \rangle \end{bmatrix}$$

an arbitrary inner product is evaluated as

$$\langle T_m(x), H_x^S \rangle =$$

$$\sum_{n=1}^N a_n \iint_{-L/2}^{L/2} \int_{-w/2}^{w/2} (k^2 - (\frac{n\pi}{L})^2) \cos(\frac{n\pi}{L}x') \cos(\frac{m\pi}{L}x)$$

$$\frac{e^{-jkR'}}{R'} dx' dy' dx$$

$$+ \int_{-L/2}^{L/2} \int_{-w/2}^{w/2} (\frac{2n\pi}{L} - \frac{2L}{n\pi}) \sin(\frac{n\pi}{2}) \cos(\frac{m\pi}{L}x) \frac{e^{-jkR'}}{R'} dy' dx$$

$$+ \int_{-L/2}^{L/2} \int_{-w/2}^{w/2} (\frac{2n\pi}{L} - \frac{2L}{n\pi}) \sin(\frac{n\pi}{2}) \cos(\frac{m\pi}{L}x) \frac{e^{-jkR'}}{R'} dy' dx \quad (16)$$

The above equations can be reduced and simplified by further application of convolution methods and manipulation of variables to yield

$$\langle T_m(x), H_x^S \rangle = \sum_{n=1}^N a_n \int_0^L \int_{-w/2}^{w/2} \left( \frac{4Lm}{(m^2 - n^2)\pi} \right)$$

$$[\sin(\frac{(m-n)\pi}{2L}(L-x')) \cos(\frac{(m+n)\pi}{L}x')]$$

$$+ \sin(\frac{(m+n)\pi}{2L}(L-x')) \cos(\frac{(m-n)\pi}{2L}x')] \cdot (k^2 - (\frac{n\pi}{L})^2)$$

$$\cdot \frac{e^{-jk\sqrt{x'^2 + y'^2}}}{\sqrt{x'^2 + y'^2}} dy' dx'$$

$$+ \int_{-L/2}^{L/2} \int_{-w/2}^{w/2} \left( \frac{2n\pi}{L} - \frac{2L}{n\pi} \right) \sin(\frac{n\pi}{2}) \cos(\frac{n\pi}{L}x)$$

$$\frac{e^{-jk\sqrt{(x+L/2)^2 + (y-y')^2}}}{\sqrt{(x+L/2)^2 + (y-y')^2}} dy' dx + \int_{-L/2}^{L/2} \int_{-w/2}^{w/2} \left( \frac{2n\pi}{L} - \frac{2L}{n\pi} \right) \sin(\frac{n\pi}{2})$$

$$\cos(\frac{m\pi}{L}x) \frac{e^{-jk\sqrt{(x-L/2)^2 + (y-y')^2}}}{\sqrt{(x-L/2)^2 + (y-y')^2}} dy' dx \quad (17)$$

and

$$\langle T_m(x), H_x^i \rangle = \int_{-L/2}^{L/2} \cos(\frac{m\pi}{L}x) e^{-jkx} \sin\theta_i \cos\phi_i dx$$

(18)



$$= \frac{[-2\cos(\gamma)\frac{m\pi}{L}\sin(\frac{m\pi}{2}) + 2k_o\sin(\gamma)\sin\theta_i\cos\phi_i\cos(\frac{m\pi}{2})]}{(k_o^2\sin^2\theta_i\cos^2\phi_i) - (\frac{m\pi}{L})^2}$$

$$\text{where } \gamma = -\frac{kL}{2} \sin\theta_i\cos\phi_i$$

#### 4. Computations

The solution of the matrix equation was performed using numerical integration and matrix inversion for  $N = 1, 3, 5, 7$ , and  $9$ . The far electric field was computed for each "mode" and the sum of these first five odd modes. The results are plotted for  $\phi = 0^\circ$  and  $90^\circ$  as a function of the far field angle  $\theta$  in Figures 3 through 12 for each of the modes and Figures 13 and 14 for the sum of the five modes. The plots of Figures 15 and 16 are for  $\phi = 0^\circ$  and  $90^\circ$  as a function of the angle of incidence of the plane wave excitation. It is significant to note the following; the computed far field for the sum of the first five odd modes and that for the first mode  $N = 1$  are almost identical, the relative amplitude of the higher order mode fields are at least 9 Db or more below the first order mode field, and the form of the scattered far field is the same as would be expected from a

rectangular aperture. It is also of note that for a narrow slot ( $w \ll \lambda$ ) there can be no transverse electric wave.

## 5. Conclusions and Future Application

The method yields the scattered field from a transverse magnetic wave incident on finite length and width slot in an infinite ground plane even for a relatively small number of terms but the computations must be validated by comparison to measured data. The future application of this formulation will involve the solution for a transverse electric incident wave, superposition of the TM and TE solutions and the extension to a solution for a pair of orthogonal slots.

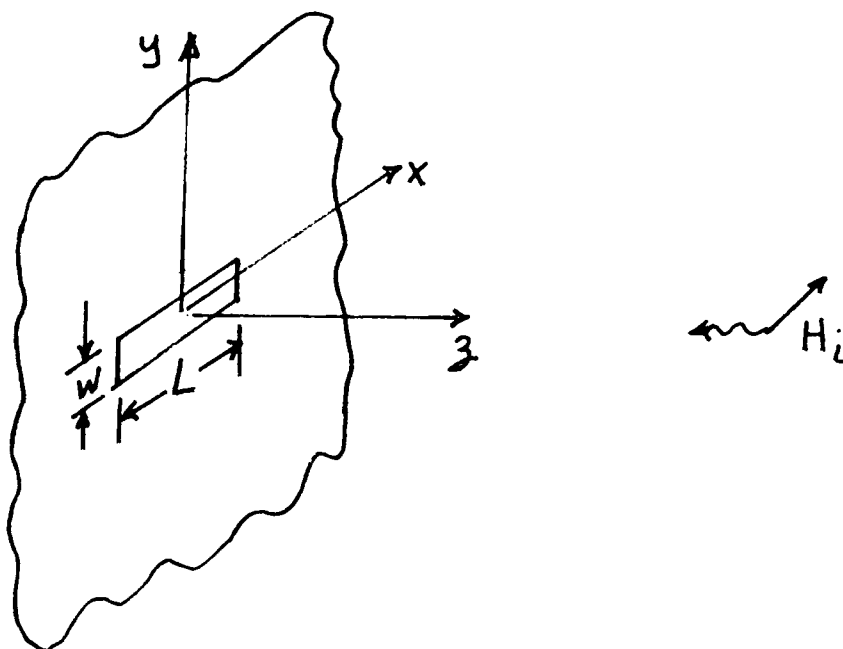


Figure 1.

$$\begin{array}{c}
 \epsilon_0, M_0 \\
 \left| \begin{array}{c} H_s^2 \\ \hat{H}_s^1 \\ H_i \end{array} \right\rangle \left| \begin{array}{c} H_s^1 \\ \hat{H}_s^2 \\ H_i \end{array} \right\rangle \left| \begin{array}{c} H_i \\ \hat{H}_s^1 \\ \hat{H}_s^2 \end{array} \right\rangle \\
 \left| \begin{array}{c} H_s^2 \\ \hat{H}_s^1 \\ H_i \end{array} \right\rangle \left| \begin{array}{c} H_s^1 \\ \hat{H}_s^2 \\ H_i \end{array} \right\rangle \left| \begin{array}{c} H_i \\ \hat{H}_s^1 \\ \hat{H}_s^2 \end{array} \right\rangle
 \end{array}
 \Rightarrow
 \begin{array}{c}
 \epsilon_0, M_0 \\
 \left| \begin{array}{c} H_s^2 \\ \hat{H}_s^1 \\ H_i \end{array} \right\rangle \left| \begin{array}{c} H_s^1 \\ \hat{H}_s^2 \\ H_i \end{array} \right\rangle \left| \begin{array}{c} H_i \\ \hat{H}_s^1 \\ \hat{H}_s^2 \end{array} \right\rangle \\
 \left| \begin{array}{c} H_s^2 \\ \hat{H}_s^1 \\ H_i \end{array} \right\rangle \left| \begin{array}{c} H_s^1 \\ \hat{H}_s^2 \\ H_i \end{array} \right\rangle \left| \begin{array}{c} H_i \\ \hat{H}_s^1 \\ \hat{H}_s^2 \end{array} \right\rangle
 \end{array}
 \Rightarrow
 \begin{array}{c}
 \hat{H}_s^1 \hat{H}_s^2 \\
 \left| \begin{array}{c} H_s^2 \\ \hat{H}_s^1 \\ H_i \end{array} \right\rangle \left| \begin{array}{c} H_s^1 \\ \hat{H}_s^2 \\ H_i \end{array} \right\rangle \left| \begin{array}{c} H_i \\ \hat{H}_s^1 \\ \hat{H}_s^2 \end{array} \right\rangle \\
 \left| \begin{array}{c} H_s^2 \\ \hat{H}_s^1 \\ H_i \end{array} \right\rangle \left| \begin{array}{c} H_s^1 \\ \hat{H}_s^2 \\ H_i \end{array} \right\rangle \left| \begin{array}{c} H_i \\ \hat{H}_s^1 \\ \hat{H}_s^2 \end{array} \right\rangle
 \end{array}$$

$$H_{total} = H_i + (H_s^1 - H_s^2)$$

Figure 2.

PHI - 0.0  
MODE NUMBER - 1

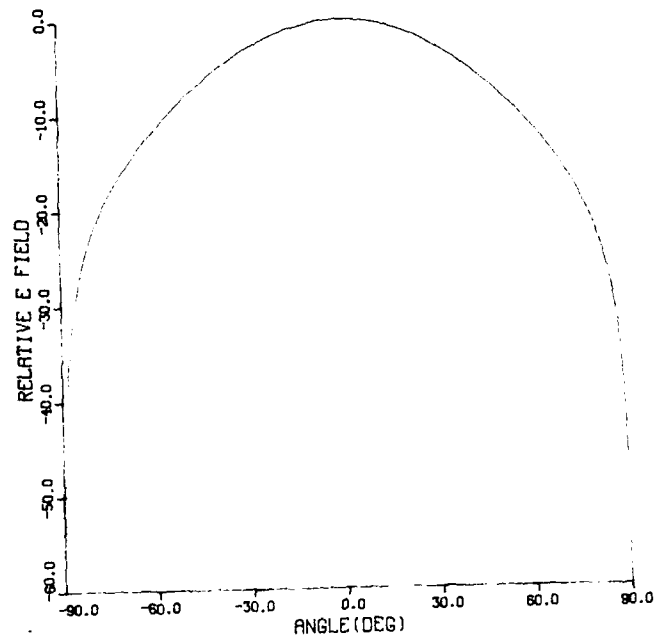


Figure 3.

PHI - 90.0  
MODE NUMBER - 1

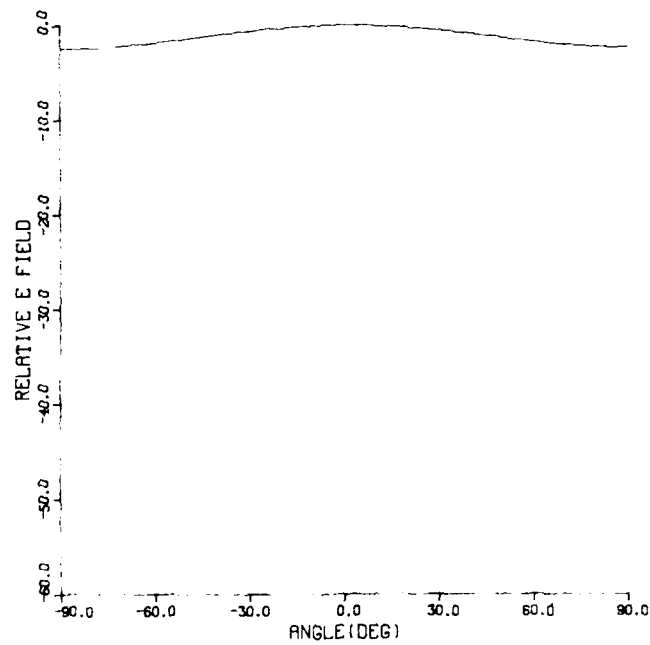


Figure 4.

PHI - 0.0

MODE NUMBER - 3

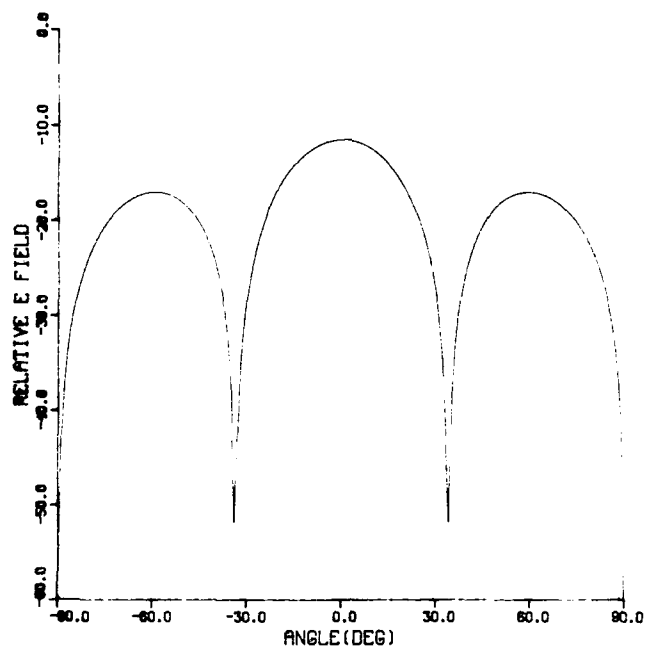


Figure 5.

PHI - 90.0

MODE NUMBER - 3

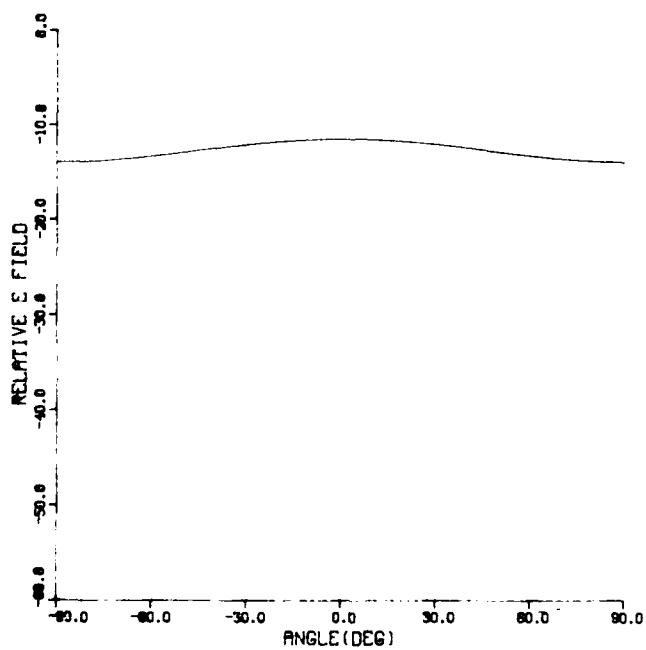


Figure 6.

PHI - 0.0  
MODE NUMBER - 5

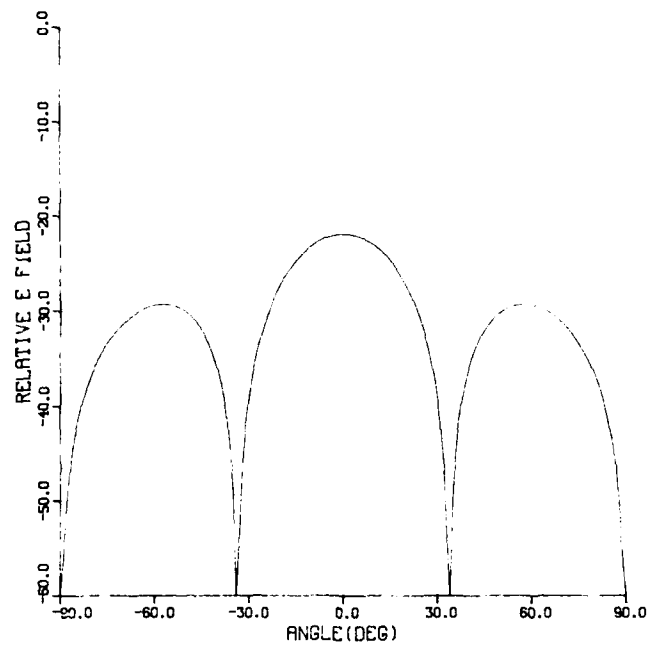


Figure 7

PHI - 90.0  
MODE NUMBER - 5

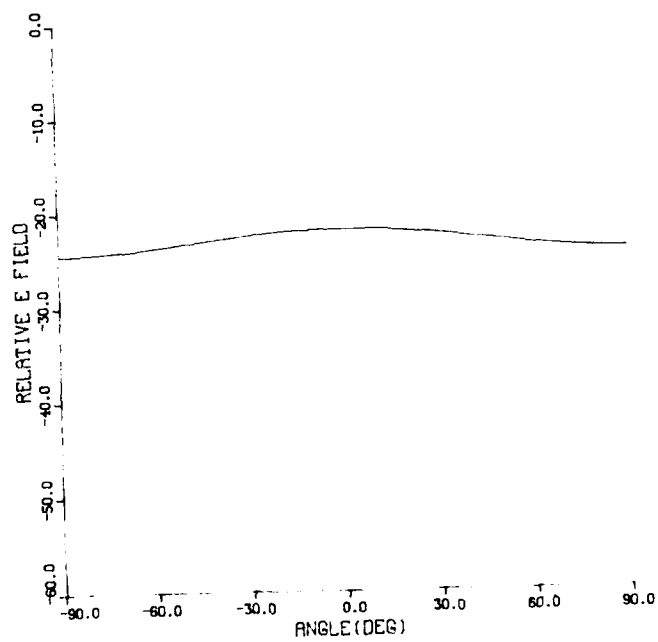


Figure 8

PHI - 0.0

MODE NUMBER - 7

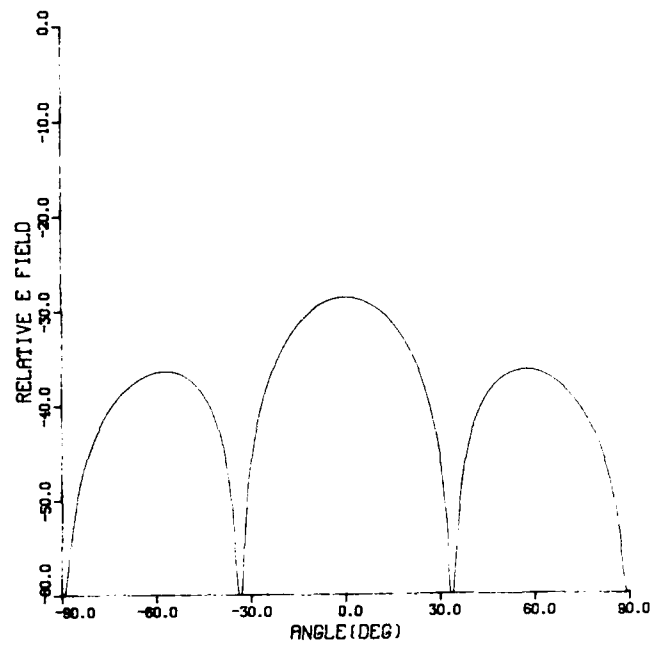


Figure 9.

PHI - 90.0

MODE NUMBER - 7

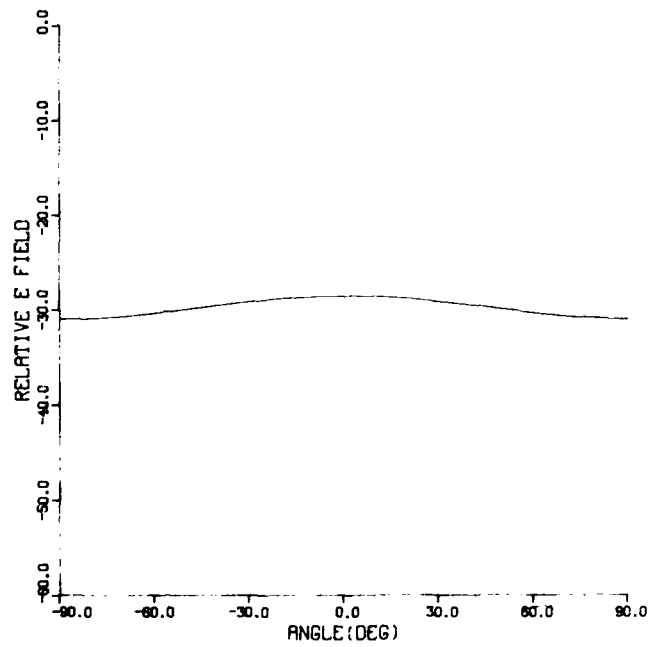


Figure 10.

PHI - 0.0

MODE NUMBER - 9

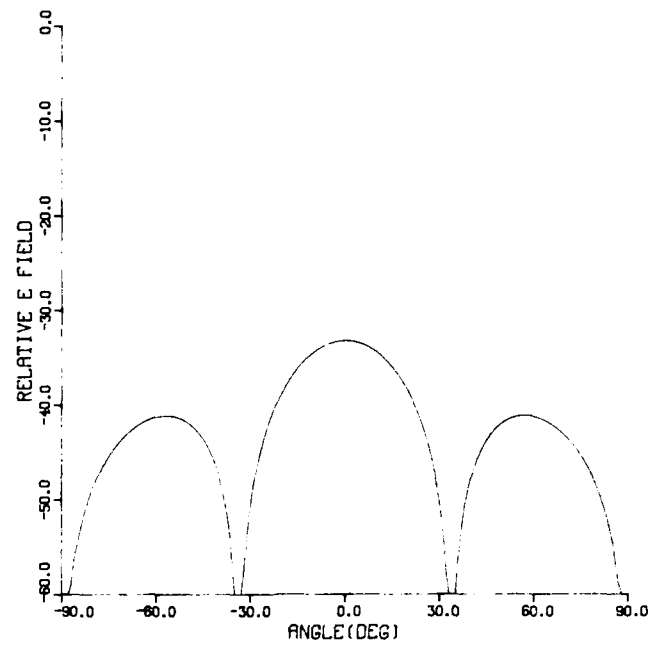


FIGURE 11.

PHI - 90.0

MODE NUMBER - 9

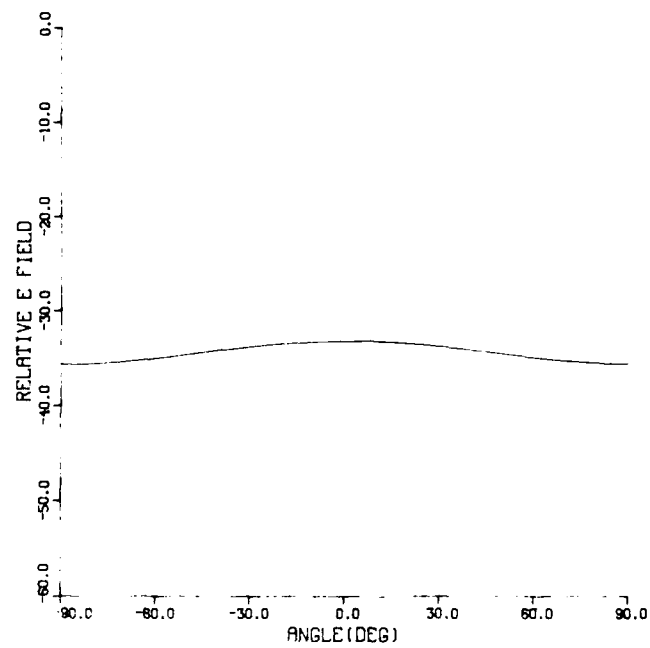


FIGURE 12.



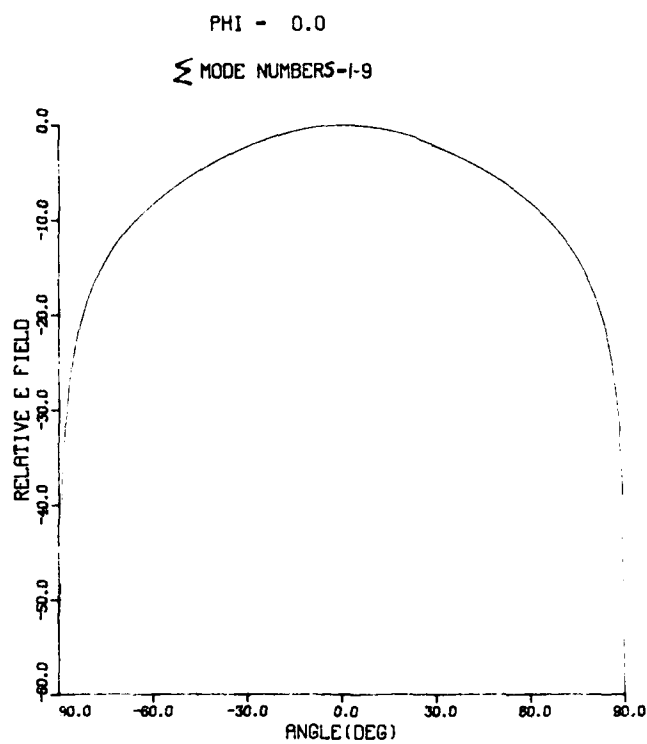


FIGURE 13

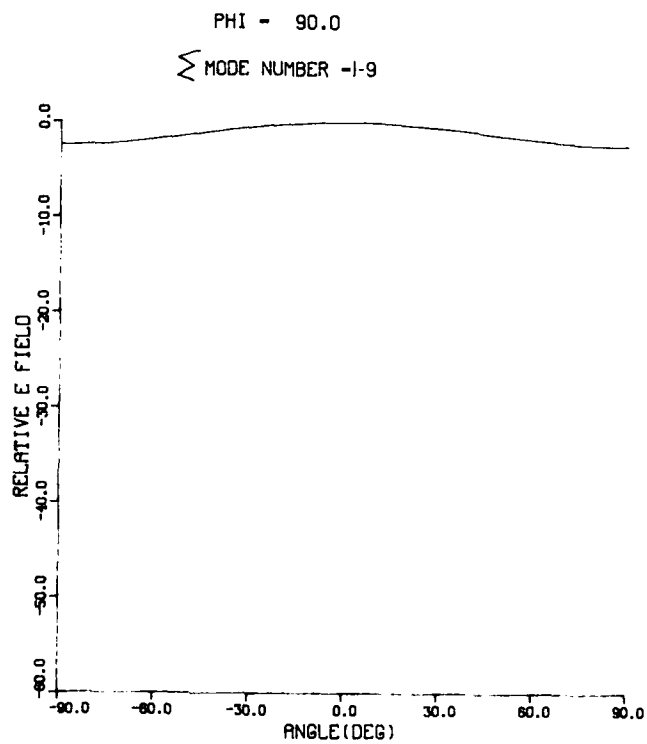


FIGURE 14

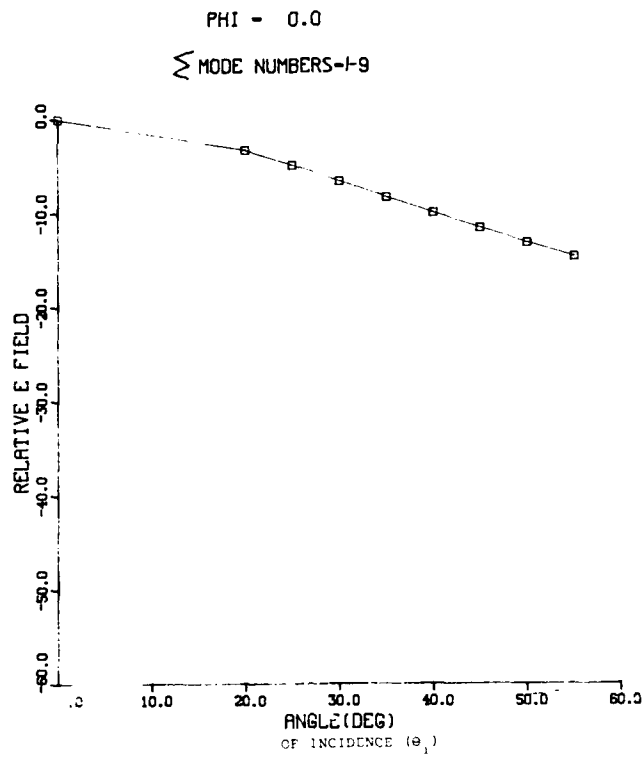


FIGURE 15.

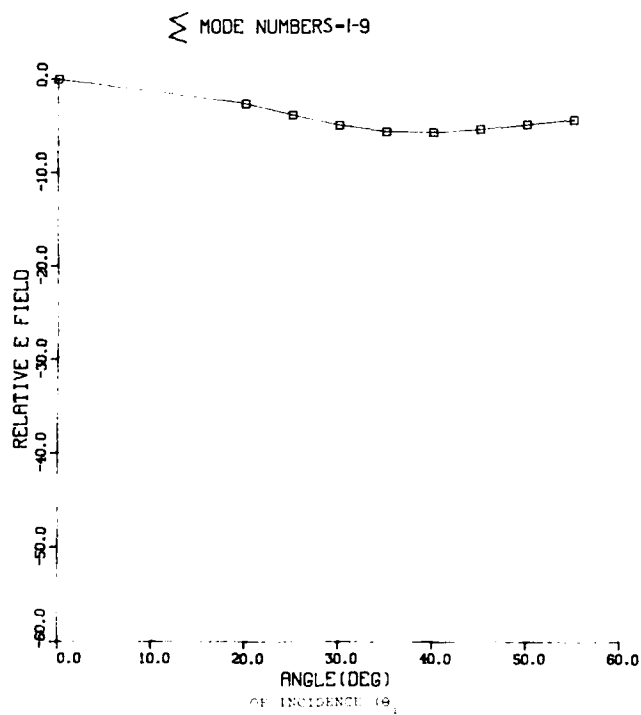


FIGURE 16.

## REFERENCES

1. Elliot, R. S. (1983) An improved design procedure for small arrays of shunt slots, IEEE Trans. AP-S 31 (No. 1) 48-53.
2. Malherbe, J. A. G., and Davidson, D. B. (1984) Mutual impedance for half-cosinusoid slot voltage distribution an evaluation, IEEE Trans. AP-S 32 (No. 9) 990-991.
3. Butler, C. M., et al., (1978) Electromagnetic penetration through apertures in conducting surfaces, IEEE Trans. AP-S 26 (No. 1) 82-93.
4. Harrington, R. F. (1961) Time Harmonic Electromagnetic Fields, McGraw-Hill, New York, pp. 103-110.
5. Harrington, R. F. (1968) Field Computation by Moment Methods, Robert E. Krieger, Malabar, FL.

## APPENDIX A

### Variable Definitions

$a_n$      $n$  th coefficient of the basis function sum  
          from 1 to  $N$

$\vec{F}$     electric vector potential

$\vec{H}, \vec{E}$     magnetic and electric field vectors

$k$     wave number  $\frac{2\pi}{\lambda}$

$L$     slot length

$\vec{M}$     magnetic current vector

$n$     summation index

$P(x), Q(x-x')$  functions of  $x, x-x'$

$R, r$     radius

$T(x)$     testing function

$w$     width of slot

theta    incident polar angle

phi    incident polar angle

inc, i    subscript for incident quantity

scat, s    subscript for scattered quantity

$u[x' - \frac{L}{2}]$     unit step function 1 for  $x' \geq \frac{L}{2}$   
                  0 elsewhere

$\delta(z')$     impulse function    1 when  $z' = 0$  , 0 elsewhere

## NEAR-FIELD BISTATIC RCS MEASUREMENT AT BDM

R. Rogers and E. Farr  
The BDM Corporation  
1801 Randolph Road SE  
Albuquerque, NM 87106

### ABSTRACT

The techniques of near-field antenna pattern measurement can be extended to near-field RCS measurement. The motivation for doing so is precisely the same as that for near-field antenna measurements; i.e., the convenience of an indoor antenna range, and an improvement in accuracy. Although the near-field measurement problem is solvable in principle in a manner analogous to the near-field antenna problem, it requires a significantly larger amount of time to take the necessary data, and to subsequently process the data to obtain useful quantities.

BDM is currently involved in an on-going program to evaluate the feasibility of near-field bistatic RCS measurements. At the time of this writing, a complete set of mathematics has been formulated to handle the probe correction and data processing. The hardware has been built, software development is near completion, and the analysis of canonical scattering objects has been completed. Experimental data soon to be taken for these objects will be presented. It is hoped that the technique will

prove to be a practical approach to RCS measurements.

## 1.0 INTRODUCTION

In this paper we discuss an on-going project to evaluate a plane-wave scattering matrix (PWSM) approach to measuring bistatic radar cross-section (BRCS). Arrays of measurements obtained with separate transmit and receive probe antennas are computer processed to yield the complex bistatic scattering matrix as a function of illumination and observation angles. The data acquisition and computer processing are an exact sampled data implementation of the continuous-domain PWSM theory, provided that attention is paid to bandlimiting and sampling constraints.

A particularly appealing aspect of this approach to BRCS is that bistatic measurements can be made at angles very close to the monostatic. A significant drawback is the large number of measurements that must be made.

We will discuss in turn the continuous-domain PWSM theory of BRCS, the sampled-data formulation of that theory, and the experimental work in progress.

## 2.0 PLANE-WAVE SCATTERING MATRIX BRCS THEORY

This work is based upon a three-antenna plane-wave scattering matrix theory derived by Dinallo<sup>1</sup>. The goal is to calculate for an arbitrary object a (mono-frequency) scattering matrix

$$\underline{I}_{11}(\bar{k}, \bar{l}) = \begin{bmatrix} I_{11\theta\theta}(\bar{k}, \bar{l}) & I_{11\theta\phi}(\bar{k}, \bar{l}) \\ I_{11\phi\theta}(\bar{k}, \bar{l}) & I_{11\phi\phi}(\bar{k}, \bar{l}) \end{bmatrix} \quad (1)$$

which describes the scattering of a unit incident plane wave by an object. Incident and scattered propagation vectors are

$$\bar{l} = l_x \hat{e}_x + l_y \hat{e}_y + l_z \hat{e}_z \quad (2a)$$

$$\bar{k} = k_x \hat{e}_x + k_y \hat{e}_y + k_z \hat{e}_z. \quad (2b)$$

The elements of the scattering matrix  $\underline{I}_{11}(\bar{k}, \bar{l})$  are specified by means of two polarization-related indices and two propagation vectors. For example,  $I_{11\theta\phi}(\bar{k}, \bar{l})$  refers to the  $\theta$ -component of the angular spectrum of the wave that is scattered when the object is illuminated by the  $\phi$ -component of the angular spectrum of the incident wave. Taking all four elements together,  $\underline{I}_{11}(\bar{k}, \bar{l})$  specifies how the  $\theta$  and  $\phi$  components of the angular spectrum of the incident wave  $\bar{l}$  are scattered into  $\theta$  and  $\phi$  components of the angular spectrum of a scattered wave  $\bar{k}$ .

The scattering of an arbitrary wavefront by the object follows directly, since the superposition principle allows us to create complex wavefronts as a superposition of plane waves.

### 3.0 CALCULATING SCATTERING MATRIX

In order to calculate the scattering matrix, we will first calculate the  $\theta$ - and  $\phi$ -components of the scattered angular spectrum over the area scanned by the receive probe, given

illumination of the test object by the transmit probe in a particular orientation and location. This process is repeated for a set of transmit probe locations.

The transmit probe is then rotated to illuminate the test object with a different angular spectrum, and we repeat the measurements and calculations to determine the  $\theta$ - and  $\phi$ -components of the scattered angular spectrum for this second transmit probe antenna orientation and set of locations.

The laboratory measurements for bistatic near-field scattering consist of gain and phase measurements made by a receive probe as it is swept through a pattern of probe locations. The receive probe scan pattern is swept repeatedly (and gain and phase measurements made) for a set of transmit probe locations, as the transmit probe itself steps through a set of locations in the transmit probe scan pattern.

The transmit probe and receive probe we use are identical, although they need not be so. The receive probe's receiving characteristic

$$\bar{I}_{01}(\bar{k}) = \begin{bmatrix} I_{01\theta}(\bar{k}) \\ I_{01\phi}(\bar{k}) \end{bmatrix} \quad (3)$$

and the transmit probe's transmitting characteristic



$$\bar{I}_{10}(\bar{I}) = \begin{bmatrix} I_{10\theta}(\bar{I}) \\ I_{10\phi}(\bar{I}) \end{bmatrix} \quad (4)$$

are assumed to be known (either analytically or empirically<sup>2</sup>). As in the case of near-field antenna measurements, neither probe antenna should have nulls in a direction for which one wishes to calculate the scattering matrix.

The transmit characteristic is related to the antenna's far-field  $\bar{E}(\bar{r})$  as<sup>3</sup>

$$\bar{I}_{10}(\bar{k}) = \frac{1}{2\pi k^2 \cos\theta} \lim_{r \rightarrow \infty} \left\{ kr \cdot e^{-jkr} \bar{E}(\bar{r}) \right\}. \quad (5)$$

For a reciprocal antenna, the transmit and receive characteristics are related by

$$\bar{I}_{01}(\bar{k}) = \frac{Y_0 \cos\theta}{\eta_0} \bar{I}_{10}(-\bar{k}) \quad (6)$$

where  $Y_0$  is the characteristic admittance of the waveguide feed, and  $\eta_0$  is the characteristic admittance of free space.

The scattering object is at the origin of a coordinate system S (Figure 1). We define  $\bar{I}$  as the propagation vector of the incident plane wave (from the transmit probe),  $\bar{r}_1$  as the coordinates of the transmit probe,  $\bar{k}$  as the propagation vector of the scattered plane wave (to the receive probe), and  $\bar{r}_2$  as the coordinates of the receive probe.

The measurement equation for near-field bistatic RCS is

$$b_o(\bar{r}_1, \bar{r}_2) = \underbrace{\iint \bar{I}_{\theta 1}(\bar{k})}_{(1)} \cdot \underbrace{\left[ \iint \bar{I}_{11}(\bar{k}, \bar{l}) \cdot \bar{I}_{1\theta}(\bar{l}) e^{-i\bar{l} \cdot \bar{r}_1} d\bar{l} \right]}_{(2) \quad (3) \quad (4)} \underbrace{e^{+i\bar{k} \cdot \bar{r}_2}}_{(5)} d\bar{k}, \quad (7)$$

where

$$\bar{K} = k_x \hat{e}_x + k_y \hat{e}_y \quad (8a)$$

$$\bar{l} = l_x \hat{e}_x + l_y \hat{e}_y. \quad (8b)$$

The scalar  $b_o$  is a measurable quantity that is the complex gain factor describing the transmission path from the transmit probe to the receive probe via the scattering object. The incident wave is represented by the factor {3}. The exponential {4} represents propagation of the incident wave from the transmitting antenna to the object, and the multiplication with {2} represents scattering by the object. The resulting scattered spectrum of waves propagates {5} from the object to the receive probe; {1} represents the interaction of the propagated, scattered wave with the receiving probe itself. Note that multiple interactions are not included in the measurement equation.

If we consider the scattering object as a transmitting antenna, the complicated wavefront generated by it can be represented by a superposition of plane waves. We denote that superposition by  $\bar{F}_1(\bar{r}_1, \bar{k})$ , where  $\bar{r}_1$  is the location of the actual transmit source, and  $\bar{k}$  is the propagation vector of the scattered plane waves.

Since the scattered spectrum is

$$\bar{F}_1(\bar{r}_1, \bar{k}) = \iint \bar{I}_{11}(\bar{k}, \bar{l}) \cdot \bar{I}_{10}(\bar{l}) e^{-i\bar{l} \cdot \bar{r}_1} d\bar{l}, \quad (9)$$

the measurement equation above becomes

$$b_o(\bar{r}_1, \bar{r}_2) = \iint \bar{I}_{01}(\bar{k}) \cdot \bar{F}_1(\bar{r}_1, \bar{k}) e^{+i\bar{k} \cdot \bar{r}_2} d\bar{k}. \quad (10)$$

This is the measurement equation for near-field antenna measurement. The usual manipulations<sup>4</sup> (i.e., two sets of measurements with different  $\bar{I}_{01}(\bar{k})$ , Fourier transform, and simultaneous equation solution) are employed to determine  $\bar{F}_1(\bar{r}_1, \bar{k})$ .

Furthermore, the above two equations are similar in form, except that  $b_o(\bar{r}_1, \bar{r}_2)$  is a scalar while  $\bar{F}_1(\bar{r}_1, \bar{k})$  is a vector. The solution techniques of near-field antenna measurement can be applied to solving for  $\bar{F}_1(\bar{r}_1, \bar{k})$ , except that two independent solutions, representing the  $\hat{e}_\theta$  and  $\hat{e}_\phi$  components of  $\bar{F}_1(\bar{r}_1, \bar{k})$ , must be found.

In order to calculate the scattering matrix it is necessary to determine a second, independent scattered spectrum  $\bar{F}_2(\bar{r}_1, \bar{k})$  that represents the scattered spectrum with the object illuminated by a different source spectrum. For example, with linearly-polarized transmit probe, rotating the transmit probe by  $\pi/2$  creates a different source spectrum. So, with the transmit

probe antenna rotated  $\pi/2$ , we repeat the entire series of measurements and calculations. For each transmit probe location  $\bar{r}_1$  we measure an array of scalar values as the receive probe is moved through its scan pattern. A second array of scalar values is measured with the receive probe in another orientation. These two arrays of measured data, called  $b_{03}(\bar{r}_1, \bar{r}_2)$  and  $b_{04}(\bar{r}_1, \bar{r}_2)$ , are used to calculate  $\bar{F}_2(\bar{r}_1, \bar{k})$ .

Referring to the general bistatic measurement equation (7), we have calculated  $\bar{F}_1(\bar{r}_1, \bar{k})$  and  $\bar{F}_2(\bar{r}_1, \bar{k})$ , where

$$\bar{F}_1(\bar{r}_1, \bar{k}) = \iint I_{11}(\bar{k}, \bar{l}) \cdot \bar{l}_{10}(\bar{l}) e^{-j\bar{l} \cdot \bar{r}_1} d\bar{l} \quad (11a)$$

and

$$\bar{F}_2(\bar{r}_1, \bar{k}) = \iint I_{11}(\bar{k}, \bar{l}) \cdot \bar{l}'_{10}(\bar{l}) e^{-j\bar{l} \cdot \bar{r}_1} d\bar{l} \quad (11b)$$

are Fourier integrals that may be inverted to give:

$$I_{11}(\bar{k}, \bar{l}) \cdot \bar{l}_{10}(\bar{l}) = \frac{1}{4\pi^2} \iint \bar{F}_1(\bar{r}_1, \bar{l}) e^{+j\bar{l} \cdot \bar{r}_1} d\bar{r}_1 \quad (12a)$$

$$I_{11}(\bar{k}, \bar{l}) \cdot \bar{l}'_{10}(\bar{l}) = \frac{1}{4\pi^2} \iint \bar{F}_2(\bar{r}_1, \bar{l}) e^{+j\bar{l} \cdot \bar{r}_1} d\bar{r}_1 \quad (12b)$$

This time the integrals are over all positions of the transmit probe, holding the receive probe position fixed. Since the transmit probe moves in the plane  $z = d$ , let

$$\bar{R}_1 = r_{1x} \hat{e}_x + r_{1y} \hat{e}_y + d \cdot \hat{e}_z, \quad (13)$$

and the integrals become

$$I_{11}(\bar{k}, \bar{l}) \cdot \bar{l}_{10}(\bar{l}) = \frac{e^{+cl_z}}{4\pi^2} \iint \bar{F}_1(\bar{r}_1, \bar{l}) e^{+cl \cdot \bar{R}_1} d\bar{R}_1 \quad (14a)$$

$$I_{11}(\bar{k}, \bar{l}) \cdot \bar{l}'_{10}(\bar{l}) = \frac{e^{+cl_z}}{4\pi^2} \iint \bar{F}_2(\bar{r}_1, \bar{l}) e^{+cl \cdot \bar{R}_1} d\bar{R}_1. \quad (14b)$$

We define a pair of vector coupling products  $\bar{Q}(\bar{k}, \bar{l})$  and  $\bar{Q}'(\bar{k}, \bar{l})$  as

$$\bar{Q}(\bar{k}, \bar{l}) = \frac{e^{+cl_z}}{4\pi^2} \iint \bar{F}_1(\bar{r}_1, \bar{l}) e^{+cl \cdot \bar{R}_1} d\bar{R}_1 \quad (15a)$$

$$\bar{Q}'(\bar{k}, \bar{l}) = \frac{e^{+cl_z}}{4\pi^2} \iint \bar{F}_2(\bar{r}_1, \bar{l}) e^{+cl \cdot \bar{R}_1} d\bar{R}_1, \quad (15b)$$

so that we can write

$$I_{11}(\bar{k}, \bar{l}) \cdot \bar{l}_{10}(\bar{l}) = \bar{Q}(\bar{k}, \bar{l}) \quad (16a)$$

$$I_{11}(\bar{k}, \bar{l}) \cdot \bar{l}'_{10}(\bar{l}) = \bar{Q}'(\bar{k}, \bar{l}). \quad (16b)$$

Expanding the above equation in components, and dropping the explicit  $(\bar{k}, \bar{l})$  dependence,

$$\begin{bmatrix} I_{100} & I_{10\phi} & 0 & 0 \\ 0 & 0 & I_{10\theta} & I_{10\phi} \\ I'_{100} & I'_{10\phi} & 0 & 0 \\ 0 & 0 & I'_{10\theta} & I'_{10\phi} \end{bmatrix} \cdot \begin{bmatrix} I_{1100} \\ I_{110\phi} \\ I_{11\phi\theta} \\ I_{11\phi\phi} \end{bmatrix} = \begin{bmatrix} Q_\theta \\ Q_\phi \\ Q'_\theta \\ Q'_\phi \end{bmatrix} \quad (17)$$

which has solutions:

$$I_{1100} = \frac{Q_\theta I'_{10\phi} - Q'_\theta I_{10\phi}}{\Delta} \quad (18a)$$

$$I_{110\phi} = \frac{Q_\phi I'_{10\phi} - Q'_\phi I_{10\phi}}{\Delta} \quad (18b)$$

$$I_{11\phi\theta} = \frac{Q_\theta I'_{10\phi} - Q'_\theta I_{10\phi}}{\Delta} \quad (18c)$$

$$I_{11\phi\phi} = \frac{Q_{\theta} I'_{10\phi} - Q'_{\theta} I_{10\phi}}{\Delta} \quad (18d)$$

provided the determinant

$$\Delta \equiv I_{10\theta} I'_{10\phi} - I'_{10\theta} I_{10\phi} \quad (19)$$

is nonzero for particular  $(\bar{k}, \bar{l})$ . This completes the calculation of the scattering matrix.

#### 4.0 ANGULAR FILTERING

Since the probe antennas may have very broad patterns, probe-to-probe coupling is an area of particular concern in this technique of BRCS measurement. However, the transmit probe is in the plane of the receive probe, so the plane wave spectrum illuminating the receive probe contains primarily waves with  $k_z \cong 0$ . These plane waves appear on the periphery of the Fourier transform in  $k_x$ - $k_y$  space and can be suppressed, provided that the probe-to-probe coupling has not swamped the desired scattered signal due to limited receiver dynamic range.

In Figure 2 we show a typical measured angular spectrum. The scattering object was a 6-inch diameter sphere illuminated at 10 GHz by a stationary transmit probe. The  $k_x$ - $k_y$  plane shown covers the entire backscattering hemisphere, but the angles of valid reconstruction encompass only the large double peaks, which are one component of the plane wave spectrum scattered from the sphere. The broad lower peak behind the double peaks comes from

probe coupling, while the smaller peaks around the periphery are due to room reflections. Note that the probe coupling peak has wrapped around into the positive- $k_y$  area of the calculated spectrum.

#### 5.0 DISCRETIZATION ISSUES

As in the case of near-field antenna measurement, it can be shown<sup>5</sup> that  $\bar{I}(\bar{k})$  in the x-y plane is effectively bandlimited, so that a sampled-data approach to measuring  $\bar{I}(\bar{k})$  in the plane  $z = d$  (a constant) is sufficient for reconstructing  $\bar{I}(\bar{k})$ . If the plane of measurement is not in the reactive near-field of any source antennas (i.e., several wavelengths or more from the antennas), sampling  $\bar{I}(\bar{k})$  at intervals slightly smaller than  $\lambda/2$  ensures that evanescent waves are attenuated sufficiently so that the spatial Nyquist requirement is met. Finally, spatial filtering and aliasing theory (and experiment) indicate that sampling at intervals larger than  $\lambda/2$  may be acceptable in certain situations.

Evaluation of integrals of the form

$$H(k_x) = \int_{-\infty}^{\infty} h(x) e^{ik_x x} dx \quad (20)$$

is feasible for bandlimited  $h(x)$  using sampled data and discrete Fourier transform techniques. The continuous function  $h(x)$  is sampled at intervals of  $\delta x$ , where  $\delta x$  is chosen sufficiently small to ensure that the spectrum of  $h(x)$ , convolved with the sampling

window, is unaliased for the  $k_x$  of interest. The sampled  $h(x)$  is a finite sequence

$$\begin{aligned} h'(n) &= \{h(x) \mid x = x_0 + (n-1) \cdot \delta x, n=1, \dots, N\} \\ &\equiv h'(1), h'(2), \dots, h'(N) \end{aligned} \quad (21)$$

which is implicitly periodic in  $n$  with period  $N$ . The DFT of  $h'(n)$  is

$$H'(m) = \sum_{n=1}^N h'(n) e^{\frac{-2\pi i (n-1)(m-1)}{N}}, \quad m = 1, \dots, N \quad (22)$$

where (for even  $N$ )

$$\delta k_x \equiv \frac{2\pi}{N\delta x} \quad (23)$$

$$k_x = \begin{cases} (m-1)\delta k_x & m = 1, 2, \dots, \frac{N}{2}+1 \\ [m-(N+1)]\delta k_x & m = \frac{N}{2}+2, \frac{N}{2}+3, \dots, N \end{cases} \quad (24)$$

$$H(k_x) = \delta x \cdot H'(m). \quad (25)$$

Due to the discrete implementation, laboratory measurements and data analysis yield a set of scattering matrices

$$I_{11}(\bar{K}_i, \bar{L}_j) = \begin{bmatrix} I_{11xx}(\bar{K}_i, \bar{L}_j) & I_{11xy}(\bar{K}_i, \bar{L}_j) \\ I_{11yx}(\bar{K}_i, \bar{L}_j) & I_{11yy}(\bar{K}_i, \bar{L}_j) \end{bmatrix} \quad (26)$$

where  $\bar{K}_i$  and  $\bar{L}_j$  can take on only a discrete set of values that are determined by the measurement grid size, the spatial sampling interval  $\delta x$ , and the "rules" of the DFT. Fourier interpolation can be used to increase the resolution of the grid of values of  $\bar{K}$  and  $\bar{L}$ .



Particular values of  $k_x$  and  $k_y$  represent plane wave with scattered angles

$$\theta = \cos^{-1}(k_z/k) \quad (27)$$

$$\phi = \tan^{-1}(k_y/k_x) \quad (28)$$

where

$$k_z = \pm \sqrt{k^2 - (k_x^2 + k_y^2)} \quad (29)$$

However, the reconstruction is valid only for some limited range of  $\theta$  and  $\phi$  determined by the sampling geometry (Figure 3). If the Fast Fourier Transform (FFT) is used to evaluate the DFT,  $k_x$  and  $k_y$  range from  $-\frac{\pi}{\delta}$  to  $+\frac{\pi}{\delta}$  (assuming  $\delta_x = \delta_y \equiv \delta$ ). It turns out that almost all of the transform values calculated by the FFT correspond to invalid  $\theta, \phi$ , while the FFT's sampling density in the range of valid  $\theta, \phi$  is very sparse. Thus it is practical to directly evaluate the series for arbitrary specified  $k_x$  and  $k_y$ . A similar argument applies to  $l_x$  and  $l_y$ .

## 6.0 APPARATUS

The scan table has two movable carriages, each with one movable platform. The carriages and platforms ride on stainless steel rails with recirculating ball-bearings, and are driven by Slo-Syn stepper motors via steel-and-plastic chains. Step size is 0.01175 inch, and positioning repeatability is typically 0.005 inch. The table is equipped with safety limit switches and

infrared indexing sensors. The object under test (OUT) is supported on a test fixture above the scanning table, and the transmit and receive probe antennas are mounted on the platforms. Absorber material is suspended above the OUT.

The probe antennas are identical equal-length open-ended sections of X-band waveguide. Each probe is held in a mounting bracket that is bolted to a single mounting hole on its platform.

The probe antennas move through predetermined scan patterns when measurements are being made. The scan patterns are (at the moment) non-overlapping squares. During "on-the-fly" scanning the receive probe moves along the x-axis while holding y constant. The x- and y-sampling intervals for both the receive and transmit probes are identical (after spatial filtering and resampling).

The equipment configuration for performing near-field measurements is shown in Figure 4. The synthesized RF signal is taken from the output port of the Hewlett-Packard 8408B Microwave Network Analyzer to a 20-watt TWT amplifier, and then to the transmit probe antenna via semi-rigid coaxial cable. Semi-rigid coax also carries the received signal from the receive probe to a preamplifier and then to the input port of the 8408B.

Measurements are obtained "on the fly" as the receive probe scans at 30 cm/sec. The gain and phase values are captured by dual sample/hold amplifiers with a 6  $\mu$ sec window for digitization

by a 12-bit/D converter. The network analyzer bandwidth is  $f_{bw} = 10 \text{ KHz}$ ; assuming an effective integration time of about  $3/f_{bw}$ , the data "smear" length is about 0.1 mm.

Measured gain and phase are converted to I and Q components and stored to hard disk. Data acquisition is controlled by a computer program that runs in the IBM-PC computer.

#### 7.0 OVER-SAMPLING

Under ideal conditions the gain and phase need be sampled only at  $\lambda/2$  intervals (or slightly more often if one is near the reactive near-field of the test object). We oversample by a factor of ten because: 1) noise generated in the electronics for gain and phase detection smears out the spectral content of the signal being measured; 2) a general rule of thumb in digitizing and processing noisy signals is that one should digitize at five to ten times the Nyquist rate; 3) filtering techniques can be used to reduce the (uncorrelated) noise on the signal; 4) nonlinear filtering techniques can be used to detect and correct invalid phase measurements caused by phase wrap-around, and 5) room reflections produce spectral components with spatial frequencies very near the spatial Nyquist frequency. The measured noise will be uncorrelated from sample to sample if digitizing is performed at a rate that is at least an order of magnitude slower than the reciprocal of the IF bandwidth.

The data are sampled at  $\lambda/20$  intervals during scanning. The algorithm to detect glitches that occur in the measured phase values (due to phase wrap-around in the gain/phase receiver) uses differentiation to enhance noise and attenuate low-frequency deterministic signal content<sup>6</sup>, and Tchebycheff's Inequality<sup>7</sup> to detect unusually large noise peaks that are due to the phase glitches. Tchebycheff's Inequality relates the probability of deviation of a sample of a stochastic process from its expected value, to the variance of the process, as

$$P\{|\mathbf{X}-\mu| \geq n\sigma\} \leq n^{-2} \quad (30)$$

where

$$\mu \equiv E\{\mathbf{X}\} \quad (31)$$

$$\sigma \equiv E\left\{(\mathbf{X}-\mu)^2\right\} \quad (32)$$

are the expected mean and variances, respectively. For example, if  $\mathbf{X}$  is the I signal's derivative, and  $n=3$ , then  $\mathbf{X}$  will deviate from its mean by an amount  $3\sigma$  with probability no larger than 0.111, irrespective of the probability density function of the stochastic process. With appropriate choice of  $n$ , this technique detects phase glitches reliably without triggering on noise components that are indeed part of the receiver's noisy output signal.

The detected phase glitches in I and Q are patched over by interpolation and a low-pass spatial filter is applied to I and Q.

While averaging groups of ten adjacent samples is a straight forward approach to filtering, it distorts the higher spatial frequency components of the desired signal. We use a 21-term linear-phase low-pass finite-impulse-response filter which is applied to the over-sampled raw data to improve the signal to noise ratio. The filter response is down 0.7 db at spatial frequencies of  $1/\lambda$ , and 50 db down at  $4/\lambda$ . The filtered data are resampled at  $\lambda/2$  and stored to disk. Spatial filtering imposes no time performance penalty since the computer is idle during the scan re-trace interval.

By means of power spectral analysis of the raw and filtered data sets we determined that the I and Q signals are down at least 25 db at  $1/\lambda$ , and that phase glitch correction and spatial filtering lower the effective noise floor by typically 10 to 15 db.

#### 8.0 VERIFICATION APPROACH

Since the experimentally-determined scattering matrices are defined at discrete values of  $\bar{K}$  and  $\bar{L}$ , it is convenient to construct one's theoretical models of scattering such that the precise values of  $\bar{K}$  and  $\bar{L}$  calculated by the analysis software can be automatically plugged in to yield the theoretical scattering values. From an algorithmic standpoint, this corresponds to implementing the theoretical or numerical model of scattering as a

subroutine that has as input the values of  $\bar{K}$  and  $\bar{L}$  for which a theoretical prediction is needed.

We are taking a three-part approach to verifying the equipment and theory. In the first part, we performed a standard near-field antenna measurement on a known antenna, processed the data using analytic probe pattern for probe correction, and compared the resulting pattern data to known data for the antenna. The result of this step was verification of the near-field antenna measurement capability (equipment, data acquisition and analysis software). Since the first part of the BRCS data analysis is essentially a near-field antenna solution, this provided a partial validation of the BRCS software.

In the second part we performed near-field antenna measurement on a known target (conducting sphere) with known quasi-plane-wave illumination in the  $E_\theta$  and  $E_\phi$  planes. The usual near-field antenna data analysis was performed using a high-density grid, and the results compared with predictions. The result of this part was verification of the prediction and comparison software.

The third part consists of performing the full-up bistatic scan with both transmit and receive probe antennas in motion. The measured data will be processed as described above to yield the scattering matrix for the object. The results of this part will

be verification of the bistatic analysis software and an evaluation of the feasibility of the PWSM bistatic RCS algorithm. Both separate and overlapping scan patterns will be evaluated.

#### Acknowledgments

This work is sponsored by the Rome Air Development Center, Applied Electromagnetics Division, Hanscom Air Force Base, MA.

#### References

1. Dinallo, M.A. (1984) Extension of Plane-Wave Scattering Matrix Theory of Antenna-Antenna Interactions to Three Antennas: A Near-Field Radar Cross-Section Concept. Paper presented at the 1984 A.A.S. Symposium.
2. Yaghjian, A.D. (1984) Approximate Formulas for the Far-Field and Gain of Open-Ended Rectangular Waveguide, I.E.E.E. Trans. Ant. Prop., Vol 32, No. 4., April 1984.
3. Kerns, D.M. (1981) Plane-Wave Scattering-Matrix Theory of Antennas and Antenna-Antenna Interactions, Monograph No. 162, National Bureau of Standards, June 1981.
4. Yaghjian, A.D. (1986) An Overview of Near-Field Antenna Measurements, I.E.E.E. Trans. Ant. Prop., Vol. 34, No. 1, January 1986.
5. Joy, E.B. and Paris, D.T. (1972) Spatial Sampling and Filtering in Near-Field Measurements, I.E.E.E. Trans. Ant. Prop., Vol. 20, No. 3, May 1972.

6. Jenkins, G.W. and Box, G.E.P. (1976) Time Series Analysis: Forecasting and Control, Holden-Day, San Francisco.
7. Papoulis, A. (1965) Probability, Random Variables, and Stochastic Processes, McGraw-Hill, New York, p. 150.



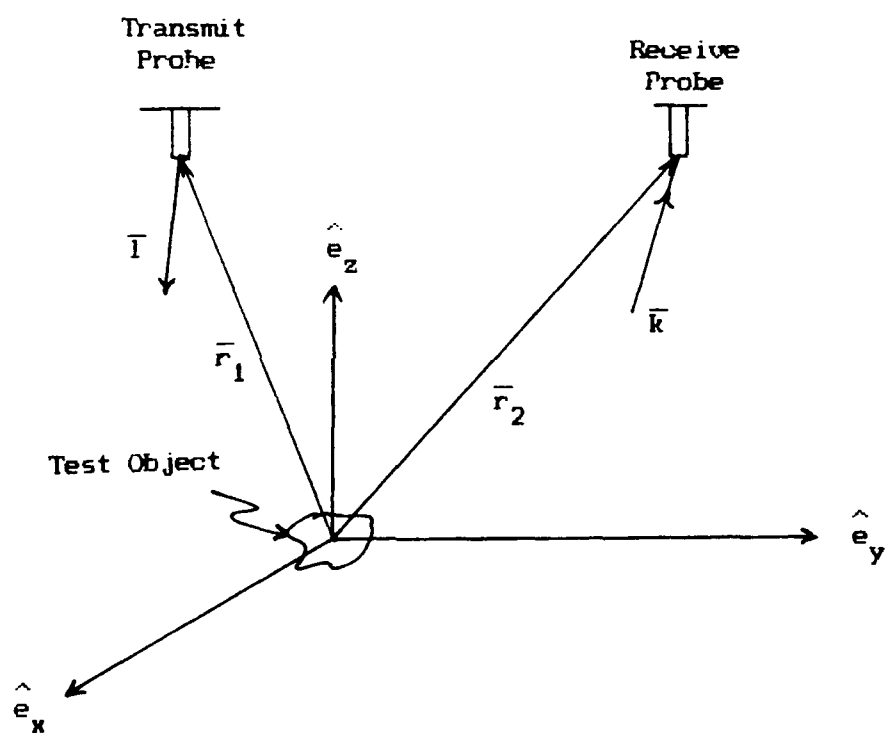


Figure 1 -- Coordinate System

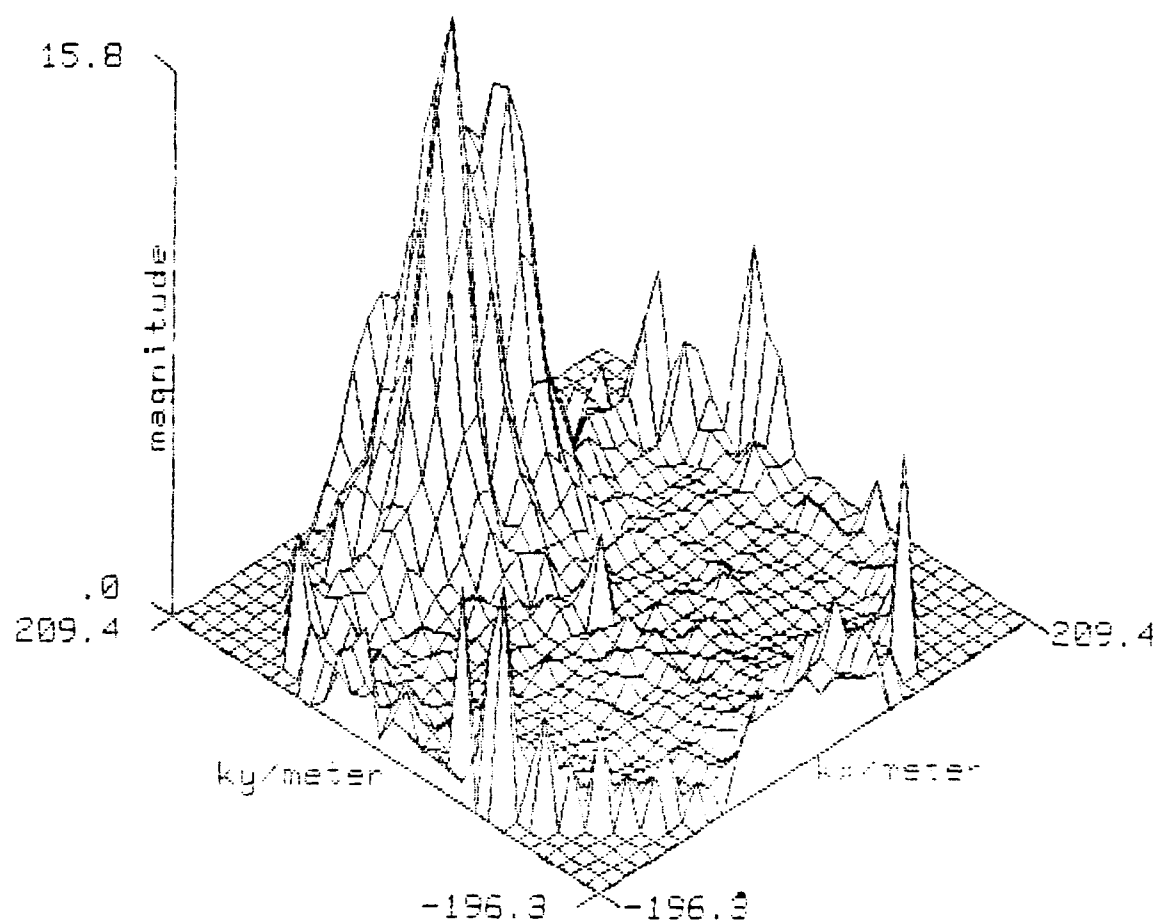


Figure 2 -- Typical Measured Angular Spectrum

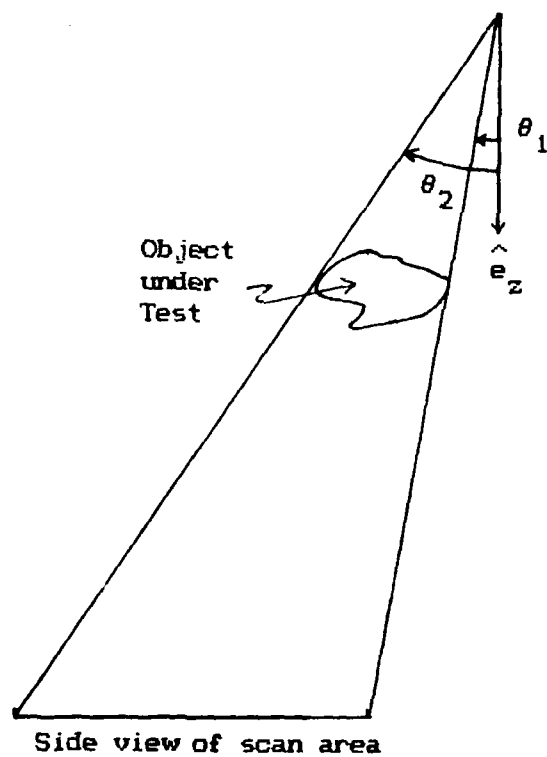


Figure 3 -- Sampling Geometry Constraint on  $\theta$

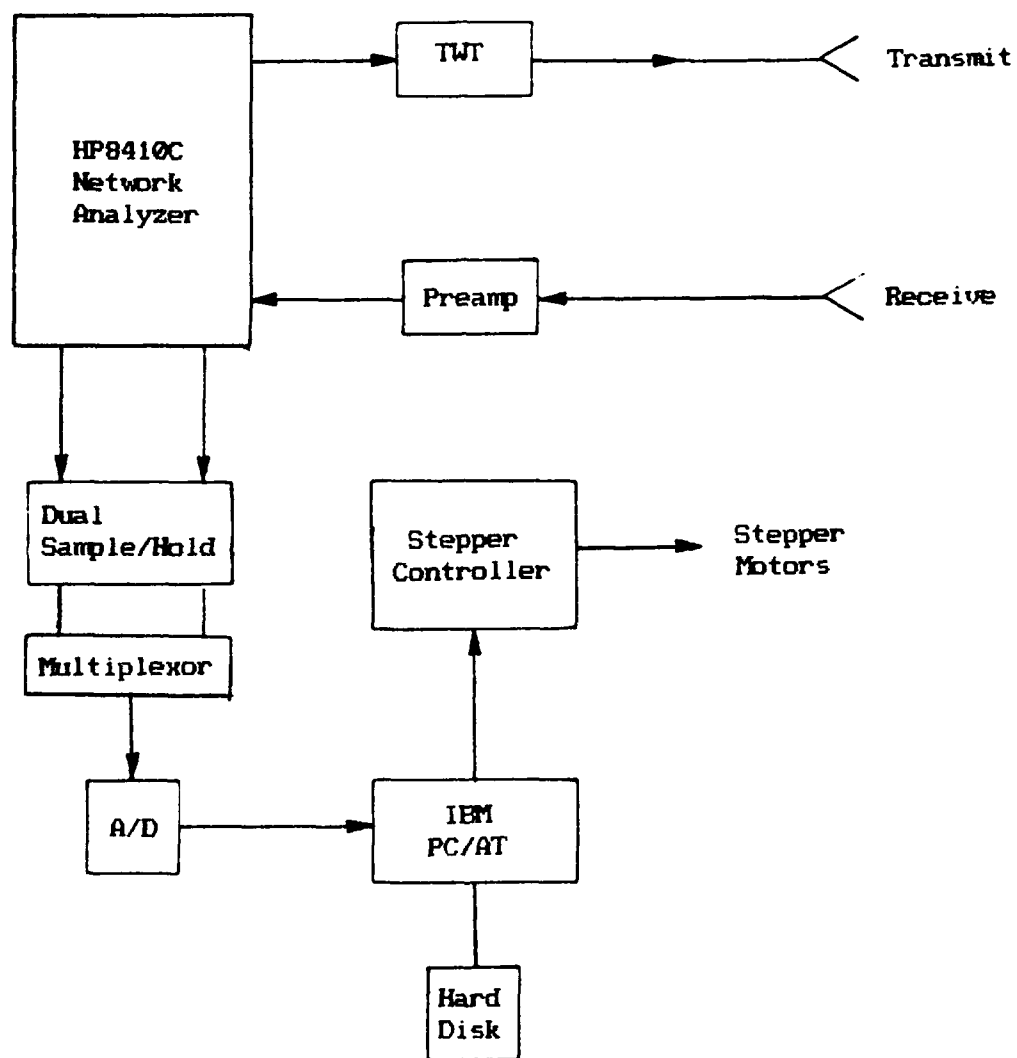


Figure 4 -- Apparatus

FIELD UNIFORMITY CRITERIA FOR THE DESIGN OF  
A TWO-WIRE EMP SIMULATOR

C. Zuffada

Kaman Sciences Corporation, Dikewood Division  
Santa Monica, California 90405

N. Engheta

Formerly with Kaman Sciences Corporation, presently with  
The Moore School of Electrical Engineering  
University of Pennsylvania  
Philadelphia, PA 19104-6390

ABSTRACT

This paper discusses a criterion useful in the design of a two-wire simulator in order to optimize the uniformity of the incident EM fields within the volume occupied by a test object. It is shown that the separation between the two wires  $2a$  and their height above the ground  $b$  can be chosen in such a way to minimize a functional describing the deviation from uniformity, in the sense of the root-mean-square value, of the principal component of the electric field in a cross section of the volume occupied by the test object. Measurements performed on an actual two-wire illuminator verify that, when this criterion is implemented in the design, the field uniformity is satisfactory.

## 1. INTRODUCTION

The purpose of the analysis described in this paper is to support the design of an illuminator for EMP (Electromagnetic Pulse) hardness surveillance. The antenna, shown in Figure 1, consists of two wires in a configuration similar to a rhombus connected to a generator at one vertex and to a matched termination load at the other vertex. At the section PP' the wires are supported by a dielectric cord stretched between two poles. The mechanical arrangement allows for the wire separation and height above the ground to be varied within an ample range, thus offering design flexibility. The portion of the system on the left of section PP' will be referred to as the launch region, whereas that on the right is the termination region. The object to be tested occupies the volume indicated by V, which will be referred to as the working volume. The generator can drive the wires at either the same voltage (common mode) or at voltages of opposite polarity (differential mode).

When the structure rests on a perfectly conducting ground and has a matched termination, it has been shown [1], [2], for the common mode excitation that, at low frequencies, the currents along the wires are well approximated by travelling waves and that the system behaves like a two-wire transmission line with a spherical wavefront operating in the TEM mode. Furthermore, since in the present case the angle  $\alpha$  indicated in Figure 1 is maintained

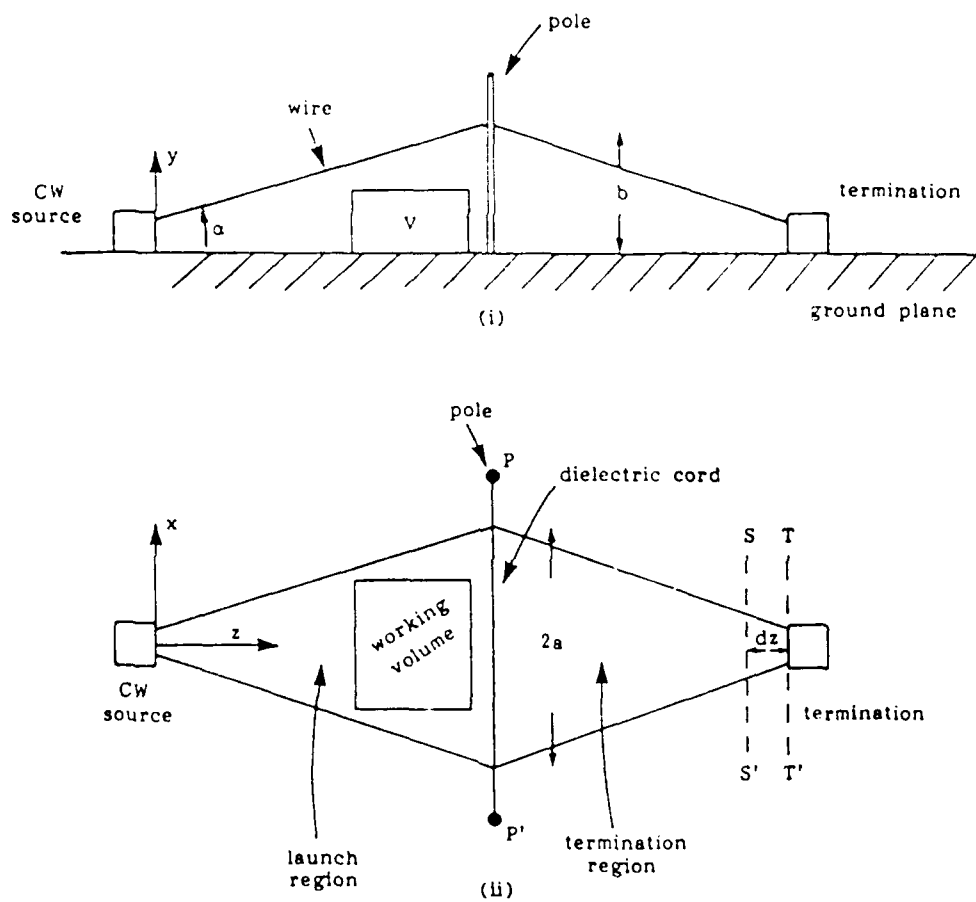
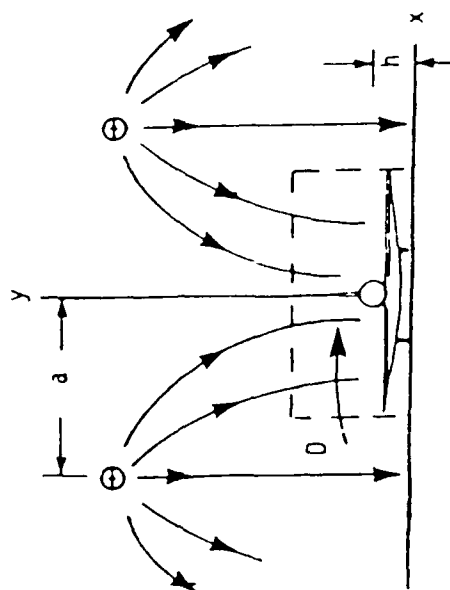


Figure 1. (i) Front view of a rhombic illuminator  
(ii) Top view of a rhombic illuminator

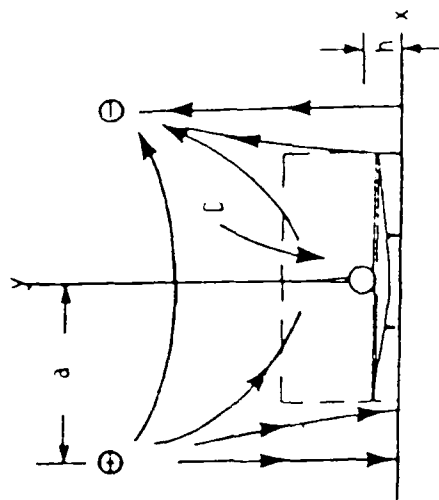
small in the launch region, the portion between wires and ground of the surface of the sphere (wavefront) which has the source as origin and  $z$  as radius (see Fig. 1) can, with a good approximation, be taken to be its projection on the plane  $x$ - $y$ .

As the frequency is increased the travelling-wave transmission line model is not truly valid anymore and both the current and the fields exhibit a standing wave behavior. Moreover, longitudinal components of the electromagnetic fields appear in addition to transverse components. However, for most of the frequency range of interest to us, on each transverse plane, the formal distribution of the dominant component of the fields can still be reasonably approximated by those of a transmission line. The EM fields of a two-parallel-wire transmission line above a perfectly conducting plane operating in the TEM mode in any plane transverse to the  $z$ -axis are well known from static analysis. Such distribution is sketched in Figure 2 for both the common mode and the differential mode. It is observed that, in a region  $D$  between the wires and the ground which is a cross section of the working volume, for the common mode excitation the electric field is predominantly vertical, whereas for the differential mode it is mostly horizontal. When performing EMP hardness surveillance tests one is concerned with illuminating a test object with electromagnetic fields which are as close as possible to those of a plane wave, i.e., uniform in any transverse plane. Therefore, the





(a)



(b)

Figure 2. Cross section view of the geometry showing the working volume.  
(a) Common mode excitation (b) Differential mode excitation

main goal of this analysis was to determine the geometrical configuration of the wires, i.e., separation  $2a$  and height  $b$  above the ground (see Fig. 2) which give the most uniform field in a prescribed region D, for both common mode and differential mode operations.

## 2. MATHEMATICAL FORMULATION

The transverse EM fields of a transmission line operating in the TEM mode can be determined by solving the static problem of two infinitely long, uniformly charged, parallel wires above a perfectly conducting ground plane. This two-dimensional problem is described by the Cartesian coordinate system presented in Figure 2. The distribution of the fields everywhere in the  $x$ - $y$  plane is easily obtained by applying the method of images and superposition. When the charge has the same sign on both wires (corresponding to the common mode) the electric field in the region D is predominantly directed along the  $y$ -axis. Such dominant component is given by

$$E_y = \frac{q}{2\pi\epsilon_0} \left\{ \frac{y-b}{(x-a)^2 + (y-b)^2} + \frac{y-b}{(x+a)^2 + (y-b)^2} - \frac{y+b}{(x-a)^2 + (y+b)^2} - \frac{y+b}{(x+a)^2 + (y+b)^2} \right\} \quad (1)$$

where  $q$  is the wire charge per unit length and  $\epsilon_0$  is the vacuum electric permittivity. On the contrary, when the wires have

opposite charge (corresponding to the differential mode) the electric field in D is predominantly directed along the x-axis. Such dominant component is

$$E_x = \frac{q}{2\pi\epsilon_0} \left[ \frac{x+a}{(x+a)^2 + (y-b)^2} - \frac{x-a}{(x-a)^2 + (y-b)^2} - \frac{x+a}{(x+a)^2 + (y+b)^2} + \frac{x-a}{(x-a)^2 + (y+b)^2} \right] \quad (2)$$

Within a prescribed region D the uniformity of the field depends on the choice of a and b. As a criterion to quantify the extent of uniformity we introduce a functional  $F(E_\delta, a, b, D)$  [3], which gives the relative deviation, i.e., the 2-norm error, of any of the relevant components of the field with respect to the average value taken in D. In its general form  $F(E_\delta, a, b, D)$  is defined as

$$F(E_\delta, a, b, D) = \left\{ \frac{1}{|D|} \int_D (E_\delta(a, b, \epsilon) - E_\delta^{\text{ave}}(a, b))^2 d\epsilon \right\}^{1/2} / E_\delta^{\text{ave}}(a, b) \quad (3)$$

where  $E_\delta$  is either  $E_y$  for the common mode or  $E_x$  for the differential mode and  $\epsilon$  is a variable describing the domain D.

Moreover,  $E_{\delta}^{ave}$  is defined as

$$E_{\delta}^{ave} = \frac{1}{D} \int_D E_{\delta}(a,b,\xi) d\xi \quad (4)$$

Since we are concerned here with test objects such as aircraft whose cross sections exhibit a maximum linear dimension which is greater than the others,  $D$  can be taken to be a straight segment either lying parallel to the  $x$ -axis (representing the wings) or along the  $y$ -axis (representing the cross section of the fuselage and tail) at a certain height  $h$  above the ground. This choice allows us to carry out the integrals in Eq. (3) and Eq. (4) analytically. Once  $F$  is constructed, the maximum uniformity is achieved by choosing  $a$  and  $b$  such that  $F$  is minimum in  $D$ . Moreover, since  $a$  and  $b$  are independent parameters it might be useful to introduce an additional constraint based, for instance, on the behavior of the field or its derivatives at one point, to establish a relationship between  $a$  and  $b$ , thus eliminating one parameter. For the case of the common mode excitation one such relationship exists [4] that provides a good uniformity in a local region around the center of the structure, coincident with the origin of the coordinate system (from Fig. 2), where the field is strong. Such relationship is  $a/b = 1/\sqrt{3}$  and it has been incorporated in our analysis. For the differential mode excitation a

correspondent relationship was not found because in this case the origin is a point when the field goes to zero.

Once the integrations in Eq. (3) and Eq. (4) are carried out one is left with transcendental functions of  $a$  and  $b$  which are then minimized graphically.

For the sake of brevity the explicit expressions are not reported here.

Figure 3 presents the resulting 2-norm error over the wings for the common mode excitation, as a function of  $a/h$ . The relationship  $a/b = 1/\sqrt{3}$  is here used. It is seen that the error decreases rapidly and for  $a/h > 5$  it is bounded by 5 percent. From this curve, for any prescribed maximum deviation, one can immediately determine a range of possible values for  $a$ , and consequently for  $b$ , which satisfies the requirement.

Figure 4 illustrates the 2-norm error, again over the wings, for the differential mode excitation. In this case, one is concerned with a family of curves with the variable  $b/h$  on the abscissa axis while  $a/h$  acts as a parameter, assuming discrete values. A dual representation, with the roles of  $a$  and  $b$  interchanged, provides exactly the same information. Again it is noted that the error decreases when  $a/h$  and  $b/h$  increase. Also, for  $a/h$  and  $b/h$  large, which represent a realistic situation, the minima of the curves are fairly broad, emphasizing that the choice of  $a$  and  $b$  is not critical within a certain range of values. Charts

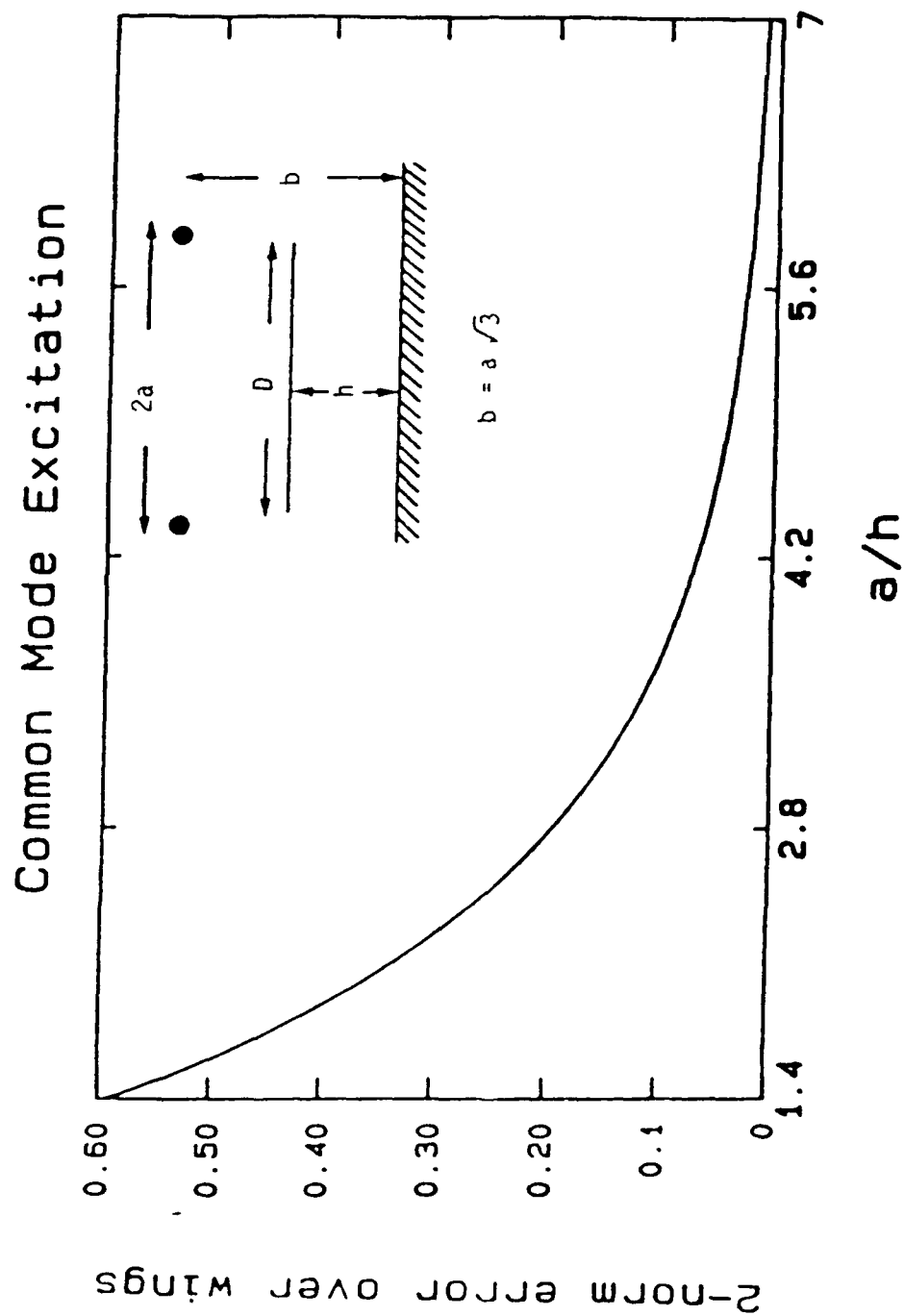
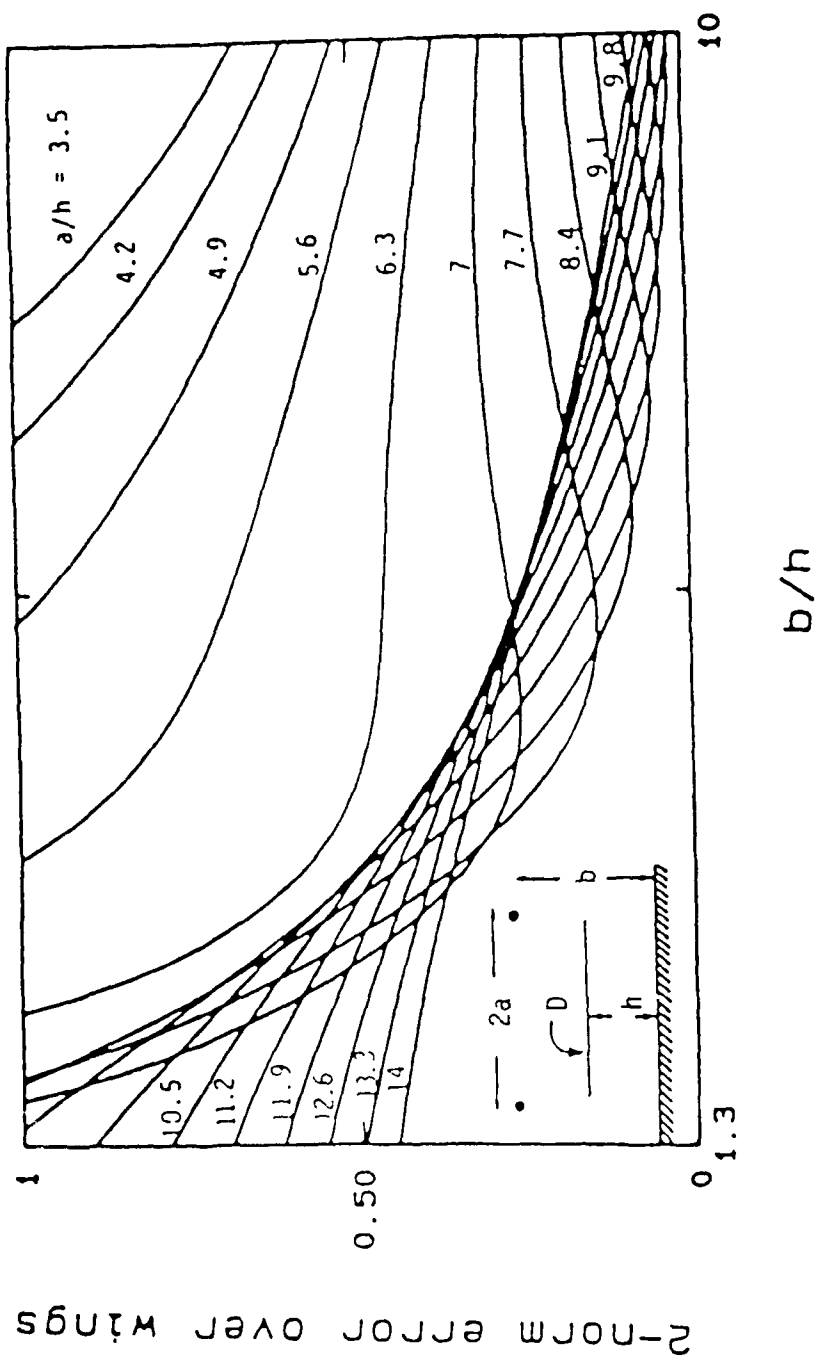


Figure 3. 2-norm error over wings as a function of  $a/h$ .

# Differential Mode Excitation



like those of Figure 3 and 4 are directly useful to the designer in choosing the optimum  $a$  and  $b$  within a range of possible values, compatibly with other constraints, such as test site area, pole length, etc.

### 3. IMPEDANCE CALCULATIONS

For good performance, illuminators of this type are usually terminated into a resistive load of value equal to the characteristic impedance  $Z_C = V/I$  of the transmission line at the ending section. Using again the static model for two parallel wires to calculate the voltage and after dividing by the current, it is obtained

$$Z'_C = \frac{n_0}{4\pi} \left\{ \ln \left[ \frac{1 + \sqrt{1 + (R/b)^2} - R/b}{1 - \sqrt{1 + (R/b)^2} + R/b} \right] + \frac{1}{2} \ln [1 + (b/a)^2] \right\} \quad (5)$$

for the common mode and

$$Z''_C = \frac{n_0}{\pi} \left\{ \ln \left[ \frac{1 + \sqrt{1 + (R/a)^2} - R/a}{1 - \sqrt{1 + (R/a)^2} + R/a} \right] - \frac{1}{2} \ln [1 + (a/b)^2] \right\} \quad (6)$$

for the differential mode, where  $R$  is the radius of the wire and  $n_0 = 377 \Omega$  is the free-space intrinsic impedance. It is pointed out that in both cases the characteristic impedance consists of the sum of two terms; one, depending either on the ratio  $R/b$  (common mode) or  $R/a$  (differential mode) is the dominant contribution, while the other, depending on the ratio  $a/b$ , pro-



impedance at  $PP'$ . This can be of great help in reducing reflections. Unfortunately, this correction cannot be applied to the launch region because here  $d/dz \{Z_c\}$  is positive and one would have to "subtract" a resistance  $d/dz \{Z_c\} dz$  for every portion  $dz$  of wires.

It is pointed out that the reflections and scattering originating at the wire bends are not affected by this measure and hence they are still present.

One might try to mitigate this effect by making a smooth transition around the poles instead of having a sharp bend.

#### 4. CONCLUSIONS

A criterion is presented to help in selecting the wire separation and height above the ground in the design of a rhombic illuminator, such that the most uniform fields in a prescribed working volume are obtained. In addition some impedance considerations which help to reduce the reflections in the working volume are also given. The above criterion and impedance considerations were applied in the design of a low level CW illuminator. Unlike the configuration in the model, the real system was built without a conductive ground plane in order to get higher fields near the ground for the differential mode excitation. Results of a preliminary field mapping for the common mode excitation show that the uniformity is satisfactory and that the distribution of the principal component of the electric field in any cross section of the

working volume closely follows that of the model used in the analysis (Eq. 1), with differences of less than a factor of two.

#### ACKNOWLEDGEMENTS

The work reported herein was funded by AFWL, Kirtland AFB, under Contract F29601-84-C-0042, Subtask 04-02. The authors wish to thank C. E. Baum and T. Smith of AFWL, Kirtland AFB and S. Kokorowski, L. Marin, K.S.H. Lee and F. C. Yang of Kaman Sciences Corp., Dikewood Division. They are also grateful to C. Cheung and T. Weimer for performing the numerical computations.

#### REFERENCES

1. Shen, H-M and R. W. P. King (1982) The Rhombic EMP Simulator, IEEE Trans. on Elect. Comp., Vol. EMC-24 (No. 2):255-265.
2. Shen, H-M and R.W.P. King (1982) Experimental Investigation of the Rhombic EMP Simulator: Comparison with Theory and Parallel Plate Simulator, IEEE Trans. on Elect. Comp., Vol. EMC-24 (No. 3):349-355.
3. Baum, C. E. (1985) Personal communication.
4. Baum, C. E.(1970) Impedances and Field Distributions for Symmetrical Two Wire and Four Wire Transmission Line Simulators, Sensor and Simulation Notes, Note 27 AFWL Kirtland AFB.

# A UNIFIED METHOD OF ANTENNA SYSTEM ANALYSIS BASED ON THE PARAMETRIC MODELING OF COMPONENT SCATTERING COEFFICIENTS

W. Milroy, M. Middeke, R. Lewis, M. Thomas, S. Drost

Antenna Systems Laboratory  
Radar Systems Group  
Hughes Aircraft Company, Los Angeles, CA

## Abstract

The ongoing development of a computer-aided design tool for the comprehensive analysis of antenna systems and subsystems is described. Utilizing custom Automated Network Analyzer software, arbitrary N-port devices are fully characterized in terms of scattering coefficients. This data is in turn modeled as a function of frequency and physical variables in order to provide a continuous parametric representation with up to a 50:1 reduction in required storage space. This parametric representation allows for a statistical investigation of antenna system and subsystem behavior in terms of user-specified mechanical and electrical tolerances. Based on an accrued library of scattering matrix characterizations of individual antenna components, the resultant network parameters (VSWR, Isolation, Insertion Loss, and Phase), far-field patterns, and RCS characteristics of ensemble antenna systems and subsystems can be predicted based on simple linear algebra techniques. The analytical theory and mechanics of this approach are discussed along with numerical results for a typical antenna subsystem application.

## 1. Introduction

In an environment of increasingly stringent performance and observability requirements across ever-broadening frequency bandwidths, today's antenna designer must reconsider the soundness of heretofore common analysis assumptions and approximations. Specifically, higher-order reflections and finite isolation effects between adjacent and remote components can no longer be dismissed as negligible, the finite accuracy of theoretical models becomes a point of increasing concern, the imperfections of "perfect" loads take on new significance. Likewise, the prudent specification of internal mechanical and electrical tolerances becomes increasingly critical in optimizing the balance between performance and producibility. In response to these new challenges, we are currently developing a unified approach to the analysis of antenna subsystem and system behavior based on the measurement and utilization of parameterized scattering coefficient data.

Scattering coefficients were chosen over other characterizations (Impedance, Admittance, etc.), because of their straightforward means of measurement and their correspondence to real physical attributes. Figure 1 illustrates an overall flow diagram of our approach which can be conveniently subdivided into two major subtasks.

First, as a resource for the second task, we create and augment the scattering parameter library. This involves the scattering coefficient characterization of a variety of common devices and junctions in terms of frequency and physical variables (iris depths, septum offsets, stripline widths, etc.) over suitable ranges. This raw data is first collected through the utilization of an automated test procedure, transformed and processed in the spatial domain, parameterized in terms of physical variables, and finally stored in condensed form as a member of the scattering parameter library.

The second major subtask is the computation of the composite scattering coefficients (and related characteristics) for user-specified networks comprised of components whose individual scattering coefficients have been previously stored (in condensed form) in the scattering parameter library. These computations are performed over a user-specified range of frequencies for a user-specified set of physical variable settings and tolerances. An executive program manages overall analysis operations in conjunction with a circuit analysis "engine" optimized for the performance of repetitive linear algebra operations.

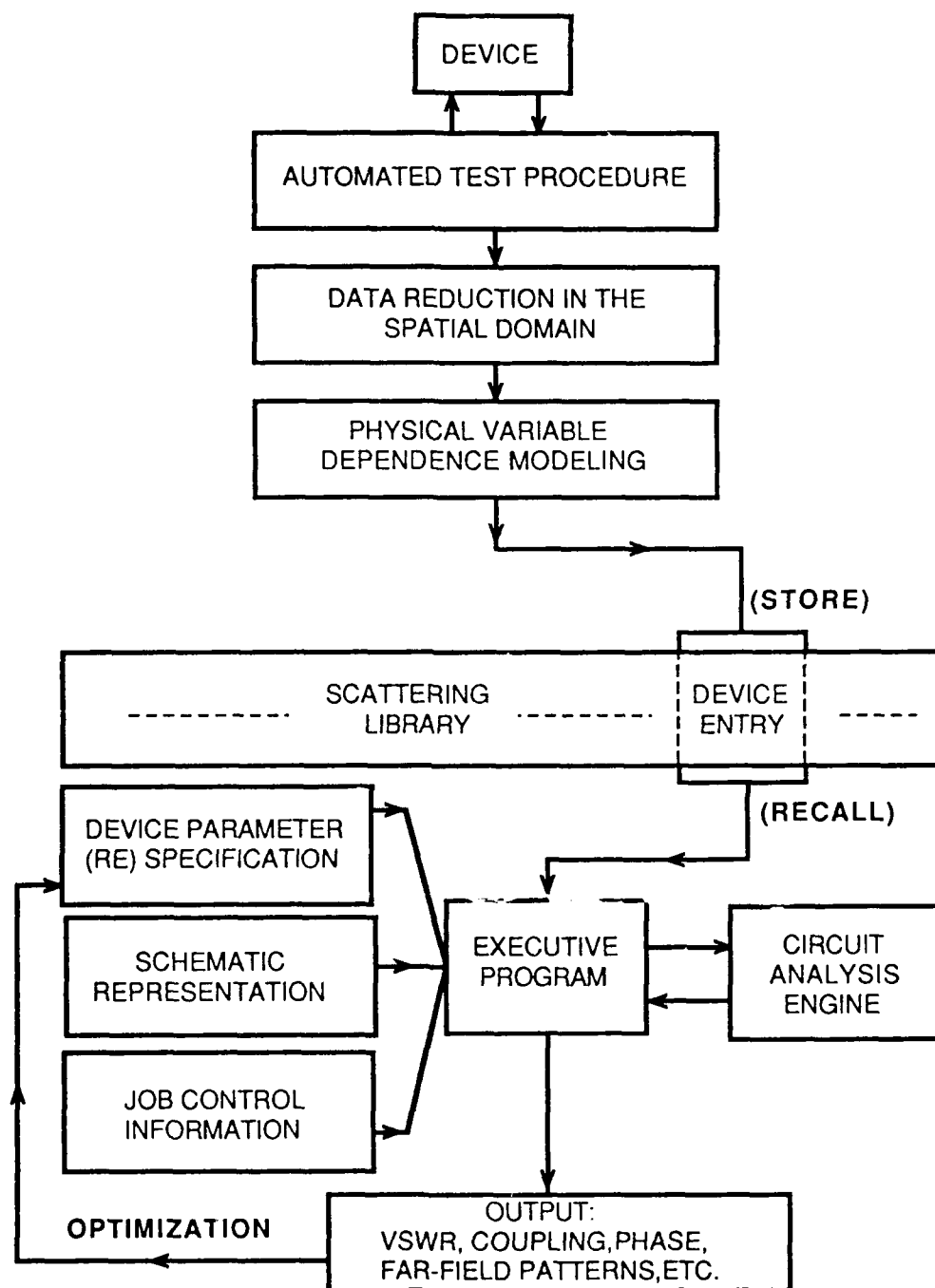


FIGURE 1. OVERALL FLOW DIAGRAM, THE UNIFIED ANALYSIS APPROACH

## 2. Creation and Augmentation of the Scattering Library

### 2.1 Scattering Coefficient Measurement

Figure 2 illustrates the fully-developed automated test procedure in flow diagram form. This procedure is currently software-implemented on an HP8409C Automated Network Analyzer as depicted in Figure 3. Data is temporarily stored on floppy disk at the HP9000 terminal prior to transmission to a mainframe (TSO) computer via a modem switch.

The automated test procedure commences with a series of prompts, at which point the user provides a description of the device under test (device function, reciprocity, number of ports, dataset name.) In addition, interface specifications, interface-to-junction distances, and names are specified by the user for each device port. The prompting sequence continues with user-specification of lower limit, upper limit, and cut-off frequencies plus the desired number of frequency samples (restricted to an integer power of 2 due to the implementation of Fast Fourier Transform (FFT) in later processing.) Based on this information, frequency samples are selected such that they are evenly-spaced in phase constant  $\beta$  in order to provide optimal resolution when transformed to the spatial domain (see Section 2.2.) Finally, the user is prompted for the names, limits, and increments of all physical variables to be associated with the device.

Based on the information provided by the user, an optimized test sequence is formulated and presented to the user for approval. This tabular test plan specifies the minimum number of required permutations of port connections and physical variable combinations, minimized on the basis of device reciprocity and network analyzer capabilities. In addition, data storage space is allocated and initialized with all user-specified device information.

Upon user approval, a calibration procedure is performed and the test sequence is initiated. All required hardware disconnections and connections are explicitly prompted and confirmed step-by-step.

All raw measured data is calibrated at the completion of the test sequence, then formatted prior to transfer to the mainframe computer. Transfer is accomplished via a modem switch with all data echoed for confirmation of error-free transmission.

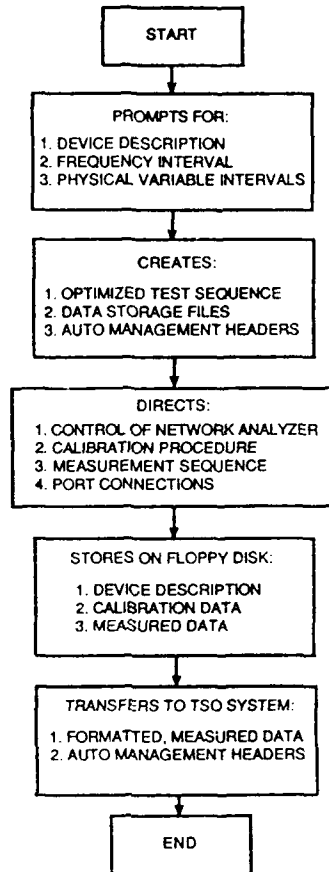


FIGURE 2. FLOW DIAGRAM, AUTOMATED TEST PROCEDURE

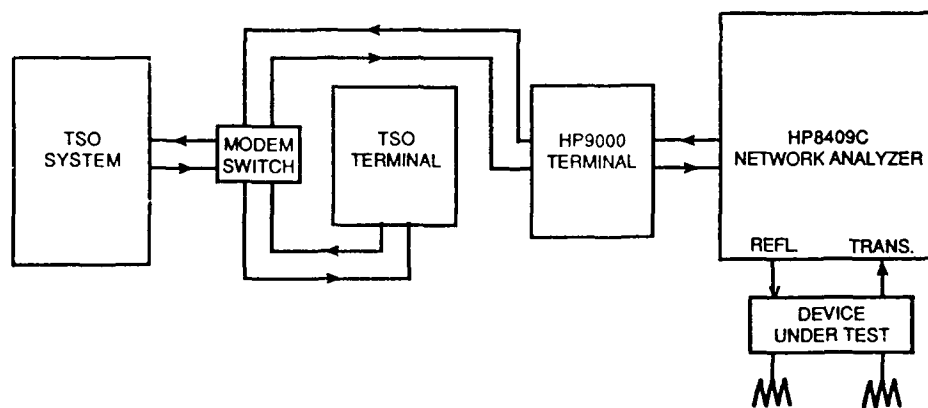


FIGURE 3. TEST SET-UP, AUTOMATED TEST PROCEDURE



## 2.2 Data Reduction in the Spatial Domain

The overall methodology of this facet of the modeling process is illustrated in Figure 4. However, before discussing this approach in detail, it seems appropriate to justify our methods based on some theoretical and physical reasoning.

Calibrated data transferred from the network analyzer to the mainframe computer is in the form of N-frequency samples (for each scattering coefficient), evenly-spaced in phase constant  $\beta$ . Note that we refer to  $\beta$  as the "frequency" domain because of the simple one-to-one relationship between  $\beta$  and  $f$  (directly proportional for  $f_c = 0$ .)

The frequency domain, while the most direct, is not the ideal domain for modeling the physical variable dependence of the individual scattering coefficients. Instead, transformation to the spatial domain is desirable in order to separate frequency and physical dependencies and thereby simplify the modeling procedure. To see this, assume that any particular scattering coefficient can be expressed "exactly" as:

$$S_{mn}(\beta, \underline{x}) = \sum_{k=-\infty}^{\infty} \Gamma_k(\beta, \underline{x}) e^{-j\beta l_k} \quad (1)$$

where  $\Gamma_k(\beta, \underline{x})$  is a discrete complex reflection or transmission coefficient for a discrete frequency- $(\beta)$  and physical variable- $(\underline{x})$  dependent discontinuity located a distance  $l_k$  from a reference plane. These discontinuities may be real or fictitious (higher-order reflection terms.) It is our desire to solve for the reflection/transmission coefficients  $\Gamma_k(\beta, \underline{x})$  at each of the discontinuity positions  $l_k$  given  $S_{mn}(\beta, \underline{x})$ . However, two obstacles block our immediate progress in that direction.

First, the frequency dependence of the reflection/transmission coefficients appears to preclude the direct application of a Fourier Transform between  $\beta$ -space (frequency domain) and  $l$ -space (spatial domain), since Fourier coefficients must be independent of the transform variable. Second, the infinite nature of the summation would indicate that an infinite number of frequency samples of the scattering coefficient would be required. As a solution we propose now (and validate later) the following assumptions.

1. Assume that the frequency dependence of each discontinuity  $\Gamma_k(\beta, \underline{x})$  is weak compared to the frequency dependence of the composite scattering coefficient  $S_{mn}(\beta, \underline{x})$  and can therefore be modeled by a frequency-independent term  $\Gamma_k(\underline{x})$  augmented by a "few" fictitious frequency-independent "sideband" terms  $\Gamma_r(\underline{x})$  adjacent to  $\Gamma_k(\underline{x})$ .

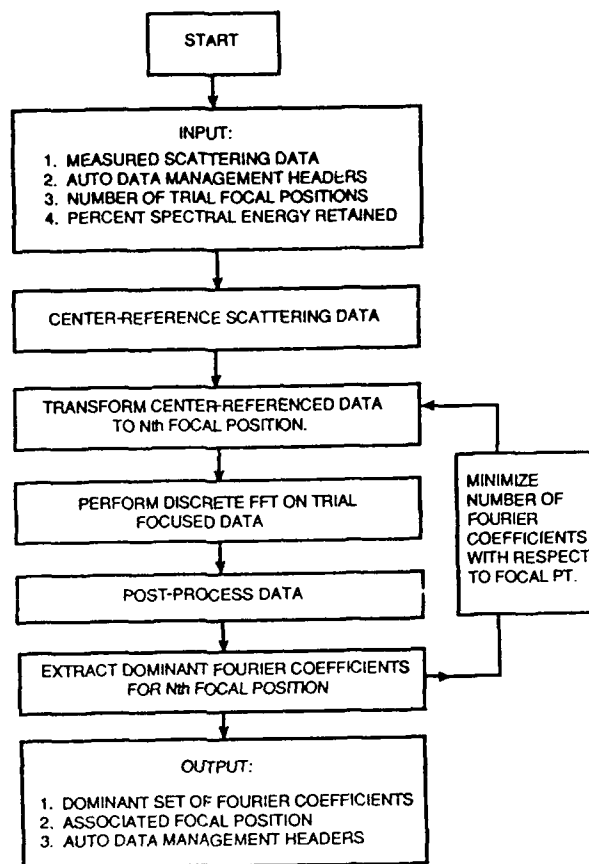


FIGURE 4. FLOW DIAGRAM, DATA REDUCTION IN THE SPATIAL DOMAIN

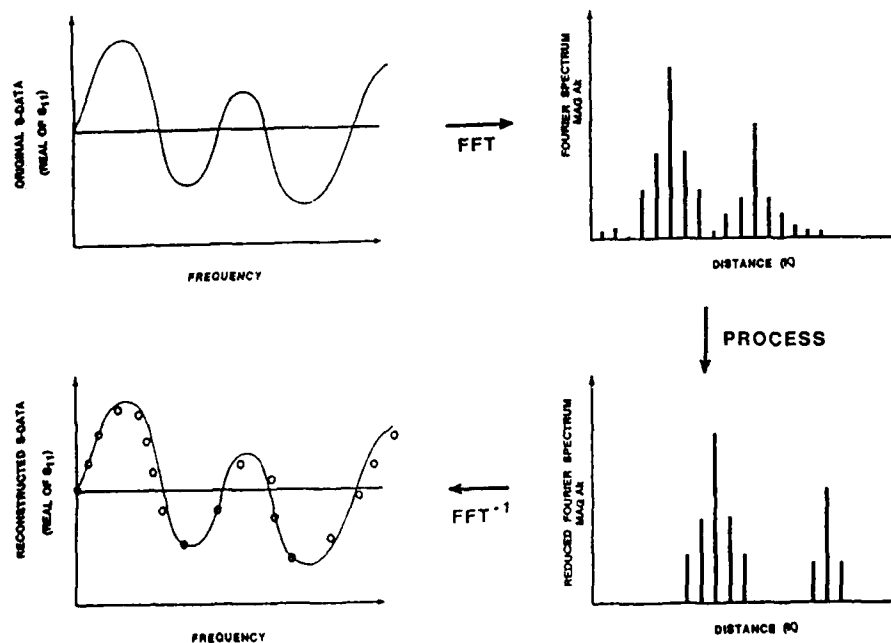


FIGURE 5. DATA REDUCTION IN THE SPATIAL DOMAIN

2. Assume that the  $\Gamma_k(x)$  terms diminish with increasing  $k$  sufficiently quickly, such that the series can be truncated at  $N$  terms.

With these assumptions applied, (1) can be rewritten as:

$$S_{mn}(\beta_i, x) = \sum_{k=0}^{N-1} \Gamma_k(x) e^{-j\beta_i l_k} \quad [i=0,1,2,\dots,(N-1)] \quad (2)$$

which is in a form ideally suited for application of the Fast Fourier Transform (FFT) in order to solve for the  $N$  reflection/transmission coefficients  $\Gamma_k(x)$  at each of the discontinuity positions  $l_k$  given  $N$  frequency samples of the scattering coefficients  $S_{mn}(\beta_i, x)$ .

Given the  $N$  discrete evenly-spaced "frequency" samples  $\beta_i$ , we can solve for the  $N$  discrete evenly-spaced discontinuity positions  $l_k$ . These are easily shown to be:

$$l_k = \frac{(N-1)}{N} \frac{2\pi}{(\beta_{\text{HIGH}} - \beta_{\text{LOW}})} k \quad [k=0,1,2,\dots,(N-1)] \quad (3)$$

where  $\beta_{\text{HIGH}}$  and  $\beta_{\text{LOW}}$  are the phase constants associated with the highest and lowest sample frequencies.

Note that the discrete sampled nature of  $S_{mn}(\beta_i, x)$  and the finite summation limit  $(N-1)$  appearing in (2) imply a minimum resolution  $\Delta l$  and maximum range  $l_{\text{max}}$  in determining discontinuity locations. These limits are easily verified to be

$$\Delta l = \frac{(N-1)}{N} \frac{2\pi}{(\beta_{\text{HIGH}} - \beta_{\text{LOW}})} \quad (4)$$

$$l_{\text{max}} = (N-1) \Delta l \quad (5)$$

Thus, with the application of FFT, we transform the scattering coefficient data from the frequency domain to the spatial domain, thereby removing direct frequency dependence and reducing the modeling problem to that of characterizing the physical variable dependence of each reflection/transmission (Fourier) coefficient. This subject will be covered in detail in Section 2.3.

Note that the discontinuities in a real physical device are usually somewhat localized, therefore it's not at all surprising to discover that the total spectral energy (defined as the sum of the squares of the Fourier coefficient magnitudes) is highly localized as well. We therefore can (and do) exploit this fact in order to dramatically reduce the number of coefficients that must be modeled and stored by selectively retaining only dominant coefficients.

This advantage will be discussed towards the end of this section. Additionally, the physical equivalence between the Fourier coefficients and the actual discontinuity locations and reflection coefficients implies a reasonable expectation that the physical variable ( $x$ ) dependence of the Fourier coefficients will be well-behaved.

With this background in mind, we can now restate our spatial domain modeling approach as follows: **Optimally pre- and post-process the scattering coefficient data in such a way as to retain a minimum number of Fourier coefficients whose physical variable dependence is maximally benign while allowing reconstruction of the scattering coefficients in the frequency domain to an acceptable level of precision.** This procedure is illustrated pictorially in Figure 5. The mechanics of the approach are quite involved, but include some basic "building block" processes.

**Center-referencing** is performed on the scattering coefficient data in the frequency domain for the purpose of removing excessive complex exponential "rotation" through the artificial removal of idealized transmission line lengths. Figure 6 illustrates this process and shows the resultant translation toward the reference plane in the spatial domain.

**Unmasking** is a process by which internal reflection coefficients, attenuated by the presence of large discontinuities near the reference plane, are restored to their isolated magnitude levels. This is accomplished using a coefficient-to-coefficient recursion relation and has the effect of separating the physical variable dependence of specific coefficients, thereby improving overall modeling accuracy. Figure 7a illustrates the transformed reflection data for a two-stub waveguide tuner (pictured in Figure 17) with both stubs protruding halfway into the waveguide. Note the clearly dominant Fourier coefficients associated with the two capacitive stubs and the apparent attenuation of the second dominant coefficient despite the equal penetration of the two stubs. Figure 7b illustrates the spatial domain after application of the unmasking process. Note the amplification of the second coefficient and the (now apparent) pseudo-discontinuity corresponding to the second-order reflection contribution.

**Focusing** is a method by which small idealized transmission line lengths are added or removed in the frequency domain in order to enhance spectral energy concentration in the spatial domain, thereby minimizing the number of Fourier coefficients which must be modeled and retained. Optimal focusing is accomplished when the actual physical location of the dominant discontinuity in the spatial domain falls directly on a discrete  $l_k$  value. The required focusing shift range is therefore restricted to the width of one resolution cell  $\Delta l$ . Figure 8a

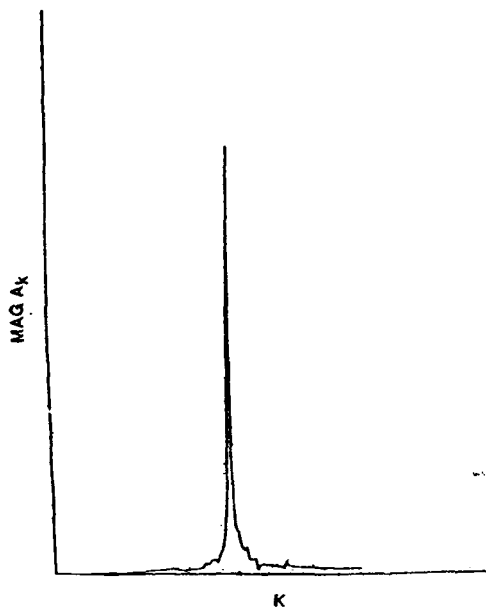


FIGURE 6a. NONCENTER-REFERENCED DATA, SPATIAL DOMAIN

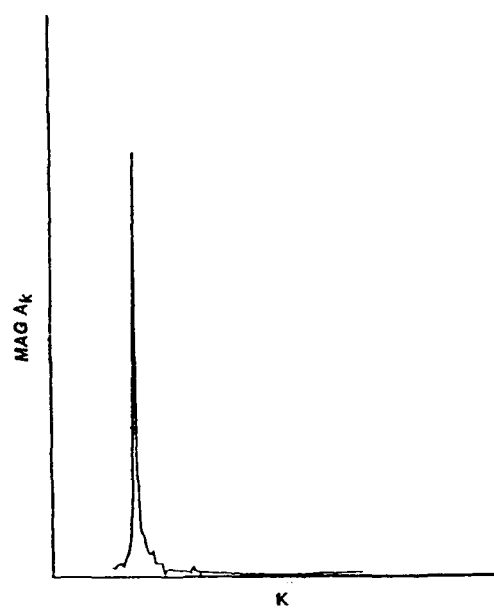


FIGURE 6b. CENTER-REFERENCED DATA, SPATIAL DOMAIN

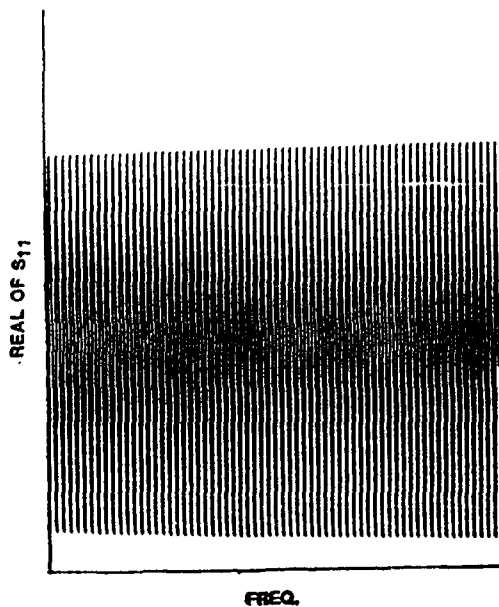


FIGURE 6c. NONCENTER-REFERENCED DATA, FREQUENCY DOMAIN

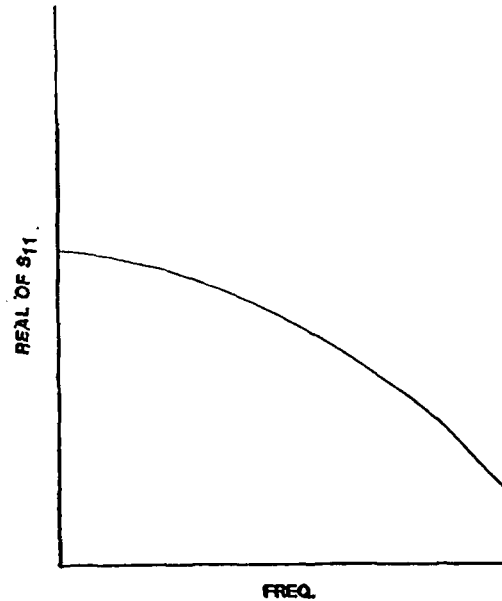


FIGURE 6d. CENTER-REFERENCED DATA, FREQUENCY DOMAIN

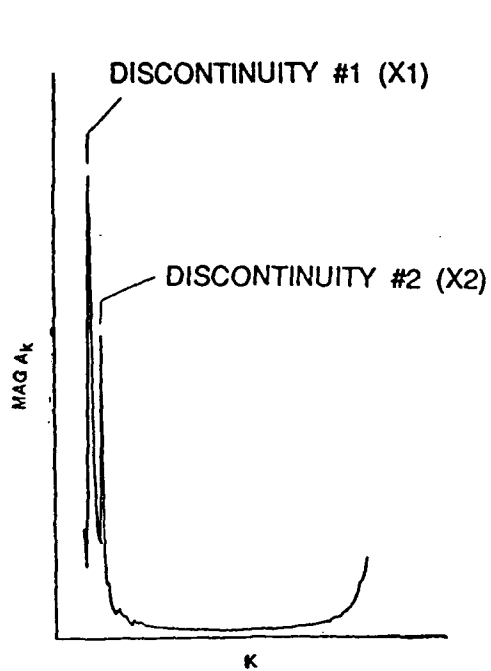


FIGURE 7a. BEFORE UNMASKING,  
SPATIAL DOMAIN

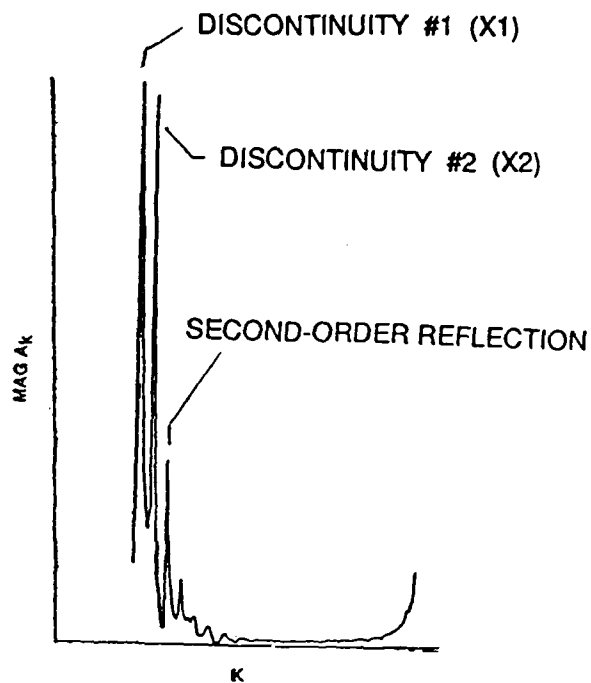


FIGURE 7b. AFTER UNMASKING,  
SPATIAL DOMAIN

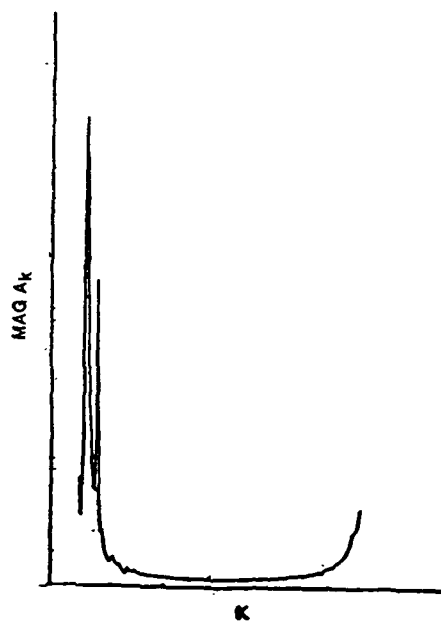


FIGURE 8a. BEFORE FOCUSING,  
SPATIAL DOMAIN

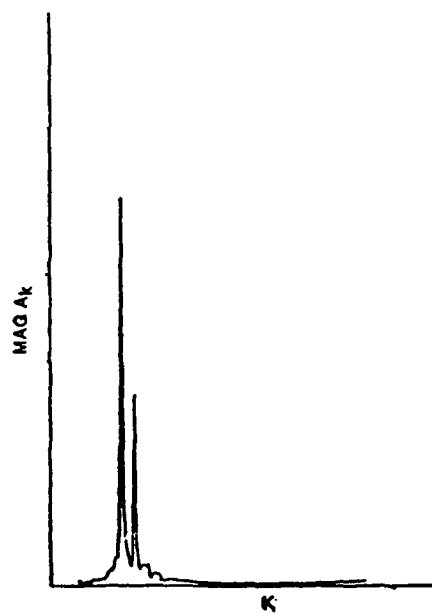


FIGURE 8b. AFTER FOCUSING,  
SPATIAL DOMAIN

illustrates the spatial domain for the two-stub tuner before focusing. Note the enhanced spectral energy concentration after focusing as illustrated in Figure 8b.

The reason for the improvement due to focusing is best understood by considering the case of a single theoretical discontinuity of unit reflection coefficient magnitude, located precisely at the  $l = l_i$  position. As illustrated in Figure 9, the frequency response for this discontinuity, when transformed to the spatial domain, yields a precise unit impulse function at the  $k = i$  position. Now consider the same discontinuity shifted to the position  $l = l_i + (\Delta l/2)$ . Figure 10 illustrates the spatial domain for this case, revealing equal and opposite impulses of magnitude  $(2/\pi)$  located at the adjacent positions  $k = i$  and  $k = (i+1)$ . A significant sideband structure is now evident, requiring the retention of numerous coefficients in order to adequately model this discontinuity, and hence the value of focusing becomes apparent.

We will now validate our previous assumption that a mildly frequency-dependent discontinuity can be modeled by a frequency-independent discontinuity together with an adjacent sideband structure. Figure 11 illustrates the spatial domain for a frequency-independent discontinuity located at the physical position  $l = l_i$ . Figure 12 illustrates the normalized spatial domain for a linearly frequency-dependent discontinuity located at the identical position. (The magnitude of the reflection coefficient varies linearly by 22 percent over a 40 percent frequency bandwidth.) Note the small sideband structure now evident at the base of the main impulse.

Recall that we previously assumed that we could truncate the infinite series (1) to a finite N-term series (2) without a loss in accuracy. In the spatial domain, this is the equivalent of imposing a finite (spatial) bandwidth limitation. That is to say, we require that no total electrical path length, regardless of reflection order, can be greater than the distance  $l_{\max}$  (5.) For the typical application of a WR-90 waveguide-based device, sampled at 256 evenly-spaced samples in  $\beta$ , over the frequency range of 8 to 12 GHz, we compute  $\Delta l$  and  $l_{\max}$ , based on (4) and (5), to be 2.16 and 551 inches respectively. In this particular case then, the validity of the truncation hinges upon the very reasonable assumption that all higher-order reflections within the device have dissipated to zero for path lengths greater than 46 feet!

We mentioned earlier that we can dramatically reduce data storage requirements by exploiting the localization of spectral energy in the spatial domain, thereby requiring the modeling and storage of only a "few" dominant Fourier coefficients with a minimal loss in overall modeling accuracy. This economy is illustrated in Figure 13 where the concentration of the majority of spectral energy (for the two-stub tuner) in a minority of Fourier coefficients is

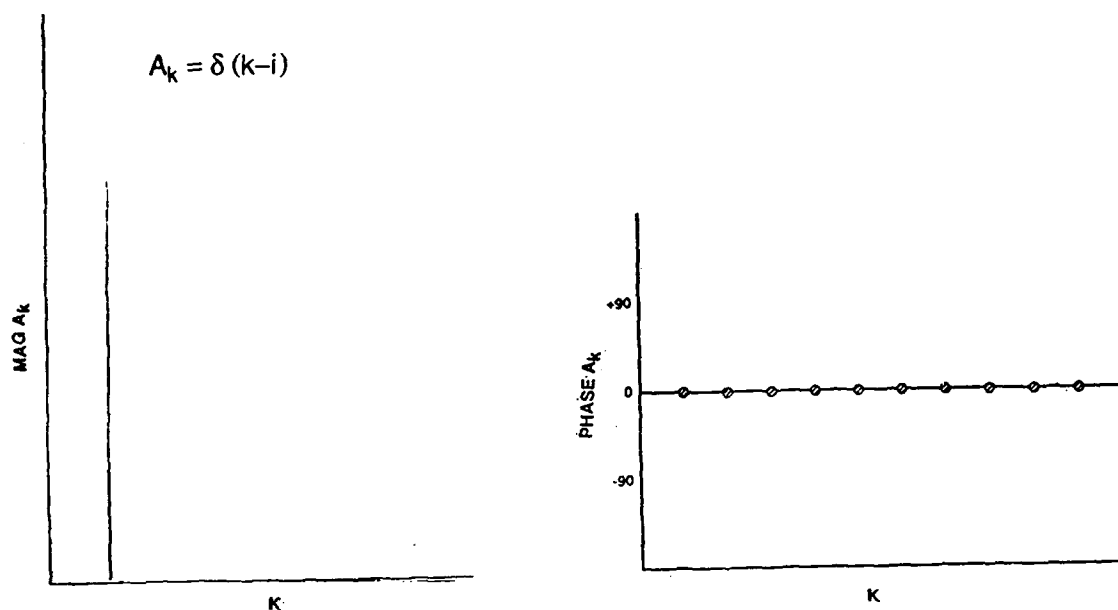


FIGURE 9. INTEGER-POSITIONED DISCONTINUITY, SPATIAL DOMAIN

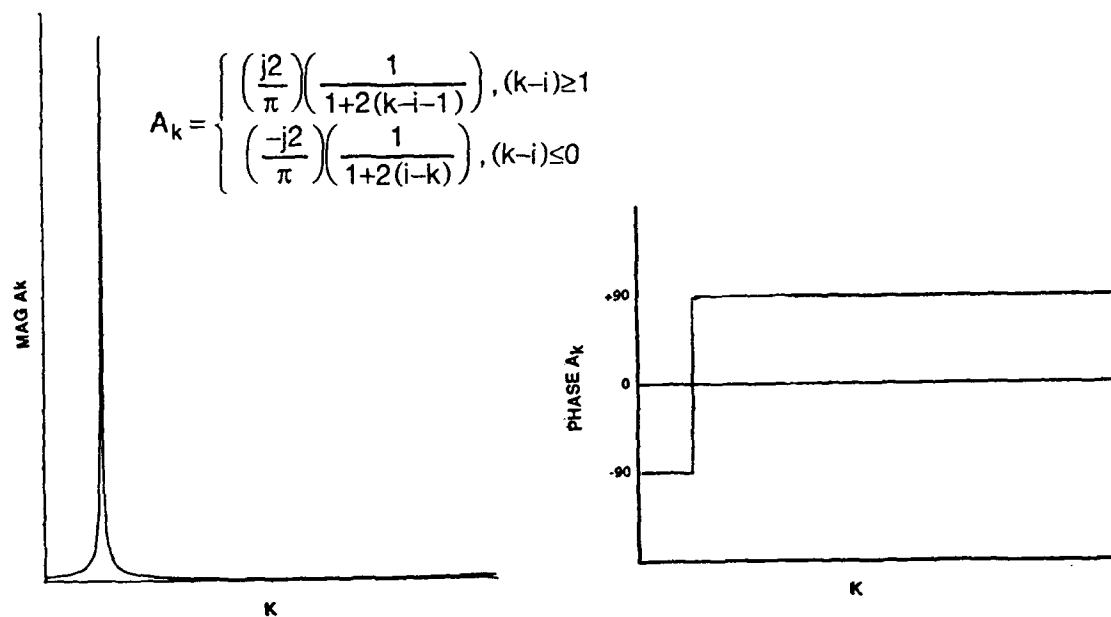


FIGURE 10. HALF-INTEGER-POSITIONED DISCONTINUITY, SPATIAL DOMAIN



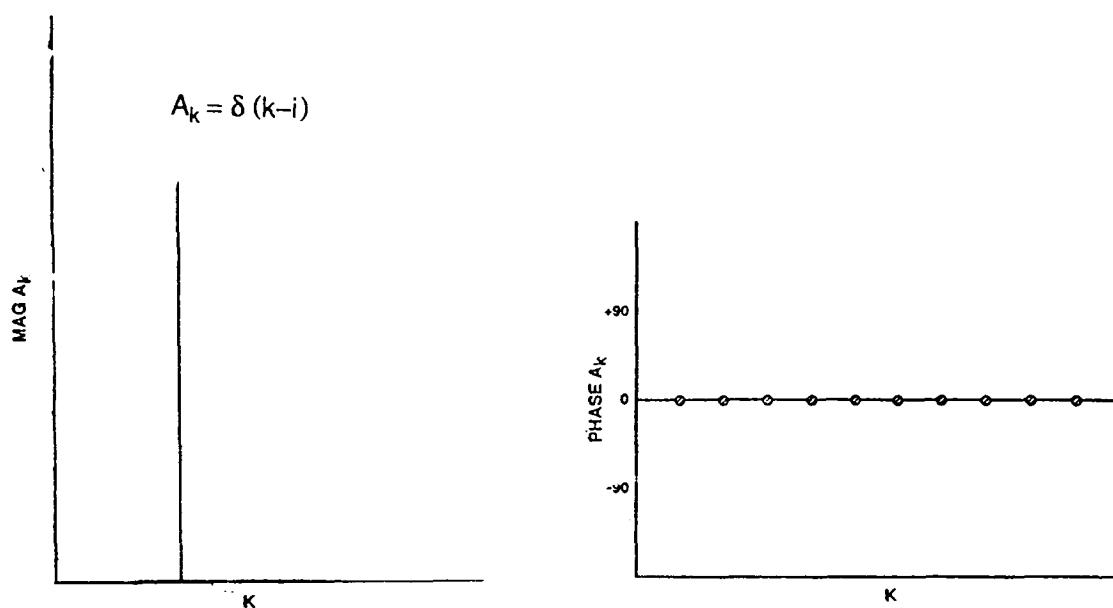


FIGURE 11. FREQUENCY-INDEPENDENT DISCONTINUITY, SPATIAL DOMAIN

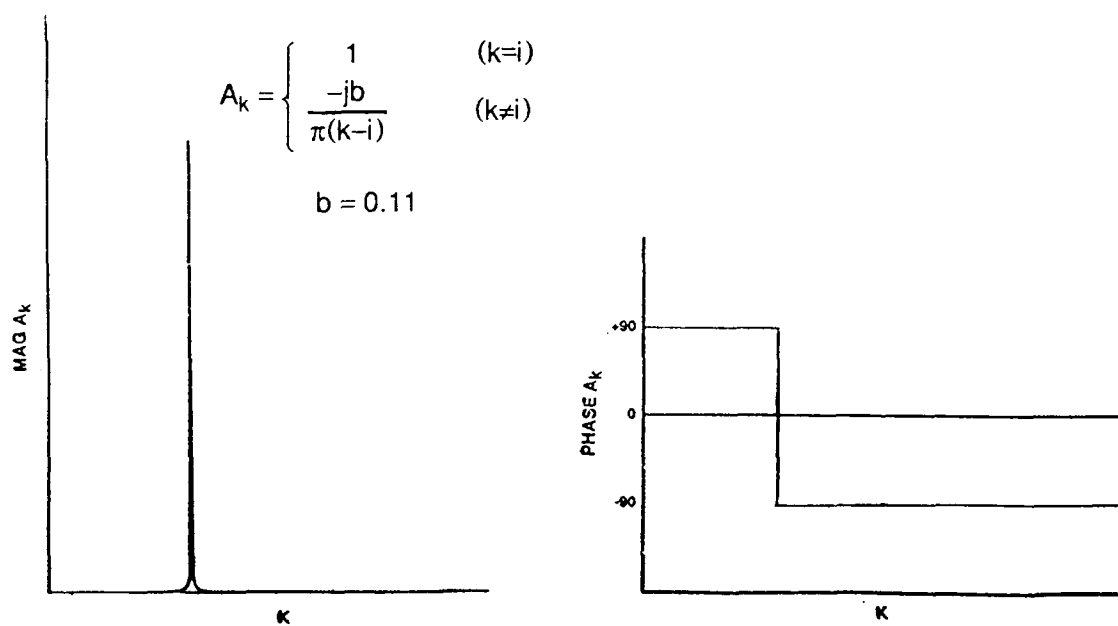


FIGURE 12. LINEARLY FREQUENCY-DEPENDENT DISCONTINUITY, SPATIAL DOMAIN

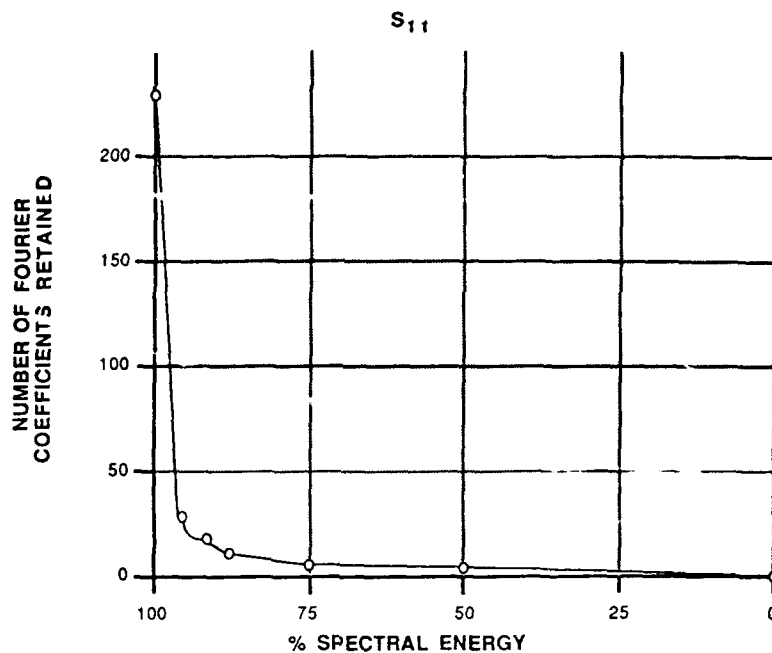


FIGURE 13. SPECTRAL ENERGY CONCENTRATION (256 PT. FFT)

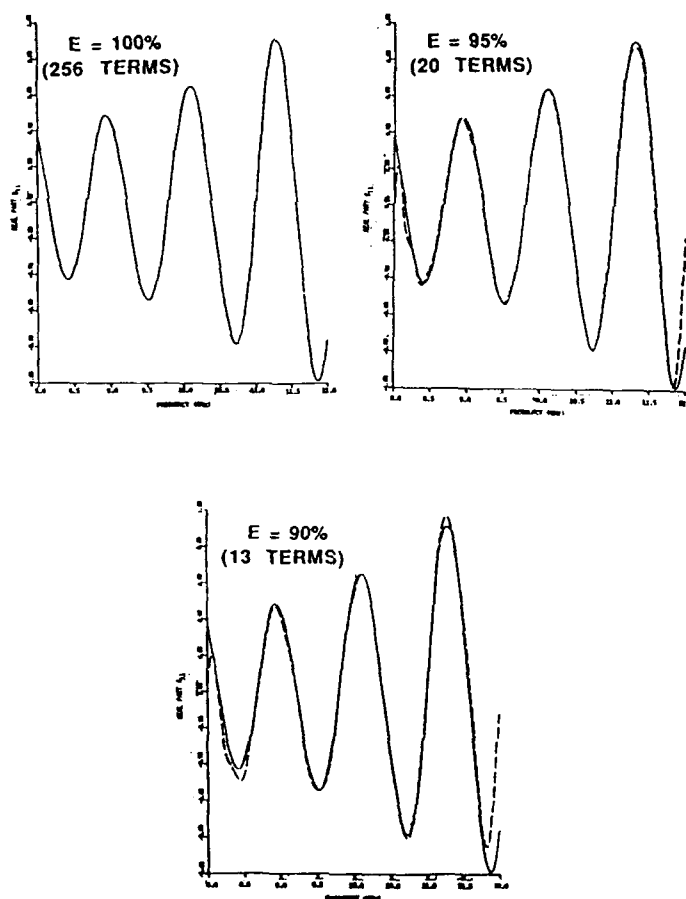


FIGURE 14. DATA REDUCTION IN THE SPATIAL DOMAIN, VARYING DEGREES OF SPECTRAL ENERGY RETAINED

clearly evident. Figure 14 illustrates the loss in modeling accuracy (in the frequency domain) for the real part of the input reflection coefficient for the two-stub tuner with 100 percent (256 terms), 95 percent (20 terms), and 90 percent (13 terms) of the total spectral energy retained. As one might expect, degradation in modeling accuracy is most evident at the inflection points, where low-pass filtering effects begin to emerge.

To review then, referring to Figure 4, data reduction in the spatial domain involves the application of both analog and digital signal processing techniques to the measured scattering coefficient data so as to reduce the data to a compact frequency-independent form (Fourier coefficients.) These coefficients (one set for each scattering parameter) are then passed to the next processing stage where the Fourier coefficients are parametrically modeled in terms of their physical variable dependencies.

### 2.3 Physical Variable Dependence Modeling

Figure 15 illustrates the overall procedure for the parametric modeling of the physical variable dependence for each of the retained Fourier coefficients.

For the case of the two-stub tuner (pictured in Figure 17) each Fourier coefficient is dependent upon two physical variables  $X_1$  and  $X_2$  (the "near" and "far" stub depths.) Figure 16 illustrates the magnitude and phase "surfaces" associated with the  $k = 6$  Fourier coefficient, corresponding to the spatial location of the "far"  $X_2$  stub. Note the strong exponential dependence of the coefficient magnitude on the  $X_2$  variable and the overall smoothness of the surface. In contrast, note the highly convoluted surface associated with the phase behavior of the  $k = 6$  Fourier coefficient. At first inspection, this behavior seems peculiar in light of the smooth magnitude characteristic. However, noting that phase ( $\theta$ ) is normally expressed MODULO ( $\theta, 2\pi$ ), we recognize that some of this ill-behavior may be due to "retraces" associated with the MODULO function. A typical "retrace" in one dimension is depicted as a dashed-line connecting the third and fourth data points in Figure 18a. Figure 18b illustrates the same data after application of a DEMODULO process by which a  $2\pi$  constant is added to all values subsequent to the fourth data point. Clearly, this modified characteristic is better suited to modeling. In fact, application of simple interpolation between the third and fourth data points in the MODULO form would result in highly erroneous results. A two-dimensional application of the DEMODULO process to the ill-behaved phase data of Figure 10 is illustrated in Figure 19b. Note the smoothness of the post-processed surface.

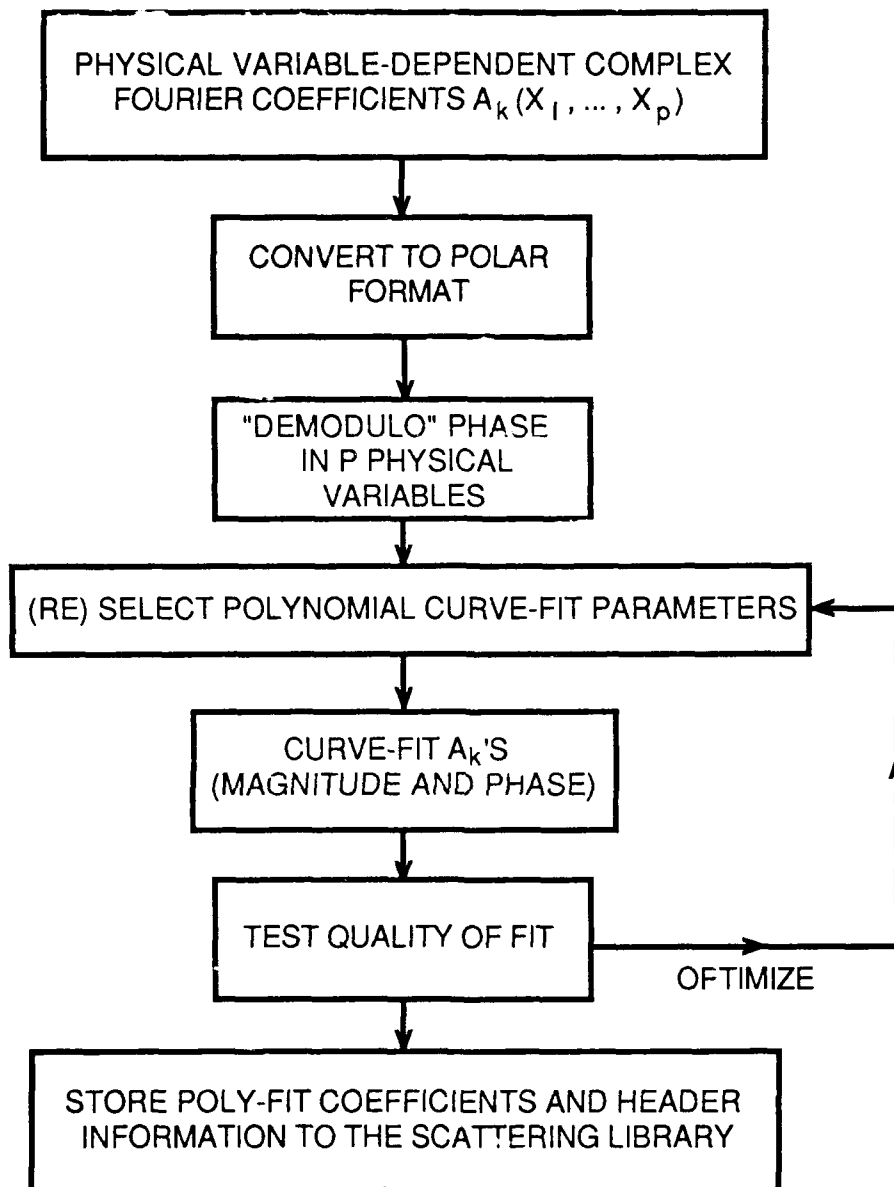


FIGURE 15. FLOW DIAGRAM, MODELING OF PHYSICAL VARIABLE DEPENDENCE OF FOURIER COEFFICIENTS

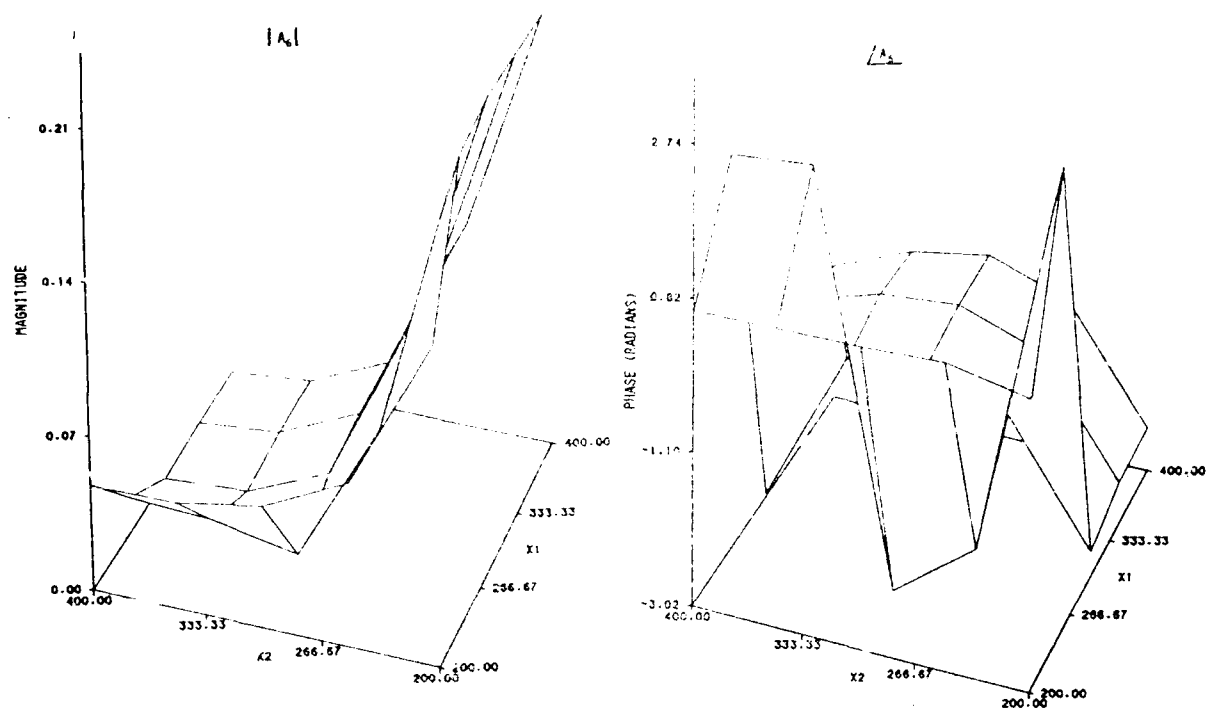


FIGURE 16. PHYSICAL VARIABLE DEPENDENCE OF FOURIER COEFFICIENT ( $A_6$ ) FOR TWIN-STUB DEVICE

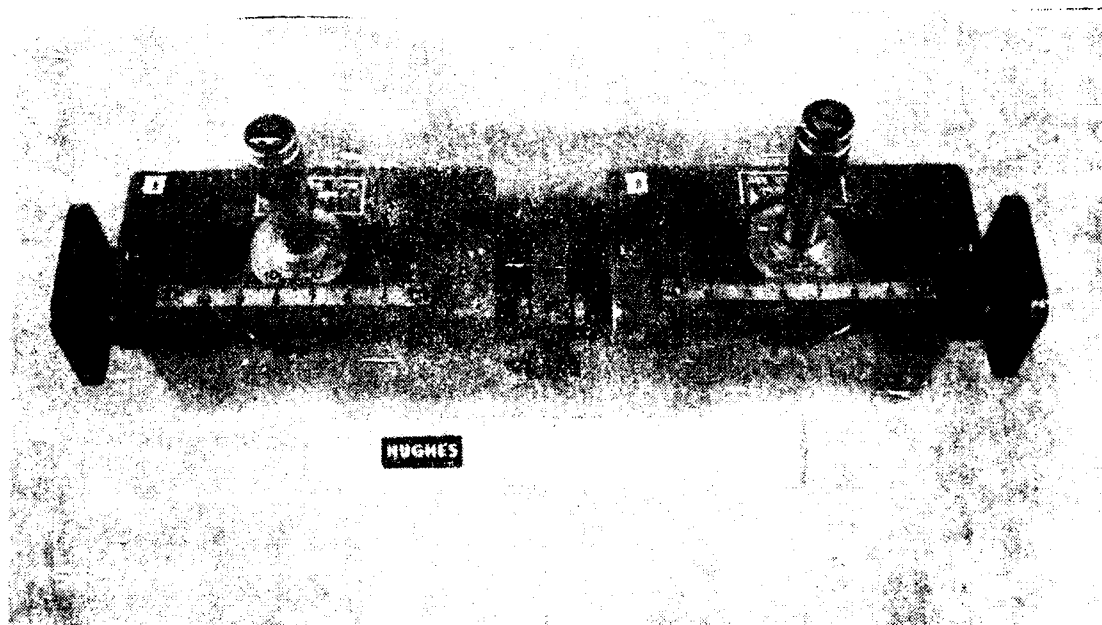


FIGURE 17. TWIN-STUB DEVICE

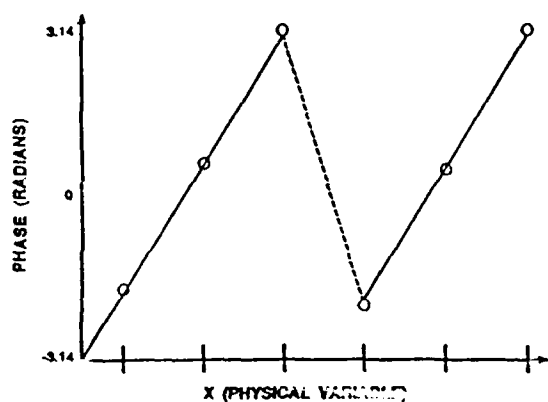


FIGURE 18a. PHASE DATA  
(1 DIMENSION),  
MODULO

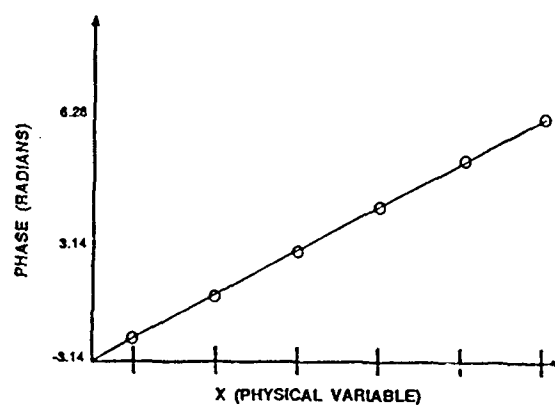


FIGURE 18b. PHASE DATA  
(1 DIMENSION),  
DEMODOLO

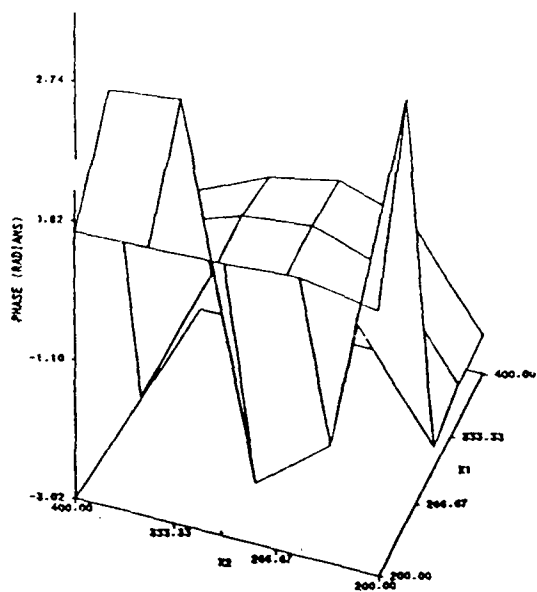


FIGURE 19a. PHASE DATA,  
MODULO  
(2 DIMENSIONS)

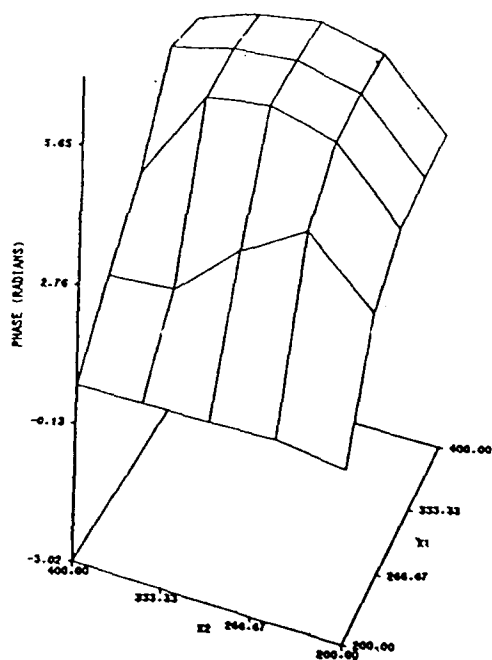


FIGURE 19b. PHASE DATA,  
DEMODOLO  
(2 DIMENSIONS)

Given smooth P-dimensional magnitude and phase (hyper-) surfaces for each Fourier coefficient, it is a straightforward process to apply a P-dimensional least-squares polynomial fit in order to parametrically model the physical dependencies. Weighting factors are applied to the least-squares fit of the phase (hyper-) surface in order to achieve local qualities-of-fit that are proportional to the Fourier coefficient magnitudes. The orders of these polynomials are variable (within the constraints of the number of measured physical variable permutations), and are adjusted in order to maximize modeling accuracy while minimizing the number of polynomial coefficients which must be ultimately stored.

#### 2.4 Formatting and Storage of the Scattering Library

With the parametric modeling process now complete, the polynomial coefficients for the magnitude and phase for each Fourier coefficient associated with each scattering parameter for a given device are formatted and stored in the scattering library. This condensed representation is accompanied by the device descriptors and parameters necessary in order to reconstitute the scattering parameters at specific frequencies for specific physical variable settings. Note that, besides "real" measured components, fictitious devices based on theoretical development can be synthesized, modeled, and stored as entries in the scattering parameter library.

### 3. The Circuit Analysis "Engine"

In a manner similar to other software packages, a schematic representation of an arbitrary interconnection of multi-port devices is based on a nodal format. Each internal node is common to exactly two devices with each external node common to only one. Interconnecting transmission line sections are specified as separate two-port devices. (Figure 25 illustrates this process.)

Expressions for each of the two opposite traveling waves at each node can be written in terms of the scattering coefficients and the incoming waves for each of the two adjacent devices. For M internal nodes, this results in 2M equations in 2M unknowns (internal wave coefficients.) We can therefore solve for all internal wave coefficients leaving only the scattering parameters for the N-port composite device defined by the N external nodes. This process is performed in practice through the construction of a square  $(2M+N) \times (2M+N)$  matrix.

which combines expressions for the outgoing waves at each of the external nodes in terms of the internal wave coefficients and the external incoming waves together with the homogeneous expressions for the internal wave coefficients in terms of the external incoming waves. This allows for the direct computation of the external scattering parameters by partitioning the matrix into four parts and solving for the external outgoing waves in terms of the external incoming waves through the application of simple matrix algebra and a single  $2M \times 2M$  inversion.

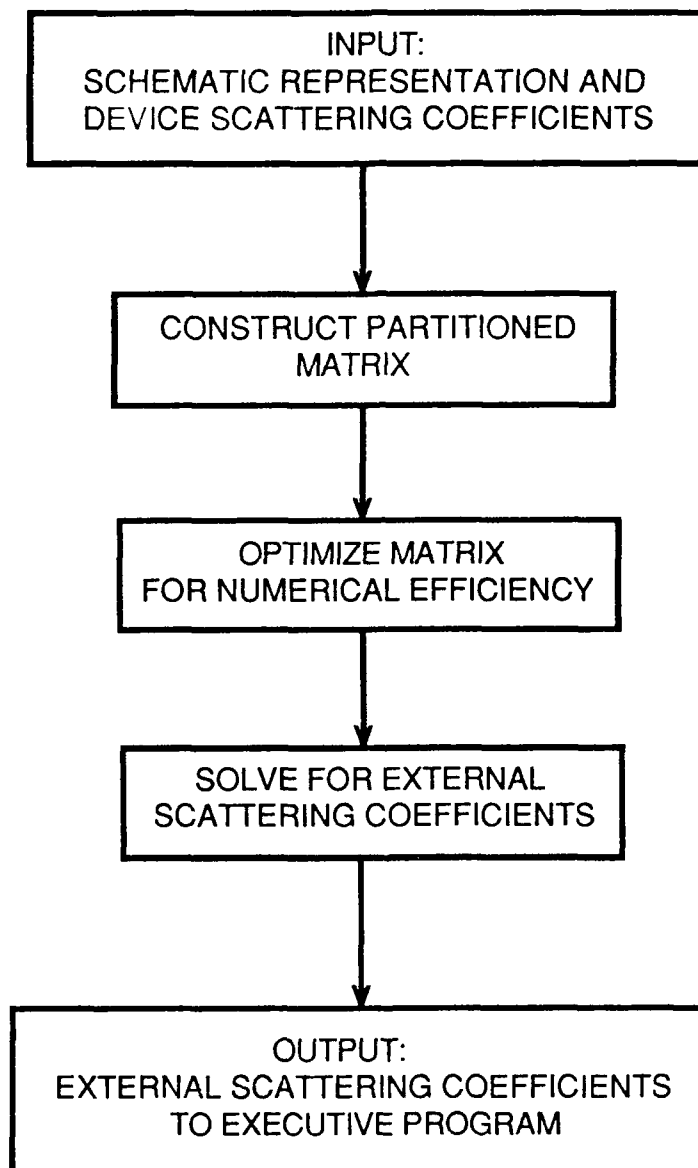
Figure 20 illustrates the process performed by the circuit analysis engine. Special care has been taken in optimizing the numerical efficiency of this routine because of its repetitive nature and its dominance in the overall execution time for the unified analysis package. Part of this optimization will ultimately include the exploitation of the sparse nature of the partitioned matrix, thereby allowing for the decimation of the large matrix equation into many smaller parts.

#### 4. The User-Specified Device Format

An obvious prerequisite to the analysis of a given circuit is the specification of the properties and interconnections of the constituent devices. This is accomplished via a user-specified input file in which the node connections and physical variable settings for each device are declared, one line per device. A typical input file line specifying a 3-port H-plane reactive tee is illustrated in Figure 21.

A device designation "DVDR0107" appears at the beginning of the line and serves as a "call number" for locating the previously stored and condensed scattering parameters for this device within the scattering library. The three integers "15", "11", and "32" specify the circuit nodes to which the first, second, and third ports of the device are attached. The following three real numbers "120", "3", and "2" describe the mean value, absolute tolerance, and standard deviation for the physical variable corresponding to the offset of the septum internal to the tee. The other two triplets dictate the same information for the variables associated with the septum and iris depths for the device. Alternatively, "global" variables can be specified in place of physical constants in order to expedite the adjustment of settings and tolerances for similar devices.





**FIGURE 20. FLOW DIAGRAM, CIRCUIT ANALYSIS ENGINE**

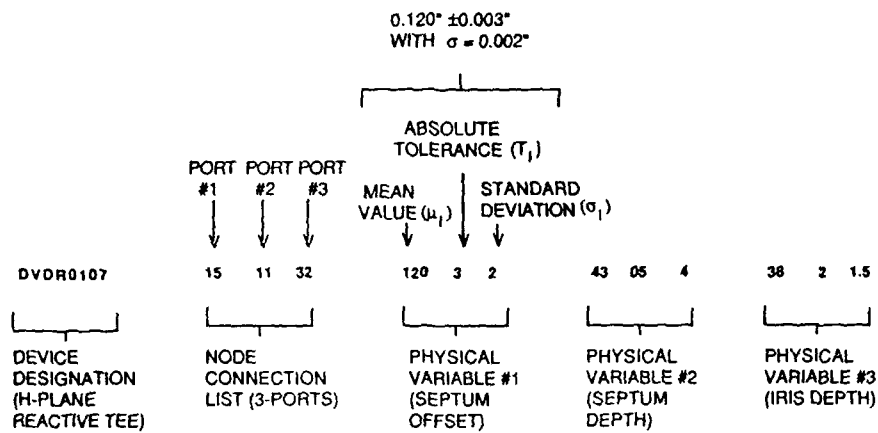


FIGURE 21. USER-SPECIFIED DEVICE FORMAT (1 CARD)

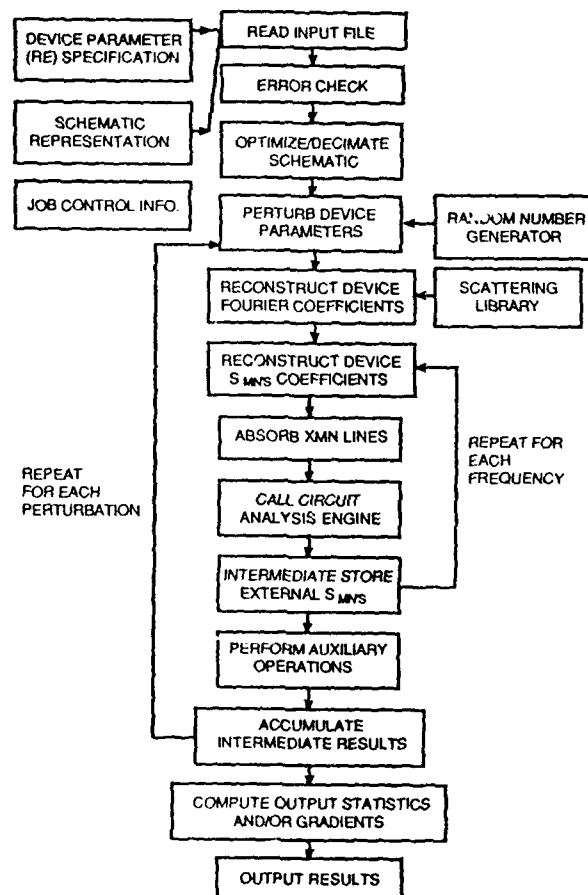


FIGURE 22. FLOW DIAGRAM, EXECUTIVE PROGRAM

The statistical information for each variable describes a probability distribution function, truncated at the tolerance extremes. These specifications are utilized when performing statistical studies of various composite circuit variables in terms of the tolerances of its constituent devices.

## 5.0 The Executive Program

The Executive Program is responsible for the overall management of the various unified analysis operations and is illustrated in flow diagram form in Figure 22. (Refer to Figure 1 for the location of the Executive Program within the overall unified analysis approach.) Note that most of the features discussed in this section are currently implemented in the executive program, while some remain in various stages of ongoing development.

Operation commences with the reading of the user-specified schematic and device descriptions embodied in the input file together with user-specified job control information dictating the desired functions and options to be performed. The input data set is checked for consistency in the schematic and device specifications. Verifications include: Is each node specified exactly once (external) or twice (internal)? Are the number of nodes in the node connection list equal to the number of ports for the device? Is the device model valid over the entire physical variable and frequency ranges of interest? Are all port interfaces continuous?

Following error checking, the user-specified schematic is optimized by identifying equivalent sections of the circuit and therefore eliminating redundant analysis operations. Additionally, the schematic is decimated into subsections which are analyzed separately in order to isolate statistically variable devices and to minimize matrix sizes, thereby enhancing numerical efficiency. Next, device variables are perturbed based on their individual probability distribution functions (statistical computations) or in specified differential increments (gradient computations.)

With all device variables now defined, the individual Fourier coefficients associated with each scattering parameter for each device are reconstructed through the expansion of the polynomials whose coefficients are stored in the scattering library. Note that these reconstructed Fourier coefficients have no frequency dependence and are therefore valid for the entire frequency bandwidth of interest.

The actual scattering parameters for each device are now reconstructed in the frequency domain through the application of an inverse FFT to the Fourier coefficients and the utilization of an interpolation formula as dictated by the Sampling Theorem. Interpolation begins with the lowest frequency and continues incrementally across the bandwidth of interest as specified by the user.

As another optimizing feature, simple transmission line lengths are "absorbed" into adjacent devices by altering the appropriate scattering parameter phase values in order to simulate the presence of the lines. This has the effect of reducing the number of required internal nodes by a factor of two and therefore improves computational efficiency.

Once fully optimized, the composite scattering parameters for the (sub-) circuit are computed via the circuit analysis engine and then temporarily stored. This process of scattering parameter reconstruction, transmission line absorption, and (sub-) circuit analysis is repeated for each frequency of interest.

It is at this point that any required auxiliary operations are performed on the computed external scattering parameter data. These operations include the calculation of related network parameters (VSWR, insertion loss and phase, transmission loss and phase, isolation) based on  $S_{mm}$  and  $S_{mn}$  coefficients; the computation of far-field antenna characteristics (patterns, gain, RMS sidelobe levels) based on aperture  $S_{mn}$  coefficients, lattice spacings, and element factors; and the prediction of "pre-aperture" RCS contributions based on aperture  $S_{mm}$  coefficients and lattice spacings. These characteristics are stored and accumulated for all required statistical/gradient perturbations of the physical variables.

Decimated (sub-) circuits are now reassembled and, based on the accumulated results for the various perturbation cases, statistical parameters (mean and standard deviations) and gradients are computed for network and antenna characteristics and then output in tabular and/or graphical form as requested by the user. Plots of mean values and standard deviation "windows" for individual characteristics as functions of frequency and/or angle are available. This allows for the informed adjustment of the mean values and tolerances of specific physical variables in order to meet specified network and antenna requirements with predictable levels of certainty. Gradient information is used for optimization of specific physical variables subject to user-specified weighting and penalty functions.

## 6. A Typical Application: Waveguide Corporate Feed Network

Figure 23 illustrates an eight-port Corporate Feed Subassembly comprised of six reactive H-plane power dividers, five H-plane bends, and seven E-plane bends, plus interconnecting waveguide sections.

A generic H-plane power divider was fabricated as pictured in Figure 24 and characterized in terms of its scattering parameters over a range of frequencies and physical variable combinations (septum offset, septum length, and iris depth.) Likewise, the two-port scattering parameters for the H-plane and E-plane waveguide bends were measured across a broad frequency bandwidth. Given the known physical variable settings for each of the six reactive H-plane power dividers comprising the feed network, the scattering parameters for each were reconstructed for all frequencies of interest. Figure 25 illustrates the node and device definitions for the network along with the (nonstatistical) schematic representation and the specification of interconnecting waveguide section lengths.

The unified analysis approach (in its developmental form) was applied to the network and Figures 26a and 26b illustrate the measured and predicted insertion losses between the input and each of the seven output ports across the entire bandwidth of interest. Note the faithful prediction of both the macroscopic and microscopic structure of the measured data. Similarly, plots of insertion phase and input VSWR show excellent correlation between predicted and measured results.

## 7. Progress-to-Date and Future Plans

As mentioned in the abstract and introduction, the development of the unified analysis approach is an ongoing effort. To date, we have proven the viability of our modeling and analysis techniques both in theory and in direct application via "proof-of-design" versions of the requisite software. Direct comparison between measured and predicted results for typical microwave subassemblies have yielded excellent correlations.

We continue to augment the scattering parameter library with the characterizations of common devices so as to expand the applicability of our analysis approach to a growing range of subassemblies and assemblies. The statistical capabilities of the analysis routine are presently under test as are several of the aforementioned optimization schemes for boosting numerical efficiency.

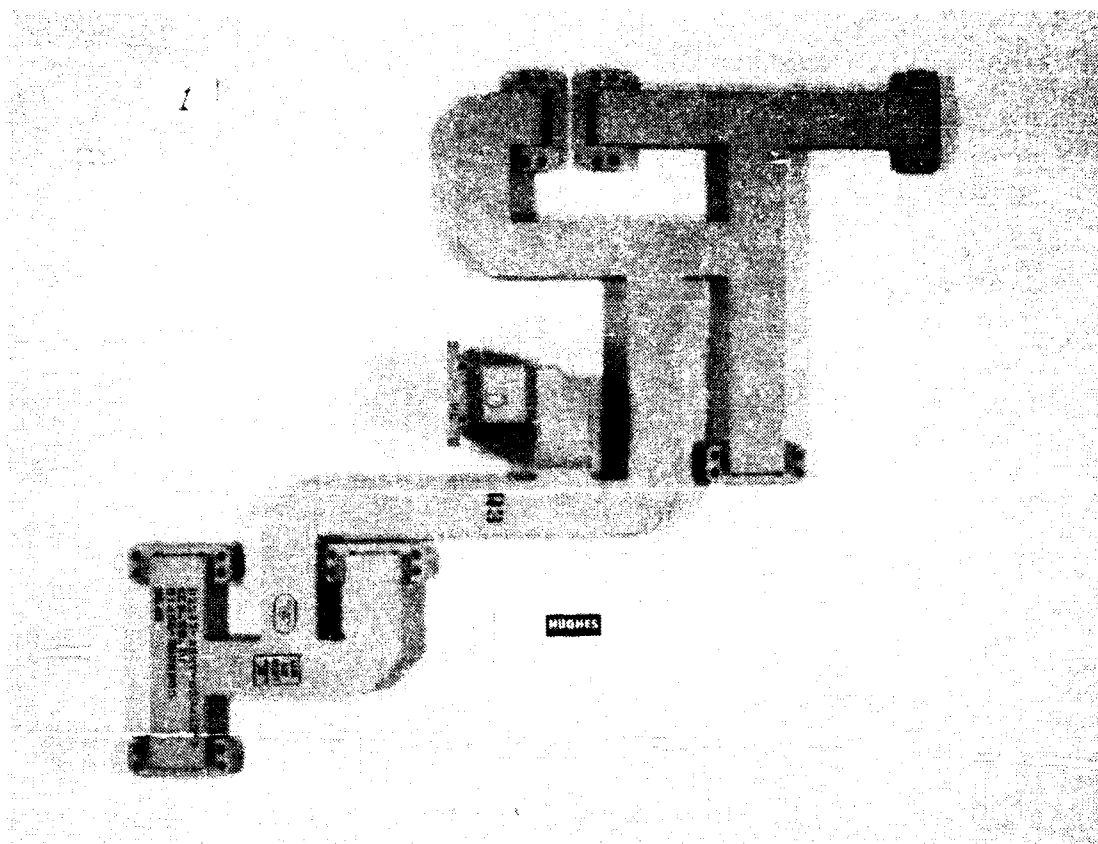


FIGURE 23. UPPER FEED ASSEMBLY

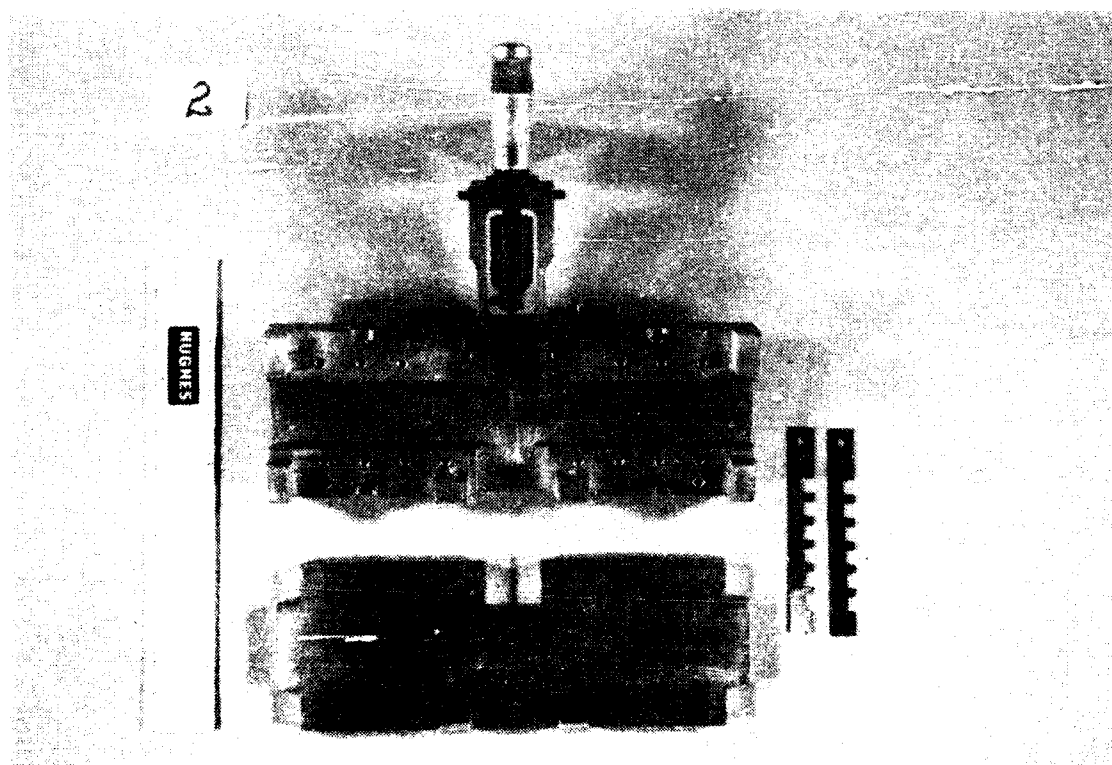


FIGURE 24. TEST FIXTURE, REACTIVE H-PLANE TEE

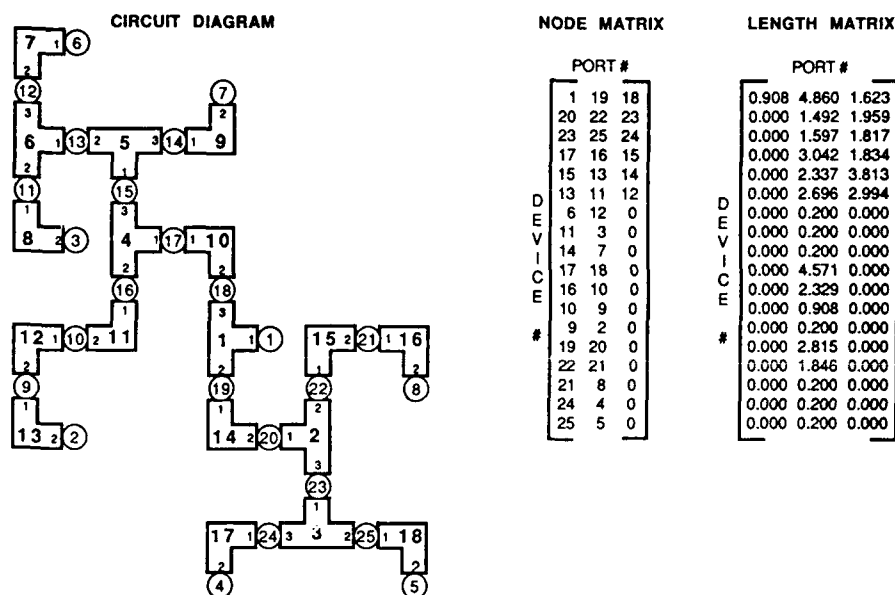


FIGURE 25. SCHEMATIC AND NODAL REPRESENTATION, UPPER FEED ASSEMBLY

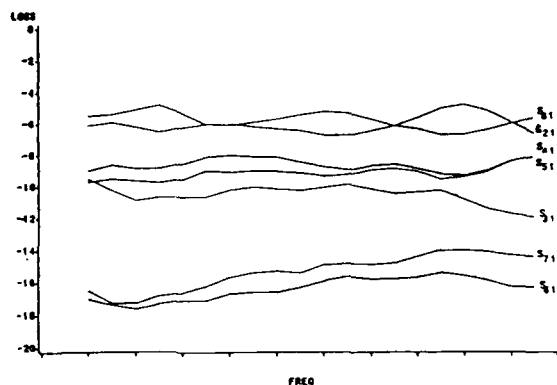


FIGURE 26a. UPPER FEED ASSEMBLY INSERTION-LOSS, MEASURED

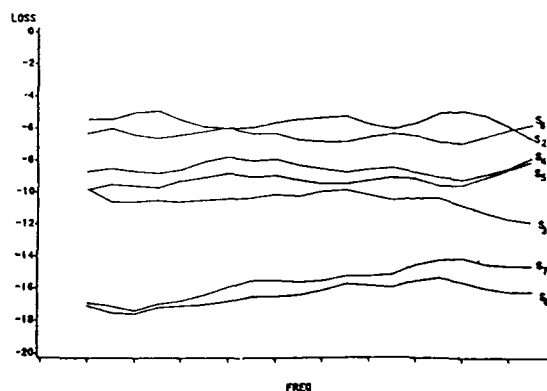


FIGURE 26b. UPPER FEED ASSEMBLY INSERTION-LOSS, PREDICTED

Auxiliary capabilities such as far-field patterns and RCS characterizations are not as yet available. However, implementation of these features is expected to be a straightforward process given the self ( $S_{mm}$ ) and coupling ( $S_{1n}$ ) scattering coefficients for the entire antenna assembly with the input ports and radiating elements expressed as external nodes.

As the scattering parameter library continues to grow and our analysis package becomes further refined, we will apply our unified approach to larger and larger portions of entire antenna systems, with the ultimate goal of modeling their complete behavior, replete from sum-port to aperture-plate, while realizing new levels of analysis accuracy and efficiency.

## 8. Acknowledgements

Special thanks to Mr. H. W. Byrne and Mr. D. F. Hall for their technical contributions, Mr. Y. S. Jeong for his empirical support, and to Ms. S. B. Van Cleve for overseeing the preparation of this manuscript.



SOLVING MAXWELL EQUATIONS BY MATRIX FORMULATION  
IN ANTENNA DESIGN AND APPLICATIONS

Feng Cheng Chang

Antenna Systems Laboratory  
TRW Electronic Systems Group  
Redondo Beach, California

ABSTRACT

The usual approach in solving Maxwell's equations with given current distribution is by means of finding the vector potential function due to the current source. This approach is generally very involved, for it contains vector differential operations in addition to the integration. In this article, useful formulas for directly finding electric and magnetic fields are derived, where the complicated vector differential operations are replaced by the easy vector algebraic operations. The resulting solutions are certainly exact with no approximation, and can be explicitly written in matrix formulation such that both the current source and the resulting fields may be conveniently expressed in terms of various coordinate systems. If the radiation fields in the near or far region are of primary interest, the formulation becomes simply the matrix multiplication, whenever the radiation vector is determined.

## SOLVING MAXWELL EQUATIONS BY MATRIX FORMULATION

### INTRODUCTION

In solving Maxwell's equations with a given current distribution, the usual approach [1-5] is to find the vector potential due to the current source. The desired solutions can then be determined by using vector differential operations upon the vector potential. A vector differential operation is an operation which contains the vector differential operator  $\nabla$ , such as gradient, divergence, curl, and Laplacian. By introducing the free-space Dyadic Green's function [1], one can bypass the vector potential function, and thereby establish a direct connection between the current source and the resulting electromagnetic fields. However, the solutions of Maxwell's equations are still quite involved, because of the vector differential operations in addition to the integration. In numerical computation, the evaluation is usually much easier for the integration than the differentiation, since integration can always be approximated using summations.

In this article useful formulas for finding electromagnetic fields are derived. These formulas replace the complicated vector differential operations with easy vector algebraic operations. A vector algebraic operation is an operation which contains only the dot product and cross product of vectors. The resulting field solutions are exact with no approximation. Furthermore, the field solutions can be explicitly written in matrix formulation so that both the current source and the resulting fields can be expressed in terms of various coordinate systems.

If the radiating fields [4,5], either in the near field (Fresnel region) or in the far field (Fraunhofer region), are of primary interest, the formulation can be greatly simplified. The electromagnetic fields are easily derived by simple matrix multiplication whenever the radiation vector [4] is calculated.

Several examples appearing in electromagnetic theory will be given to demonstrate the merit of the technique presented.

## FORMULATION

It is well-known [1-5] that the solutions of Maxwell equations in time harmonics form

$$\nabla \times \vec{E} = -j\omega\mu \vec{H} \quad (1a)$$

$$\nabla \times \vec{H} = j\omega\epsilon \vec{E} + \vec{J} \quad (1b)$$

can be written as

$$\vec{E}(\vec{r}) = -j\omega\eta \vec{G}_\nabla(\vec{r}) \vec{A}(\vec{r}) \quad (2a)$$

$$\vec{H}(\vec{r}) = -jk \vec{K}_\nabla(\vec{r}) \vec{A}(\vec{r}) \quad (2b)$$

where  $\vec{A}$  is called a vector potential, related to the given current distribution  $\vec{J}$  over a volume  $V$ ,

$$\vec{A}(\vec{r}) = \int_V g(|\vec{r} - \vec{r}'|) \vec{J}(\vec{r}') dv' \quad (3)$$

$$g(r) = \frac{e^{-jkr}}{4\pi r} \quad (4)$$

$$\eta = \sqrt{\mu/\epsilon} \quad k = \omega\sqrt{\mu\epsilon}$$

and  $\vec{G}_\nabla(\vec{r})$  and  $\vec{K}_\nabla(\vec{r})$  are vector differential operators, operating only upon the coordinates of the observation position  $\vec{r}$ ,

$$\vec{G}_\nabla(\vec{r}) = 1 + \frac{1}{k^2} \nabla \nabla \cdot \quad (5a)$$

$$\vec{K}_\nabla(\vec{r}) = \frac{1}{-jk} \nabla \times \quad (5b)$$

$\vec{G}_\nabla(\vec{r})g(|\vec{r} - \vec{r}'|)$  is the well-known free-space Dyadic Green's operator.

The electrical field and magnetic field may therefore be written as

$$\vec{E}(\vec{r}) = -jk\eta \int_V \vec{G}_\nabla(\vec{r}) g(|\vec{r} - \vec{r}'|) \vec{J}(\vec{r}') dv' \quad (6a)$$

$$\vec{H}(\vec{r}) = -jk \int_V \vec{K}_\nabla(\vec{r}) g(|\vec{r} - \vec{r}'|) \vec{J}(\vec{r}') dv' \quad (6b)$$

Evaluation of (2) or (6) is in general not very easy, since it involves both vector differential operations and integrations. It is shown in the Appendix that the complicated vector differential operations in (6) can be eliminated and replaced by easy vector algebraic operations. The results are

$$\vec{E}(\vec{r}) = -jk\eta \int_V g(R) \vec{G}(\vec{R}) \vec{J}(\vec{r}') dv' \quad (7a)$$

$$\vec{H}(\vec{r}) = -jk \int_V g(R) \vec{K}(\vec{R}) \vec{J}(\vec{r}') dv' \quad (7b)$$

where  $\vec{G}(\vec{R})$  and  $\vec{K}(\vec{R})$  are vector algebraic operators, containing only the dot product and cross product of vectors,

$$\vec{G}(\vec{R}) = \left(1 + \frac{1}{jkR} + \frac{1}{(jkR)^2}\right) (1 - \hat{R} \hat{R} \cdot) + \left(\frac{-2}{jkR} + \frac{-2}{(jkR)^2}\right) \hat{R} \hat{R} \cdot \quad (8a)$$

$$\vec{K}(\vec{R}) = \left(1 + \frac{1}{jkR}\right) \hat{R} \times \quad (8b)$$

and  $\vec{R}$  is a radial vector, independent of the coordinate system, directed along the line of sight from the source position  $\vec{r}'$  to the observation position  $\vec{r}$ , as illustrated in Figure 1(a).

$$\vec{R} = \vec{r} - \vec{r}', \quad R = |\vec{r} - \vec{r}'|, \quad \hat{R} = \frac{\vec{R}}{R} \quad (9)$$

Both (6) and (7) are exact solutions of Maxwell's equations (1), directly related to the current source. The evaluation by (7) is more manageable now compared to (6), since it involves only integration.

To demonstrate this, we may convert the vector expression into matrix expression by using the technique of matrix formulation of vector operations [6]. Equations (7) may then be written as,

$$(\vec{E}(\vec{r}^q))^P = -jk\eta \int_V g(R) \begin{bmatrix} P \\ T \end{bmatrix} \begin{bmatrix} S_R \\ \end{bmatrix} [\vec{G}(\vec{R})] \begin{bmatrix} S_R \\ T \end{bmatrix} \begin{bmatrix} P' \\ \end{bmatrix} (\vec{J}(\vec{r}', q'))^{P'} dv', q' \quad (10a)$$

$$(\vec{H}(\vec{r}^q))^P = -jk \int_V g(R) \begin{bmatrix} P \\ T \end{bmatrix} \begin{bmatrix} S_R \\ \end{bmatrix} [\vec{K}(\vec{R})] \begin{bmatrix} S_R \\ T \end{bmatrix} \begin{bmatrix} P' \\ \end{bmatrix} (\vec{J}(\vec{r}', q'))^{P'} dv', q' \quad (10b)$$

where the spherical coordinates  $s_R : (\theta_R, \phi_R, R)$  is defined such that  $\vec{R}$  is a radial vector from  $\vec{r}'$  to  $\vec{r}$ . And a vector, such as  $(\vec{E}(\vec{r}^q))^P$ , is a function of variables in the q-coordinates and has three components in the p-coordinates. Also a coordinate transformation matrix relating the u-coordinates to the v-coordinates is denoted by  $[VTU]$ , which can readily be found by the technique of a coordinate transformation flowchart [7]. As a practical application, the solutions  $\vec{E}(\vec{r})$  and  $\vec{H}(\vec{r})$  are usually expressed in the spherical coordinates  $s : (\theta, \phi, r)$ , and the source  $\vec{J}(\vec{r}')$  may be given in the Cartesian coordinates  $c' : (x', y', z')$ . Then (10) becomes,

$$(\vec{E}(\vec{r}^s))^S = -jk\eta \int_V g(R) \begin{bmatrix} S \\ T \end{bmatrix} \begin{bmatrix} S_R \\ \end{bmatrix} [\vec{G}(\vec{R})] \begin{bmatrix} S_R \\ T \end{bmatrix} \begin{bmatrix} C' \\ \end{bmatrix} (\vec{J}(\vec{r}', c'))^{C'} dv', c' \quad (11a)$$

$$(\vec{H}(\vec{r}^s))^S = -jk \int_V g(R) \begin{bmatrix} S \\ T \end{bmatrix} \begin{bmatrix} S_R \\ \end{bmatrix} [\vec{K}(\vec{R})] \begin{bmatrix} S_R \\ T \end{bmatrix} \begin{bmatrix} C' \\ \end{bmatrix} (\vec{J}(\vec{r}', c'))^{C'} dv', c' \quad (11b)$$

Equations (11) are then written explicitly in the matrix formulation,

$$\begin{pmatrix} E_{\theta}(\theta, \phi, r) \\ E_{\phi}(\theta, \phi, r) \\ E_r(\theta, \phi, r) \end{pmatrix} = -jk\eta \iiint_V \frac{e^{-jkR}}{4\pi R} \begin{pmatrix} \cos\theta\cos\phi & \cos\theta\sin\phi & -\sin\theta \\ -\sin\phi & \cos\phi & 0 \\ \sin\theta\cos\phi & \sin\theta\sin\phi & \cos\theta \end{pmatrix}$$

$$\begin{pmatrix} \cos\theta_R\cos\phi_R & -\sin\phi_R & \sin\theta_R\cos\phi_R \\ \cos\theta_R\sin\phi_R & \cos\phi_R & \sin\theta_R\sin\phi_R \\ -\sin\theta_R & 0 & \cos\theta_R \end{pmatrix} \begin{pmatrix} 1 + \frac{1}{jkR} + \frac{1}{(jkR)^2} & 0 & 0 \\ 0 & 1 + \frac{1}{jkR} + \frac{1}{(jkR)^2} & 0 \\ 0 & 0 & \frac{-2}{jkR} + \frac{-2}{(jkR)^2} \end{pmatrix}$$

$$\begin{pmatrix} \cos\theta_R\cos\phi_R & \cos\theta_R\sin\phi_R & -\sin\theta_R \\ -\sin\phi_R & \cos\phi_R & 0 \\ \sin\theta_R\cos\phi_R & \sin\theta_R\sin\phi_R & \cos\theta_R \end{pmatrix} \begin{pmatrix} J_{x'}(x', y', z') \\ J_{y'}(x', y', z') \\ J_{z'}(x', y', z') \end{pmatrix} dx' dy' dz' \quad (12a)$$

$$\begin{pmatrix} H_{\theta}(\theta, \phi, r) \\ H_{\phi}(\theta, \phi, r) \\ H_r(\theta, \phi, r) \end{pmatrix} = -jk \iiint_V \frac{e^{-jkR}}{4\pi R} \begin{pmatrix} \cos\theta\cos\phi & \cos\theta\sin\phi & -\sin\theta \\ -\sin\phi & \cos\phi & 0 \\ \sin\theta\cos\phi & \sin\theta\sin\phi & \cos\theta \end{pmatrix}$$

$$\begin{pmatrix} \cos\theta_R\cos\phi_R & -\sin\phi_R & \sin\theta_R\cos\phi_R \\ \cos\theta_R\sin\phi_R & \cos\phi_R & \sin\theta_R\sin\phi_R \\ -\sin\theta_R & 0 & \cos\theta_R \end{pmatrix} \begin{pmatrix} 0 & -1 - \frac{1}{jkR} & 0 \\ 1 + \frac{1}{jkR} & 0 & 0 \\ 0 & 0 & 0 \end{pmatrix}$$

$$\begin{pmatrix} \cos\theta_R\cos\phi_R & \cos\theta_R\sin\phi_R & -\sin\theta_R \\ -\sin\phi_R & \cos\phi_R & 0 \\ \sin\theta_R\cos\phi_R & \sin\theta_R\sin\phi_R & \cos\theta_R \end{pmatrix} \begin{pmatrix} J_{x'}(x', y', z') \\ J_{y'}(x', y', z') \\ J_{z'}(x', y', z') \end{pmatrix} dx' dy' dz' \quad (12b)$$

where

$$R = [ (r\sin\theta\cos\phi - x')^2 + (r\sin\theta\sin\phi - y')^2 + (r\cos\theta - z')^2 ]^{1/2}$$

$$\theta_R = \cos^{-1} [ (r\cos\theta - z') / R ]$$

$$\phi_R = \tan^{-1} [ (r\sin\theta\sin\phi - y') / (r\sin\theta\cos\phi - x') ]$$

The solutions of Maxwell's equations given by (12) are exact. The expression in matrix form is the most convenient for numerical computation.

In general, the radiating field [5], either in the near field or in the far field, is of primary interest. If  $r' \ll r \sim \lambda$ , then  $\vec{R} \rightarrow \vec{r}$ ,  $\hat{R} \rightarrow \hat{r}$ ,  $\theta_R \rightarrow \theta$ ,  $\phi_R \rightarrow \phi$ , and  $R \rightarrow r$  for the amplitude factor and  $R \rightarrow r - \hat{r} \cdot \vec{r}'$  for the phase factor. The vector potential given by (3) then becomes

$$\vec{A}(\vec{r}) = g(r) \vec{N}(\vec{r}), \quad r' \ll r \sim \lambda \quad (13a)$$

where  $\vec{N}(\vec{r})$  is called a radiation vector [4],

$$\vec{N}(\vec{r}) = \int_V \vec{J}(\vec{r}') e^{jk \hat{r} \cdot \vec{r}'} dv', \quad r' \ll r \sim \lambda \quad (13b)$$

Then from (2),

$$\vec{E}(\vec{r}) = -jk\eta \vec{G}_\nabla(\vec{r}) g(r) \vec{N}(\vec{r}) \quad (14a)$$

$$\vec{H}(\vec{r}) = -jk \vec{K}_\nabla(\vec{r}) g(r) \vec{N}(\vec{r}) \quad (14b)$$

and from (7),

$$\vec{E}(\vec{r}) = -jk\eta g(r) \vec{G}(\vec{r}) \vec{N}(\vec{r}) \quad (15a)$$

$$\vec{H}(\vec{r}) = -jk g(r) \vec{K}(\vec{r}) \vec{N}(\vec{r}) \quad (15b)$$

Both (14) and (15) should lead to the same results, when the vector potential  $\vec{A}(\vec{r})$  or the radiation vector  $\vec{N}(\vec{r})$  (for  $r' \ll r$ ) is computed. It is interesting to note that the solution by (14) is often extremely complicated, because it involves vector differential operations on a vector function  $\vec{A}(\vec{r}) = g(r)\vec{N}(\vec{r})$ . On the other hand, the solution by (15) is surprisingly simple and straightforward, because it involves only matrix multiplication. This can be seen clearly from the following matrix formulation:



$$\begin{pmatrix} E_{\theta}(\theta, \phi, r) \\ E_{\phi}(\theta, \phi, r) \\ E_r(\theta, \phi, r) \end{pmatrix} = -jkr \eta \frac{e^{-jkr}}{4\pi r} \begin{pmatrix} 1 + \frac{1}{jkr} + \frac{1}{(jkr)^2} & 0 & 0 \\ 0 & 1 + \frac{1}{jkr} + \frac{1}{(jkr)^2} & 0 \\ 0 & 0 & \frac{-2}{jkr} + \frac{-2}{(jkr)^2} \end{pmatrix} \begin{pmatrix} N_{\theta}(\theta, \phi, r) \\ N_{\phi}(\theta, \phi, r) \\ N_r(\theta, \phi, r) \end{pmatrix} \quad (16a)$$

$$\begin{pmatrix} H_{\theta}(\theta, \phi, r) \\ H_{\phi}(\theta, \phi, r) \\ H_r(\theta, \phi, r) \end{pmatrix} = -jk \frac{e^{-jkr}}{4\pi r} \begin{pmatrix} 0 & -1 - \frac{1}{jkr} & 0 \\ 1 + \frac{1}{jkr} & 0 & 0 \\ 0 & 0 & 0 \end{pmatrix} \begin{pmatrix} N_{\theta}(\theta, \phi, r) \\ N_{\phi}(\theta, \phi, r) \\ N_r(\theta, \phi, r) \end{pmatrix} \quad (16b)$$

Specializing for the far field, where  $r \gg \lambda$ ,

$$\begin{pmatrix} E_{\theta}(\theta, \phi, r) \\ E_{\phi}(\theta, \phi, r) \\ E_r(\theta, \phi, r) \end{pmatrix} = -jkr \eta \frac{e^{-jkr}}{4\pi r} \begin{pmatrix} 1 & 0 & 0 \\ 0 & 1 & 0 \\ 0 & 0 & 0 \end{pmatrix} \begin{pmatrix} N_{\theta}(\theta, \phi, r) \\ N_{\phi}(\theta, \phi, r) \\ N_r(\theta, \phi, r) \end{pmatrix} \quad (17a)$$

$$\begin{pmatrix} H_{\theta}(\theta, \phi, r) \\ H_{\phi}(\theta, \phi, r) \\ H_r(\theta, \phi, r) \end{pmatrix} = -jk \frac{e^{-jkr}}{4\pi r} \begin{pmatrix} 0 & -1 & 0 \\ 1 & 0 & 0 \\ 0 & 0 & 0 \end{pmatrix} \begin{pmatrix} N_{\theta}(\theta, \phi, r) \\ N_{\phi}(\theta, \phi, r) \\ N_r(\theta, \phi, r) \end{pmatrix} \quad (17b)$$

From (16) or (17) we see that for  $r' \ll r$ , the desired solutions  $\vec{E}(\vec{r})$  and  $\vec{H}(\vec{r})$  of Maxwell's equations can be easily determined whenever the radiation vector  $\vec{N}(\vec{r})$  has been computed.

To compute the radiation vector  $\vec{N}(\vec{r})$  in general cases, we assume that the coordinate systems of the source  $\vec{r}'$  and the field  $\vec{r}$  are not coincident, but are related through both origin translation along the offset vector  $\vec{r}_b(x_b, y_b, z_b)$  and three rotations via Euler angles  $(\phi_w, \theta_w, \psi_w)$  as depicted in Figure 1(b). The desired radiation vector may be obtained by either of the following forms:

$$(\vec{N}(\vec{r}^s))^s = \int_V [^sT^C] (\vec{J}(\vec{r}^C))^C \exp jk(\hat{r}^s)^C ((\vec{r}^C)_b^C + [^CT^C] (\vec{r},^C)^C) dv,^C \quad (18a)$$

$$(\vec{N}(\vec{r}^s))^s = \int_V [^sT^{d'}] (\vec{J}(\vec{r}^{d'}))^d \exp jk(\hat{r}^s)^C ((\vec{r}^C)_b^C + [^CT^{d'}] (\vec{r},^d)^d) dv,^d \quad (18b)$$

$$(\vec{N}(\vec{r}^s))^s = \int_V [^sT^C] (\vec{J}(\vec{r}^{d'}))^C \exp jk(\hat{r}^s)^C ((\vec{r}^C)_b^C + [^CT^{d'}] (\vec{r},^d)^d) dv,^d \quad (18c)$$

$$(\vec{N}(\vec{r}^s))^s = \int_V [^sT^{d'}] (\vec{J}(\vec{r}^C))^d \exp jk(\hat{r}^s)^C ((\vec{r}^C)_b^C + [^CT^C] (\vec{r},^C)^C) dv,^C \quad (18d)$$

It is more useful when we write (18) explicitly in matrix form,

$$\begin{pmatrix} N_\theta(\theta, \phi, r) \\ N_\phi(\theta, \phi, r) \\ N_r(\theta, \phi, r) \end{pmatrix} = e^{jk\rho_b} \begin{pmatrix} \cos\theta\cos\phi & \cos\theta\sin\phi & -\sin\theta \\ -\sin\phi & \cos\phi & 0 \\ \sin\theta\cos\phi & \sin\theta\sin\phi & \cos\theta \end{pmatrix}$$

$$\cdot \begin{pmatrix} \cos\theta_w \cos\phi_w \cos\psi_w & -\sin\theta_w \sin\psi_w & -\cos\theta_w \cos\phi_w \sin\psi_w & -\sin\theta_w \cos\psi_w & \sin\theta_w \cos\phi_w \\ \cos\theta_w \sin\phi_w \cos\psi_w & +\cos\phi_w \sin\psi_w & -\cos\theta_w \sin\phi_w \sin\psi_w & +\cos\phi_w \cos\psi_w & \sin\theta_w \sin\phi_w \\ -\sin\theta_w \cos\psi_w & & \sin\theta_w \sin\psi_w & & \cos\theta_w \end{pmatrix}$$

$$\text{either } x \iiint_V \begin{pmatrix} J_{x'}(x', y', z') \\ J_{y'}(x', y', z') \\ J_{z'}(x', y', z') \end{pmatrix} e^{jk\rho^C} dx' dy' dz' \quad (19a)$$

$$\text{or } x \iiint_V \begin{pmatrix} \cos\phi' & -\sin\phi' & 0 \\ \sin\phi' & \cos\phi' & 0 \\ 0 & 0 & 1 \end{pmatrix} \begin{pmatrix} J_{\rho'}(\rho', \phi', z') \\ J_{\phi'}(\rho', \phi', z') \\ J_{z'}(\rho', \phi', z') \end{pmatrix} e^{jk\rho^{d'}} \rho' d\rho' d\phi' dz' \quad (19b)$$

$$\text{or } x \iiint_V \begin{pmatrix} J_{x'}(\rho', \phi', z') \\ J_{y'}(\rho', \phi', z') \\ J_{z'}(\rho', \phi', z') \end{pmatrix} e^{jk\rho^{d'}} \rho' d\rho' d\phi' dz' \quad (19c)$$

$$\text{or } x \iiint_V \begin{pmatrix} \cos\phi' & -\sin\phi' & 0 \\ \sin\phi' & \cos\phi' & 0 \\ 0 & 0 & 1 \end{pmatrix} \begin{pmatrix} J_{\rho'}(x', y', z') \\ J_{\phi'}(x', y', z') \\ J_{z'}(x', y', z') \end{pmatrix} e^{jk\rho^C} dx' dy' dz' \quad (19d)$$

where

$$p_b = x_b \sin \theta \cos \phi + y_b \sin \theta \sin \phi + z_b \cos \theta$$

$$\begin{aligned} p^{c'} = & x' [(\sin \theta \cos \theta_w \cos(\phi - \phi_w) - \cos \theta \sin \theta_w) \cos \psi_w + \sin \theta \sin(\phi - \phi_w) \sin \psi_w] \\ & + y' [-(\sin \theta \cos \theta_w \cos(\phi - \phi_w) - \cos \theta \sin \theta_w) \sin \psi_w + \sin \theta \sin(\phi - \phi_w) \cos \psi_w] \\ & + z' [\sin \theta \sin \theta_w \cos(\phi - \phi_w) + \cos \theta \cos \theta_w] \end{aligned}$$

$$\begin{aligned} p^{d'} = & p' [(\sin \theta \cos \theta_w \cos(\phi - \phi_w) - \cos \theta \sin \theta_w) \cos(\psi_w + \phi') \\ & + \sin \theta \sin(\phi - \phi_w) \sin(\psi_w + \phi')] + z' [\sin \theta \sin \theta_w \cos(\phi - \phi_w) + \cos \theta \cos \theta_w] \end{aligned}$$

and

$$p' = \sqrt{x'^2 + y'^2}, \quad \phi' = \tan^{-1}(y'/x'),$$

$$x' = p' \cos \phi', \quad y' = p' \sin \phi'.$$

In the case that there is no origin translation and no axis rotations, such as depicted in Figure 1(a), then (19) become simply,

$$\begin{pmatrix} N_{\theta}(\theta, \phi, r) \\ N_{\phi}(\theta, \phi, r) \\ N_r(\theta, \phi, r) \end{pmatrix} = \begin{pmatrix} \cos\theta\cos\phi & \cos\theta\sin\phi & -\sin\theta \\ -\sin\phi & \cos\phi & 0 \\ \sin\theta\cos\phi & \sin\theta\sin\phi & \cos\theta \end{pmatrix} \iiint_V \begin{pmatrix} J_x(x', y', z') \\ J_y(x', y', z') \\ J_z(x', y', z') \end{pmatrix} e^{jk[x'\sin\theta\cos\phi + y'\sin\theta\sin\phi + z'\cos\theta]} dx' dy' dz' \quad (20a)$$

$$= \iiint_V \begin{pmatrix} \cos\theta\cos(\phi-\phi') & \cos\theta\sin(\phi-\phi') & -\sin\theta \\ -\sin(\phi-\phi') & \cos(\phi-\phi') & 0 \\ \sin\theta\cos(\phi-\phi') & \sin\theta\sin(\phi-\phi') & \cos\theta \end{pmatrix} \begin{pmatrix} J_{\rho}(\rho', \phi', z') \\ J_{\phi}(\rho', \phi', z') \\ J_z(\rho', \phi', z') \end{pmatrix} e^{jk[\rho'\sin\theta\cos(\phi-\phi') + z'\cos\theta]} \rho' d\rho' d\phi' dz' \quad (20b)$$

$$= \begin{pmatrix} \cos\theta\cos\phi & \cos\theta\sin\phi & -\sin\theta \\ -\sin\phi & \cos\phi & 0 \\ \sin\theta\cos\phi & \sin\theta\sin\phi & \cos\theta \end{pmatrix} \iiint_V \begin{pmatrix} J_x(\rho', \phi', z') \\ J_y(\rho', \phi', z') \\ J_z(\rho', \phi', z') \end{pmatrix} e^{jk[\rho'\sin\theta\cos(\phi-\phi') + z'\cos\theta]} \rho' d\rho' d\phi' dz' \quad (20c)$$

$$= \iiint_V \begin{pmatrix} \cos\theta\cos(\phi-\phi') & \cos\theta\sin(\phi-\phi') & -\sin\theta \\ -\sin(\phi-\phi') & \cos(\phi-\phi') & 0 \\ \sin\theta\cos(\phi-\phi') & \sin\theta\sin(\phi-\phi') & \cos\theta \end{pmatrix} \begin{pmatrix} J_{\rho}(x', y', z') \\ J_{\phi}(x', y', z') \\ J_z(x', y', z') \end{pmatrix} e^{jk[x'\sin\theta\cos\phi + y'\sin\theta\sin\phi + z'\cos\theta]} dx' dy' dz' \quad (20d)$$

It is often quite convenient to include both an electric source  $\vec{J}$  and magnetic source  $\vec{M}$  in Maxwell's equations [1-5]:

$$\nabla \times \vec{H} = j\omega\epsilon\vec{E} + \vec{J} \quad (20a)$$

$$-\nabla \times \vec{E} = j\omega\mu\vec{H} + \vec{M} \quad (20b)$$

The solutions are then the superposition of the fields due to both current sources,

$$\vec{E}(\vec{r}) = -jk\eta \vec{G}_v(\vec{r}) \vec{A}(\vec{r}) + jk \vec{K}_v(\vec{r}) \vec{F}(\vec{r}) \quad (21a)$$

$$\vec{H}(\vec{r}) = -jk/\eta \vec{G}_v(\vec{r}) \vec{F}(\vec{r}) - jk \vec{K}_v(\vec{r}) \vec{A}(\vec{r}) \quad (21b)$$

where

$$\vec{A}(\vec{r}) = \int_V g(|\vec{r} - \vec{r}'|) \vec{J}(\vec{r}') dv' \quad (22a)$$

$$\vec{F}(\vec{r}) = \int_V g(|\vec{r} - \vec{r}'|) \vec{M}(\vec{r}') dv' \quad (22b)$$

are electric and magnetic vector potentials.

If the radiation field is of primary interest ( $r' \ll r \sim \lambda$ ), then the solutions can be simplified to

$$\vec{E}(\vec{r}) = -jk g(r) [ \eta \vec{G}(\vec{r}) \vec{N}(\vec{r}) - \vec{K}(\vec{r}) \vec{L}(\vec{r}) ] \quad (23a)$$

$$\vec{H}(\vec{r}) = -jk g(r) [ \frac{1}{\eta} \vec{G}(\vec{r}) \vec{L}(\vec{r}) + \vec{K}(\vec{r}) \vec{N}(\vec{r}) ] \quad (23b)$$

where

$$\vec{N}(\vec{r}) = \int_V \vec{J}(\vec{r}') e^{jk\hat{r} \cdot \vec{r}'} dv', \quad r' \ll r \quad (24a)$$

$$\vec{L}(\vec{r}) = \int_V \vec{M}(\vec{r}') e^{jk\hat{r} \cdot \vec{r}'} dv', \quad r' \ll r \quad (24b)$$

are radiation vectors due to the respective current sources.

As before (23) contains only vector algebraic operations which are convenient for numerical computations. We therefore have the formal solution for any problem consisting of electric and magnetic currents in an unbounded homogeneous region. These formulas include, by implication, sheets and filaments of the electric and magnetic currents.

### EXAMPLES

Several examples will be presented to demonstrate the merit of the technique derived.

#### 1. Hertzian dipole antenna

The current distribution of an electric dipole may be expressed as

$$\begin{pmatrix} J_{x'} \\ J_{y'} \\ J_{z'} \end{pmatrix} = \begin{pmatrix} 0 \\ 0 \\ 1 \end{pmatrix} \delta(x') \delta(y') I(z'), \quad -\frac{l}{2} \leq z' \leq \frac{l}{2}$$

If  $I(z') = I_0$  and  $l \ll \lambda$ , then from (20a),

$$\begin{pmatrix} N_\theta \\ N_\phi \\ N_r \end{pmatrix} = \begin{pmatrix} -\sin\theta \\ 0 \\ \cos\theta \end{pmatrix} I_0 l \operatorname{sinc}(k \frac{l}{2} \cos\theta) \xrightarrow{l \ll \lambda} \begin{pmatrix} -\sin\theta \\ 0 \\ \cos\theta \end{pmatrix} I_0 l$$

The corresponding radiating fields are therefore obtained from (16)

$$\begin{pmatrix} E_{\theta} \\ E_{\phi} \\ E_r \end{pmatrix} = -jkr \frac{e^{-jkr}}{4\pi r} I_0 l \begin{pmatrix} -(1 + \frac{1}{jkr} + \frac{1}{(jkr)^2}) \sin\theta \\ 0 \\ (\frac{-2}{jkr} + \frac{-2}{(jkr)^2}) \cos\theta \end{pmatrix}$$

$$\begin{pmatrix} H_{\theta} \\ H_{\phi} \\ H_r \end{pmatrix} = -jk \frac{e^{-jkr}}{4\pi r} I_0 l \begin{pmatrix} 0 \\ -(1 + \frac{1}{jkr}) \sin\theta \\ 0 \end{pmatrix}$$

## 2. Dipole above the ground plane

A horizontal dipole is situated above an infinite conducting plane. Employing the image method, the location  $(x_B, y_B, z_B)$  and orientation  $(\phi_w, \theta_w, \psi_w)$  are, respectively,  $(0, 0, h)$  and  $(0^\circ, 90^\circ, 0^\circ)$  for the real element and  $(0, 0, -h)$  and  $(0^\circ, -90^\circ, 0^\circ)$  for the image element. The current distribution of both elements is assumed to be that of the electric dipole in the previous example. By superposition and from (19a), we have

$$\begin{pmatrix} N_{\theta} \\ N_{\phi} \\ N_r \end{pmatrix} = \begin{pmatrix} jkh \cos\theta & -jkh \cos\theta \\ e & -e \end{pmatrix} \begin{pmatrix} \cos\theta \cos\phi \\ -\sin\phi \\ \sin\theta \cos\phi \end{pmatrix} I_0 l$$

The radiating fields are then followed from (16) or (17).

### 3. Circular loop current

The current distribution of a circular current loop of radius  $a$  may be expressed as

$$\begin{pmatrix} J_{\rho'} \\ J_{\phi'} \\ J_{z'} \end{pmatrix} = \begin{pmatrix} 0 \\ 1 \\ 0 \end{pmatrix} \delta(\rho' - a) \delta(z') I(\phi'), \quad 0 \leq \phi' \leq 2\pi$$

Then from (20b),

$$\begin{pmatrix} N_{\theta} \\ N_{\phi} \\ N_r \end{pmatrix} = \int_0^{2\pi} \begin{pmatrix} \cos\theta \sin(\phi - \phi') \\ \cos(\phi - \phi') \\ \sin\theta \sin(\phi - \phi') \end{pmatrix} I(\phi') a e^{jka \sin\theta \cos(\phi - \phi')} d\phi'$$

If  $I(\phi') = I_0$  and  $a \ll \lambda$ ,

$$\begin{pmatrix} N_{\theta} \\ N_{\phi} \\ N_r \end{pmatrix} = \begin{pmatrix} 0 \\ 1 \\ 0 \end{pmatrix} I_0 a j 2\pi J_1(ka \sin\theta) \xrightarrow{a \ll \lambda} jk I_0 \pi a^2 \begin{pmatrix} 0 \\ \sin\theta \\ 0 \end{pmatrix}$$

Specializing for the far field, where  $r \gg \lambda$ , the radiating fields are then from (17),

$$\begin{pmatrix} E_{\theta} \\ E_{\phi} \\ E_r \end{pmatrix} = -jk\eta \frac{e^{-jkr}}{4\pi r} jk I_0 \pi a^2 \begin{pmatrix} 0 \\ \sin\theta \\ 0 \end{pmatrix}$$

$$\begin{pmatrix} H_{\theta} \\ H_{\phi} \\ H_r \end{pmatrix} = -jk \frac{e^{-jkr}}{4\pi r} jk I_0 \pi a^2 \begin{pmatrix} -\sin\theta \\ 0 \\ 0 \end{pmatrix}$$



#### 4. Helix antenna

The current distribution of a helix antenna as shown in Fig. 2.11 of [3] may be expressed as

$$\begin{pmatrix} J_{\rho'} \\ J_{\phi'} \\ J_{z'} \end{pmatrix} = \begin{pmatrix} 0 \\ 1 \\ b/a \end{pmatrix} \delta(\rho' - a) \delta(z' - b\phi') I(\phi'), \quad 0 \leq \phi' \leq 2\pi N$$

From (20b)

$$\begin{pmatrix} N_{\theta} \\ N_{\phi} \\ N_r \end{pmatrix} = \int_0^{2\pi N} \begin{pmatrix} a \cos \theta \sin(\phi - \phi') - b \sin \theta \\ a \cos(\phi - \phi') \\ a \sin \theta \sin(\phi - \phi') + b \cos \theta \end{pmatrix} I(\phi') e^{jk[a \sin \theta \cos(\phi - \phi') + b \phi' \cos \theta]} d\phi'$$

For

$$I(\phi') = I_0 e^{-(\alpha + j\beta) \sqrt{a^2 + b^2} \phi'}$$

we have

$$\begin{pmatrix} N_{\theta} \\ N_{\phi} \\ N_r \end{pmatrix} = \left( \sum_{n=0}^{N-1} e^{-j2\pi n h(\theta)} \right) \int_0^{2\pi} \begin{pmatrix} a \cos \theta \sin(\phi - \phi') - b \sin \theta \\ a \cos(\phi - \phi') \\ a \sin \theta \sin(\phi - \phi') + b \cos \theta \end{pmatrix} I_0 e^{-jh(\theta)\phi'} e^{jk a \sin \theta \cos(\phi - \phi')} d\phi'$$

where

$$h(\theta) = (\beta - j\alpha) \sqrt{a^2 + b^2} - k b \cos \theta$$

These are the same results as Eq. 2.50 -51 of [3].

## 5. Circular aperture radiator

The exact solutions of Maxwell's equations with given magnetic current distribution are similar to those of (10). Let the fields be in the Cartesian coordinates, and the source be a function of variables in the cylindrical coordinates with three components in the Cartesian coordinates. Then the desired solutions in the matrix formulation are

$$\begin{aligned} (\vec{E}(\vec{r}^C))^C &= +jk \int_V g(R) \begin{bmatrix} C & T & S_R \end{bmatrix} [\vec{K}(\vec{R})] \begin{bmatrix} S_R & S_{RT} & C' \end{bmatrix} (\vec{M}(\vec{r}', d'))^{C'} dv' d' \\ (\vec{H}(\vec{r}^C))^C &= -j \frac{k}{\eta} \int_V g(R) \begin{bmatrix} C & T & S_R \end{bmatrix} [\vec{G}(\vec{R})] \begin{bmatrix} S_R & S_{RT} & C' \end{bmatrix} (\vec{M}(\vec{r}', d'))^{C'} dv' d' \end{aligned}$$

Explicitly,

$$\begin{pmatrix} H_x(x, y, z) \\ H_y(x, y, z) \\ H_z(x, y, z) \end{pmatrix} = -j \frac{k}{\eta} \int_0^\infty \int_0^{2\pi} \int_{-\infty}^\infty \frac{e^{-jkR}}{4\pi R}$$

$$\begin{pmatrix} \cos\theta_R \cos\phi_R & -\sin\phi_R & \sin\theta_R \cos\phi_R \\ \cos\theta_R \sin\phi_R & \cos\phi_R & \sin\theta_R \sin\phi_R \\ -\sin\theta_R & 0 & \cos\theta_R \end{pmatrix} \begin{pmatrix} 1 + \frac{1}{jkR} + \frac{1}{(jkR)^2} & 0 & 0 \\ 0 & 1 + \frac{1}{jkR} + \frac{1}{(jkR)^2} & 0 \\ 0 & 0 & \frac{-2}{jkR} + \frac{-2}{(jkR)^2} \end{pmatrix}$$

$$\begin{pmatrix} \cos\theta_R \cos\phi_R & \cos\theta_R \sin\phi_R & -\sin\theta_R \\ -\sin\phi_R & \cos\phi_R & 0 \\ \sin\theta_R \cos\phi_R & \sin\theta_R \sin\phi_R & \cos\theta_R \end{pmatrix} \begin{pmatrix} M_x(\rho', \phi', z') \\ M_y(\rho', \phi', z') \\ M_z(\rho', \phi', z') \end{pmatrix} \rho' d\rho' d\phi' dz'$$

$$\begin{pmatrix} E_x(x,y,z) \\ E_y(x,y,z) \\ E_z(x,y,z) \end{pmatrix} = +j k \int_0^\infty \int_0^{2\pi} \int_{-\infty}^\infty \frac{e^{-jkR}}{4\pi R}$$

$$\begin{pmatrix} \cos\theta_R \cos\phi_R & -\sin\phi_R & \sin\theta_R \cos\phi_R \\ \cos\theta_R \sin\phi_R & \cos\phi_R & \sin\theta_R \sin\phi_R \\ -\sin\theta_R & 0 & \cos\theta_R \end{pmatrix} \begin{pmatrix} 0 & -1 - \frac{1}{jkR} & 0 \\ 1 + \frac{1}{jkR} & 0 & 0 \\ 0 & 0 & 0 \end{pmatrix}$$

$$\begin{pmatrix} \cos\theta_R \cos\phi_R & \cos\theta_R \sin\phi_R & -\sin\theta_R \\ -\sin\phi_R & \cos\phi_R & 0 \\ \sin\theta_R \cos\phi_R & \sin\theta_R \sin\phi_R & \cos\theta_R \end{pmatrix} \begin{pmatrix} M_x(\rho', \phi', z) \\ M_y(\rho', \phi', z) \\ M_z(\rho', \phi', z) \end{pmatrix} \rho d\rho d\phi dz$$

where

$$R = [(x - \rho' \cos\phi')^2 + (y - \rho' \sin\phi')^2 + (z - z')^2]^{1/2}$$

$$\theta_R = \cos^{-1}[(z - z')/R]$$

$$\phi_R = \tan^{-1}[(y - \rho' \sin\phi') / (x - \rho' \cos\phi')] ]$$

For a circular aperture of radius  $a$  with  $x$ - polarized magnetic current distribution,

$$\begin{pmatrix} M_x(\rho', \phi', z) \\ M_y(\rho', \phi', z) \\ M_z(\rho', \phi', z) \end{pmatrix} = \begin{pmatrix} 1 \\ 0 \\ 0 \end{pmatrix} K(\rho', \phi') \delta(z), \quad 0 \leq \rho' \leq a, \quad 0 \leq \phi' \leq 2\pi, \quad z > 0$$

Then,

$$\begin{pmatrix} E_x(x,y,z) \\ E_y(x,y,z) \\ E_z(x,y,z) \end{pmatrix} = +jk \int_0^\infty \int_0^{2\pi} \int_{-\infty}^\infty \begin{pmatrix} 0 \\ (1 + \frac{1}{jkR}) \cos\theta_R \\ -(1 + \frac{1}{jkR}) \sin\theta_R \sin\phi_R \end{pmatrix} \frac{e^{-jkR}}{4\pi R} K(\rho', \phi') \delta(z) \rho d\rho d\phi dz$$

$$\begin{pmatrix} H_x(x, y, z) \\ H_y(x, y, z) \\ H_z(x, y, z) \end{pmatrix} = +j \frac{k}{\eta} \int_0^\infty \int_0^{2\pi} \int_{-\infty}^\infty \begin{pmatrix} -(1 + \frac{3}{jkR} + \frac{3}{(jkR)^2}) \sin^2 \theta_R \cos^2 \phi_R + (1 + \frac{1}{jkR} + \frac{1}{(jkR)^2}) \\ -(1 + \frac{3}{jkR} + \frac{3}{(jkR)^2}) \sin^2 \theta_R \sin \phi_R \cos \phi_R \\ -(1 + \frac{3}{jkR} + \frac{3}{(jkR)^2}) \sin \theta_R \cos \theta_R \cos \phi_R \end{pmatrix} \\ \cdot \frac{e^{-jkR}}{4\pi R} K(\rho', \phi') \delta(z') \rho' d\rho' d\phi' dz'$$

For the case of a uniform current distribution, we can evaluate the integrals in a closed form for observation points along the axis. To show this, let  $K(\rho', \phi') = 1$ , and  $(x, y, z) = (0, 0, z)$ . The integrals in  $z'$  and  $\phi'$  can readily be evaluated. The results are,

$$\begin{pmatrix} E_x(0, 0, z) \\ E_y(0, 0, z) \\ E_z(0, 0, z) \end{pmatrix} = \begin{pmatrix} 0 \\ 1 \\ 0 \end{pmatrix} \frac{1}{2} \int_{jkz}^{jk\zeta} (1 + \frac{1}{\sigma'}) \frac{jkz}{\sigma'} e^{-\sigma'} d\sigma'$$

$$\begin{pmatrix} H_x(0, 0, z) \\ H_y(0, 0, z) \\ H_z(0, 0, z) \end{pmatrix} = \begin{pmatrix} 1 \\ 0 \\ 0 \end{pmatrix} \frac{-1}{2\eta} \int_{jkz}^{jk\zeta} [(1 - \frac{1}{\sigma'} - \frac{1}{\sigma'^2}) - (1 + \frac{3}{\sigma'} + \frac{3}{\sigma'^2}) \frac{k^2 z^2}{\sigma'^2}] e^{-\sigma'} d\sigma'$$

where change of variable by  $\sigma' = jk(\rho'^2 + z'^2)^{1/2}$ , and  $\zeta = (z^2 + a^2)^{1/2}$

Performing the integration by parts yields,

$$\begin{pmatrix} E_x(0, 0, z) \\ E_y(0, 0, z) \\ E_z(0, 0, z) \end{pmatrix} = \begin{pmatrix} 0 \\ 1 \\ 0 \end{pmatrix} \left( \frac{1}{2} e^{-jkz} - \frac{1}{2} \frac{z}{\zeta} e^{-jk\zeta} \right)$$

$$\begin{pmatrix} H_x(0, 0, z) \\ H_y(0, 0, z) \\ H_z(0, 0, z) \end{pmatrix} = \begin{pmatrix} 1 \\ 0 \\ 0 \end{pmatrix} \left( \frac{-1}{2\eta} e^{-jkz} + \frac{1}{4\eta} [(1 - \frac{1}{jk\zeta}) + (1 + \frac{1}{jk\zeta}) \frac{z^2}{\zeta^2}] e^{-jk\zeta} \right)$$

These are the exact solutions in the closed form expressions the same as those given by eqs. (8) and (11) of [8].

## CONCLUSION

The useful formulas for solving Maxwell's equations with given current distribution are derived. The results are exact with no approximation, and can be explicitly written in matrix formulation, such that both the current source and resulting fields may be easily expressed in terms of various coordinate systems. If the radiation fields either in the near or far region are of primary interest, the formulation is greatly simplified. The electric and magnetic fields can be simply found by the direct matrix multiplication whenever the radiation vector due to the current source is determined. Some well-known antenna configurations are used to demonstrate the merit of the technique presented.

## APPENDIX

For reference, some useful formulas are listed below. These formulas are independent of coordinate system. Also  $\vec{J}$  is treated as a constant under the vector differential operator  $\nabla$ .

$$\nabla \cdot \vec{R} = 3 \quad (26a)$$

$$\nabla \times \vec{R} = 0 \quad (26b)$$

$$\nabla (\vec{R} \cdot \vec{J}) = \vec{J} \quad (26c)$$

$$\nabla \cdot (\vec{R} \times \vec{J}) = 0 \quad (26d)$$

$$\nabla \times (\vec{R} \times \vec{J}) = -2\vec{J} \quad (26e)$$

$$\vec{J} \cdot \nabla \vec{R} = \vec{J} \quad (26f)$$

$$\nabla \cdot \hat{R} = \frac{2}{R} \quad (27a)$$

$$\nabla \times \hat{R} = 0 \quad (27b)$$

$$\nabla (\hat{R} \cdot \vec{J}) = \frac{1}{R} (1 - \hat{R} \hat{R} \cdot) \vec{J} \quad (27c)$$

$$\nabla \cdot (\hat{R} \times \vec{J}) = 0 \quad (27d)$$

$$\nabla \times (\hat{R} \times \vec{J}) = -\frac{1}{R} (1 + \hat{R} \hat{R} \cdot) \vec{J} \quad (27e)$$

$$\vec{J} \cdot \nabla \hat{R} = \frac{1}{R} (1 - \hat{R} \hat{R} \cdot) \vec{J} \quad (27f)$$

$$\nabla \cdot f(R) \vec{J} = \hat{R} \cdot f'(R) \vec{J} \quad (28a)$$

$$\nabla \times f(R) \vec{J} = \hat{R} \times f'(R) \vec{J} \quad (28b)$$

$$\nabla f(R) = \hat{R} f'(R) \quad (28c)$$

$$\nabla \cdot \vec{F}(R) = \hat{R} \cdot \vec{F}'(R) \quad (29a)$$

$$\nabla \times \vec{F}(R) = \hat{R} \times \vec{F}'(R) \quad (29b)$$

$$\nabla (\vec{F}(R) \cdot \vec{J}) = \hat{R} \vec{F}'(R) \cdot \vec{J} \quad (29c)$$

where, for instance, both  $\vec{r}$  and  $\vec{r}'$  are in the Cartesian coordinate system,

$$\vec{R} = \vec{r} - \vec{r}' = \hat{x}(x - x') + \hat{y}(y - y') + \hat{z}(z - z') \quad (30a)$$

$$R = |\vec{r} - \vec{r}'| = [(x - x')^2 + (y - y')^2 + (z - z')^2]^{1/2} \quad (30b)$$

$$\hat{R} = \frac{\vec{R}}{R} = \frac{\vec{r} - \vec{r}'}{|\vec{r} - \vec{r}'|} = \hat{x} \frac{\partial R}{\partial x} + \hat{y} \frac{\partial R}{\partial y} + \hat{z} \frac{\partial R}{\partial z} \quad (30c)$$

The derivation of (7) from (6) may therefore be made by using some of the above formulas, such as (27) and (28).

$$\begin{aligned} g(R) \vec{J} + \frac{1}{k^2} \nabla \nabla \cdot g(R) \vec{J} &= g(R) \vec{J} + \frac{1}{k^2} \nabla (\hat{R} \cdot g'(R) \vec{J}) \\ &= g(R) \vec{J} + \frac{1}{k^2} g'(R) \nabla (\hat{R} \cdot \vec{J}) + \frac{1}{k^2} (\hat{R} \cdot \vec{J}) \nabla g'(R) \\ &= g(R) \vec{J} + \frac{1}{k^2} g'(R) \frac{1}{R} (1 - \hat{R} \hat{R} \cdot) \vec{J} + \frac{1}{k^2} (\hat{R} \cdot \vec{J}) \hat{R} g''(R) \end{aligned} \quad (31a)$$

$$\frac{1}{-jk} \nabla \times g(R) \vec{J} = \frac{1}{-jk} \hat{R} \times g'(R) \vec{J} \quad (31b)$$

Since

$$g(R) = \frac{e^{-jkR}}{4\pi R} \quad (32a)$$

$$g'(R) = -jk \left( 1 + \frac{1}{jkR} \right) g(R) \quad (32b)$$

$$g''(R) = -k^2 \left( 1 + \frac{2}{jkR} + \frac{2}{(jkR)^2} \right) g(R) \quad (32c)$$

Then

$$\begin{aligned} \left[ 1 + \frac{1}{k^2} \nabla \nabla \cdot \right] g(R) \vec{J}(\vec{r}') \\ = g(R) \left[ \left( 1 + \frac{1}{jkR} + \frac{1}{(jkR)^2} \right) (1 - \hat{R} \hat{R} \cdot) + \left( \frac{-2}{jkR} + \frac{-2}{(jkR)^2} \right) \hat{R} \hat{R} \cdot \right] \vec{J}(\vec{r}') \end{aligned} \quad (33a)$$

$$\begin{aligned} \left[ \frac{1}{-jk} \nabla \times \right] g(R) \vec{J}(\vec{r}') \\ = g(R) \left[ \left( 1 + \frac{1}{jkR} \right) \hat{R} \times \right] \vec{J}(\vec{r}') \end{aligned} \quad (33b)$$

That is,

$$\bar{\bar{G}}_{\nabla}(\vec{r}) \, g(R) \, \vec{J}(\vec{r}') = g(R) \, \bar{\bar{G}}(\vec{R}) \, \vec{J}(\vec{r}') \quad (34a)$$

$$\bar{\bar{K}}_{\nabla}(\vec{r}) \, g(R) \, \vec{J}(\vec{r}') = g(R) \, \bar{\bar{K}}(\vec{R}) \, \vec{J}(\vec{r}') \quad (34b)$$

This completes the derivation.



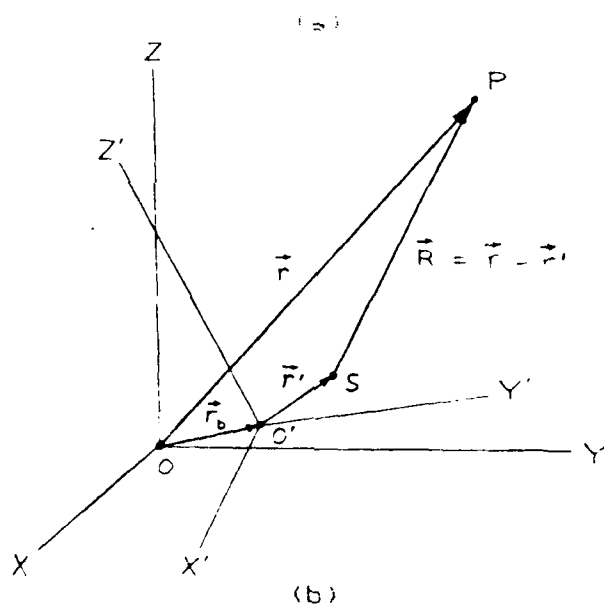
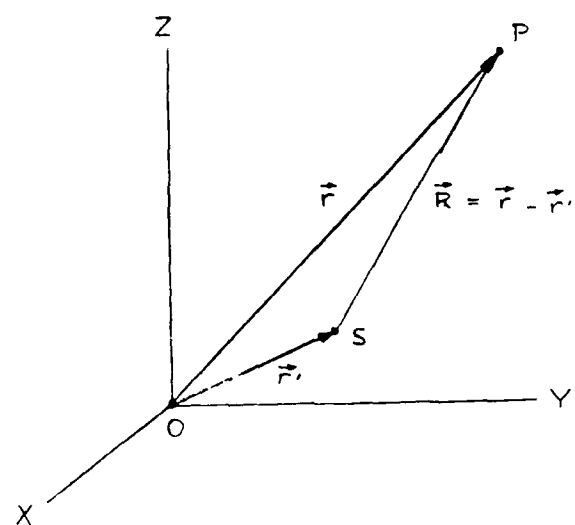


Figure 1. Vector positions of the source and the observation  
 (a) No origin translation and axis rotations,  
 (b) Origin translation by a vector  $\vec{r}_b$  and  
 axis rotations by Euler angles.

(0) VECTOR OPERATORS:

1. Vector  $\vec{A}$
2. Dot-Product  $\vec{A} \cdot$
3. Cross-Product  $\vec{A} \times$
4. Gradient  $\nabla$
5. Divergent  $\nabla \cdot$
6. Curl  $\nabla \times$
7. Divergent-Curl  $\nabla \cdot \nabla \times$
8. Curl-Gradient  $\nabla \times \nabla$
9. Divergent-Gradient  
(Scalar Laplacian)  $\nabla \cdot \nabla = \nabla^2$
10. Gradient-Divergent  $\nabla \nabla \cdot$
11. Curl-Curl  $\nabla \times \nabla \times$
12. Gradient-Divergent - Curl-Curl  
(Vector Laplacian)  $\nabla \nabla \cdot - \nabla \times \nabla \times = \nabla^2$

(A) CARTESIAN COORDINATES:  $c = (x, y, z)$

$$1. \quad (\vec{A})^c = \begin{pmatrix} A_x \\ A_y \\ A_z \end{pmatrix}$$

$$2. \quad \{\vec{A}\}^c = \begin{pmatrix} A_x & A_y & A_z \end{pmatrix}$$

$$3. \quad [\vec{A}]^c = \begin{pmatrix} 0 & -A_z & A_y \\ A_z & 0 & -A_x \\ -A_y & A_x & 0 \end{pmatrix}$$

$$4. \quad (\nabla)^c = \begin{pmatrix} \frac{\partial}{\partial x} \\ \frac{\partial}{\partial y} \\ \frac{\partial}{\partial z} \end{pmatrix}$$

$$5. \quad \{\nabla\}^c = \begin{pmatrix} \frac{\partial}{\partial x} & \frac{\partial}{\partial y} & \frac{\partial}{\partial z} \end{pmatrix}$$

$$6. \quad [\nabla]^c = \begin{pmatrix} 0 & -\frac{\partial}{\partial z} & \frac{\partial}{\partial y} \\ \frac{\partial}{\partial z} & 0 & -\frac{\partial}{\partial x} \\ -\frac{\partial}{\partial y} & \frac{\partial}{\partial x} & 0 \end{pmatrix}$$

$$7. \quad \{\nabla\}^c [\nabla]^c = \begin{pmatrix} 0 & 0 & 0 \end{pmatrix}$$

$$8. \quad [\nabla]^c (\nabla)^c = \begin{pmatrix} 0 \\ 0 \\ 0 \end{pmatrix}$$

$$9. \quad \{\nabla\}^c (\nabla)^c = \begin{pmatrix} \Delta^c \end{pmatrix}$$

$$\Delta^c = \frac{\partial^2}{\partial x^2} + \frac{\partial^2}{\partial y^2} + \frac{\partial^2}{\partial z^2}$$

$$10. \quad (\nabla)^c \{\nabla\}^c = \begin{pmatrix} \frac{\partial^2}{\partial x^2} & \frac{\partial^2}{\partial x \partial y} & \frac{\partial^2}{\partial z \partial x} \\ \frac{\partial^2}{\partial x \partial y} & \frac{\partial^2}{\partial y^2} & \frac{\partial^2}{\partial y \partial z} \\ \frac{\partial^2}{\partial z \partial x} & \frac{\partial^2}{\partial y \partial z} & \frac{\partial^2}{\partial z^2} \end{pmatrix}$$

$$11. \quad [\nabla]^c [\nabla]^c = \begin{pmatrix} -\frac{\partial^2}{\partial y^2} - \frac{\partial^2}{\partial z^2} & \frac{\partial^2}{\partial x \partial y} & \frac{\partial^2}{\partial z \partial x} \\ \frac{\partial^2}{\partial x \partial y} & -\frac{\partial^2}{\partial z^2} - \frac{\partial^2}{\partial x^2} & \frac{\partial^2}{\partial y \partial z} \\ \frac{\partial^2}{\partial z \partial x} & \frac{\partial^2}{\partial y \partial z} & -\frac{\partial^2}{\partial x^2} - \frac{\partial^2}{\partial y^2} \end{pmatrix}$$

$$12. \quad (\nabla)^c \{\nabla\}^c - [\nabla]^c [\nabla]^c = \begin{pmatrix} \Delta^c & 0 & 0 \\ 0 & \Delta^c & 0 \\ 0 & 0 & \Delta^c \end{pmatrix}$$

(B) CYLINDRICAL COORDINATES:  $d = (\rho, \phi, z)$

$$1. \quad (\vec{A})^d = \begin{pmatrix} A_\rho \\ A_\phi \\ A_z \end{pmatrix}$$

$$2. \quad \{\vec{A}\}^d = \begin{pmatrix} A_\rho & A_\phi & A_z \end{pmatrix}$$

$$3. \quad [\vec{A}]^d = \begin{pmatrix} 0 & -A_z & A_\phi \\ A_z & 0 & -A_\rho \\ -A_\phi & A_\rho & 0 \end{pmatrix}$$

$$4. \quad (\nabla)^d = \begin{pmatrix} \frac{\partial}{\partial \rho} \\ \frac{1}{\rho} \frac{\partial}{\partial \phi} \\ \frac{\partial}{\partial z} \end{pmatrix}$$

$$5. \quad \{\nabla\}^d = \begin{pmatrix} \frac{1}{\rho} \frac{\partial}{\partial \rho} \rho & \frac{1}{\rho} \frac{\partial}{\partial \phi} & \frac{\partial}{\partial z} \end{pmatrix}$$

$$6. \quad [\nabla]^d = \begin{pmatrix} 0 & -\frac{\partial}{\partial z} & \frac{1}{\rho} \frac{\partial}{\partial \phi} \\ \frac{\partial}{\partial z} & 0 & -\frac{\partial}{\partial \rho} \\ -\frac{1}{\rho} \frac{\partial}{\partial \phi} & \frac{1}{\rho} \frac{\partial}{\partial \rho} \rho & 0 \end{pmatrix}$$

$$7. \quad \{\nabla\}^d [\nabla]^d = \begin{pmatrix} 0 & 0 & 0 \end{pmatrix}$$

$$8. \quad [\nabla]^d \{\nabla\}^d = \begin{pmatrix} 0 \\ 0 \\ 0 \end{pmatrix}$$

$$9. \quad \{\nabla\}^d \{\nabla\}^d = \begin{pmatrix} \Delta^d \end{pmatrix}$$

$$\Delta^d = \frac{1}{\rho} \frac{\partial}{\partial \rho} \rho \frac{\partial}{\partial \rho} + \frac{1}{\rho^2} \frac{\partial^2}{\partial \phi^2} + \frac{\partial^2}{\partial z^2}$$

$$10. \quad (\nabla)^d \{\nabla\}^d = \begin{pmatrix} \frac{\partial^2}{\partial \rho^2} + \frac{1}{\rho} \frac{\partial}{\partial \rho} - \frac{1}{\rho^2} & \frac{1}{\rho} \left( \frac{\partial}{\partial \rho} - \frac{1}{\rho} \right) \frac{\partial}{\partial \phi} & \frac{\partial}{\partial \rho} \frac{\partial}{\partial z} \\ \frac{1}{\rho} \left( \frac{\partial}{\partial \rho} + \frac{1}{\rho} \right) \frac{\partial}{\partial \phi} & \frac{1}{\rho^2} \frac{\partial^2}{\partial \phi^2} & \frac{1}{\rho} \frac{\partial}{\partial \phi} \frac{\partial}{\partial z} \\ \left( \frac{\partial}{\partial \rho} + \frac{1}{\rho} \right) \frac{\partial}{\partial z} & \frac{1}{\rho} \frac{\partial}{\partial \phi} \frac{\partial}{\partial z} & \frac{\partial^2}{\partial z^2} \end{pmatrix}$$

$$11. \quad [\nabla]^d [\nabla]^d = \begin{pmatrix} -\frac{1}{\rho^2} \frac{\partial^2}{\partial \phi^2} - \frac{\partial^2}{\partial z^2} & \frac{1}{\rho} \left( \frac{\partial}{\partial \rho} + \frac{1}{\rho} \right) \frac{\partial}{\partial \phi} & \frac{\partial}{\partial \rho} \frac{\partial}{\partial z} \\ \frac{1}{\rho} \left( \frac{\partial}{\partial \rho} - \frac{1}{\rho} \right) \frac{\partial}{\partial \phi} & -\left( \frac{\partial^2}{\partial \rho^2} + \frac{1}{\rho} \frac{\partial}{\partial \rho} - \frac{1}{\rho^2} \right) - \frac{\partial^2}{\partial z^2} & \frac{1}{\rho} \frac{\partial}{\partial \phi} \frac{\partial}{\partial z} \\ \left( \frac{\partial}{\partial \rho} + \frac{1}{\rho} \right) \frac{\partial}{\partial z} & \frac{1}{\rho} \frac{\partial}{\partial \phi} \frac{\partial}{\partial z} & -\left( \frac{\partial^2}{\partial \rho^2} + \frac{1}{\rho} \frac{\partial}{\partial \rho} \right) - \frac{1}{\rho^2} \frac{\partial^2}{\partial \phi^2} \end{pmatrix}$$

$$12. \quad \{\nabla\}^d \{\nabla\}^d - [\nabla]^d [\nabla]^d = \begin{pmatrix} \Delta^d - \frac{1}{\rho^2} & -\frac{2}{\rho^2} \frac{\partial}{\partial \phi} & 0 \\ \frac{2}{\rho^2} \frac{\partial}{\partial \phi} & \Delta^d - \frac{1}{\rho^2} & 0 \\ 0 & 0 & \Delta^d \end{pmatrix}$$

(C) SPHERICAL COORDINATES:  $s = (\theta, \phi, r)$

$$1. \quad (\vec{A})^s = \begin{pmatrix} A_\theta \\ A_\phi \\ A_r \end{pmatrix}$$

$$2. \quad \{\vec{A}\}^s = \begin{pmatrix} A_\theta & A_\phi & A_r \end{pmatrix}$$

$$3. \quad [\vec{A}]^s = \begin{pmatrix} 0 & -A_r & A_\phi \\ A_r & 0 & -A_\theta \\ -A_\phi & A_\theta & 0 \end{pmatrix}$$

$$4. \quad (\nabla)^s = \begin{pmatrix} \frac{1}{r} \frac{\partial}{\partial \theta} \\ \frac{1}{r \sin \theta} \frac{\partial}{\partial \phi} \\ \frac{\partial}{\partial r} \end{pmatrix}$$

$$5. \quad \{\nabla\}^s = \begin{pmatrix} \frac{1}{r \sin \theta} \frac{\partial}{\partial \theta} \sin \theta & \frac{1}{r \sin \theta} \frac{\partial}{\partial \phi} & \frac{1}{r^2} \frac{\partial}{\partial r} r^2 \end{pmatrix}$$

$$6. \quad [\nabla]^s = \begin{pmatrix} 0 & -\frac{1}{r} \frac{\partial}{\partial r} r & \frac{1}{r \sin \theta} \frac{\partial}{\partial \phi} \\ \frac{1}{r} \frac{\partial}{\partial r} r & 0 & -\frac{1}{r} \frac{\partial}{\partial \theta} \\ -\frac{1}{r \sin \theta} \frac{\partial}{\partial \phi} & \frac{1}{r \sin \theta} \frac{\partial}{\partial \theta} \sin \theta & 0 \end{pmatrix}$$

$$7. \quad \{\nabla\}^s [\nabla]^s = \begin{pmatrix} 0 & 0 & 0 \end{pmatrix}$$

$$8. \quad [\nabla]^s (\nabla)^s = \begin{pmatrix} 0 \\ 0 \\ 0 \end{pmatrix}$$

$$9. \quad \{\nabla\}^s (\nabla)^s = \begin{pmatrix} \Delta^s \end{pmatrix}$$

$$\Delta^s = -\frac{1}{r^2} \frac{1}{\sin \theta} \frac{\partial}{\partial \theta} \sin \theta \frac{\partial}{\partial \theta} + \frac{1}{r^2} \frac{1}{\sin^2 \theta} \frac{\partial^2}{\partial \phi^2} + \frac{1}{r^2} \frac{\partial}{\partial r} r^2 \frac{\partial}{\partial r}$$

$$10. \quad (\nabla)^s \{\nabla\}^s = \begin{pmatrix} \frac{1}{r^2} \left( \frac{\partial^2}{\partial \theta^2} + \frac{\cos \theta}{\sin \theta} \frac{\partial}{\partial \theta} - \frac{1}{\sin^2 \theta} \right) & \frac{1}{r^2} \frac{1}{\sin \theta} \left( \frac{\partial}{\partial \theta} - \frac{\cos \theta}{\sin \theta} \right) \frac{\partial}{\partial \phi} & \frac{1}{r} \left( \frac{\partial}{\partial r} + \frac{2}{r} \right) \frac{\partial}{\partial \theta} \\ \frac{1}{r^2} \frac{1}{\sin \theta} \left( \frac{\partial}{\partial \theta} + \frac{\cos \theta}{\sin \theta} \right) \frac{\partial}{\partial \phi} & \frac{1}{r^2} \frac{1}{\sin^2 \theta} \frac{\partial^2}{\partial \phi^2} & \frac{1}{r} \left( \frac{\partial}{\partial r} + \frac{2}{r} \right) \frac{1}{\sin \theta} \frac{\partial}{\partial \phi} \\ \frac{1}{r} \left( \frac{\partial}{\partial r} - \frac{1}{r} \right) \left( \frac{\partial}{\partial \theta} + \frac{\cos \theta}{\sin \theta} \right) & \frac{1}{r} \left( \frac{\partial}{\partial r} - \frac{1}{r} \right) \frac{1}{\sin \theta} \frac{\partial}{\partial \phi} & \frac{\partial^2}{\partial r^2} + \frac{2}{r} \frac{\partial}{\partial r} - \frac{2}{r^2} \end{pmatrix}$$

$$11. \quad [\nabla]^s [\nabla]^s = \begin{pmatrix} -\left( \frac{\partial^2}{\partial r^2} + \frac{2}{r} \frac{\partial}{\partial r} \right) - \frac{1}{r^2} \frac{1}{\sin^2 \theta} \frac{\partial^2}{\partial \phi^2} & \frac{1}{r^2} \frac{1}{\sin \theta} \left( \frac{\partial}{\partial \theta} + \frac{\cos \theta}{\sin \theta} \right) \frac{\partial}{\partial \phi} & \frac{1}{r} \frac{\partial}{\partial r} \frac{\partial}{\partial \theta} \\ \frac{1}{r^2} \frac{1}{\sin \theta} \left( \frac{\partial}{\partial \theta} - \frac{\cos \theta}{\sin \theta} \right) \frac{\partial}{\partial \phi} & -\left( \frac{\partial^2}{\partial r^2} + \frac{2}{r} \frac{\partial}{\partial r} \right) - \frac{1}{r^2} \left( \frac{\partial^2}{\partial \theta^2} + \frac{\cos \theta}{\sin \theta} \frac{\partial}{\partial \theta} - \frac{1}{\sin^2 \theta} \right) & \frac{1}{r} \frac{\partial}{\partial r} \frac{1}{\sin \theta} \frac{\partial}{\partial \phi} \\ \frac{1}{r} \left( \frac{\partial}{\partial r} + \frac{1}{r} \right) \left( \frac{\partial}{\partial \theta} + \frac{\cos \theta}{\sin \theta} \right) & \frac{1}{r} \left( \frac{\partial}{\partial r} + \frac{1}{r} \right) \frac{1}{\sin \theta} \frac{\partial}{\partial \phi} & -\frac{1}{r^2} \left( \frac{\partial^2}{\partial \theta^2} + \frac{\cos \theta}{\sin \theta} \frac{\partial}{\partial \theta} \right) - \frac{1}{r^2} \frac{1}{\sin^2 \theta} \frac{\partial^2}{\partial \phi^2} \end{pmatrix}$$

$$12. \quad (\nabla)^s \{\nabla\}^s - [\nabla]^s [\nabla]^s = \begin{pmatrix} \Delta^s - \frac{1}{r^2} \frac{1}{\sin^2 \theta} & -\frac{2}{r^2} \frac{\cos \theta}{\sin^2 \theta} \frac{\partial}{\partial \phi} & \frac{2}{r^2} \frac{\partial}{\partial \theta} \\ \frac{2}{r^2} \frac{\cos \theta}{\sin^2 \theta} \frac{\partial}{\partial \phi} & \Delta^s - \frac{1}{r^2} \frac{1}{\sin^2 \theta} & \frac{2}{r^2} \frac{1}{\sin \theta} \frac{\partial}{\partial \phi} \\ -\frac{2}{r^2} \left( \frac{\partial}{\partial \theta} + \frac{\cos \theta}{\sin \theta} \right) & -\frac{2}{r^2} \frac{1}{\sin \theta} \frac{\partial}{\partial \phi} & \Delta^s - \frac{2}{r^2} \end{pmatrix}$$

## REFERENCES:

1. Silver, S. (1949) Microwave Antenna Theory and Design, New York: McGraw-Hill, Ch 3.
2. Harrington, R. F. (1961) Time Harmonic Electromagnetic Fields. New York: McGraw-Hill, Ch 2-3.
3. Elliott, R. S. (1981) Antenna Theory and Design. New York: Prentice-Hall, Ch 1-2.
4. Ramo, S.; Whinnery, J. R.; and Van Duzer, T (1984) Fields and Waves in Communication Electronics. New York: John Wiley and Sons, Ch. 12.
5. Rudge, A. W.; Milne, K.; Oliver, A. D. and Knight, P. ed. (1982) The Handbook of Antenna Design, Vol. 1, London: Peter Peregrinus, Ch. 1.
6. Chang, F. C. (1986) Matrix formulation of vector operations in electromagnetics analysis, Antenna Application Symposium.
7. Chang, F. C. (1984) Novel coordinates transformation for antenna applications, IEEE Trans. Antennas Propagat., (Vol. AP-32), 1292-1297.
8. V.Galindo-Israel and Y. Rahmat-Samii, "A new look at Fresnel field computation using the Jacobi-Bessel series," IEEE Trans. Antennas Propagat., vol. AP-29, pp. 885-898, Nov. 1981.



## MISSION of *Rome Air Development Center*

*RADC plans and executes research, development, test and selected acquisition programs in support of Command, Control Communications and Intelligence (C<sup>3</sup>I) activities. Technical and engineering support within areas of technical competence is provided to ESD Program Offices (POs) and other ESD elements. The principal technical mission areas are communications, electromagnetic guidance and control, surveillance of ground and aerospace objects, intelligence data collection and handling, information system technology, solid state sciences, electromagnetics and electronic reliability, maintainability and compatibility.*